University of Tennessee, Knoxville

TRACE: Tennessee Research and Creative Exchange

Doctoral Dissertations

Graduate School

5-2021

Ion Irradiation Effects on Damage Annealing and Dopant Activation in Single Crystal SiC

Lauren Nuckols
lnuckols@vols.utk.edu

Follow this and additional works at: https://trace.tennessee.edu/utk_graddiss

Recommended Citation

Nuckols, Lauren, "Ion Irradiation Effects on Damage Annealing and Dopant Activation in Single Crystal SiC. " PhD diss., University of Tennessee, 2021.
https://trace.tennessee.edu/utk_graddiss/6647

This Dissertation is brought to you for free and open access by the Graduate School at TRACE: Tennessee Research and Creative Exchange. It has been accepted for inclusion in Doctoral Dissertations by an authorized administrator of TRACE: Tennessee Research and Creative Exchange. For more information, please contact trace@utk.edu.

To the Graduate Council:

I am submitting herewith a dissertation written by Lauren Nuckols entitled "Ion Irradiation Effects on Damage Annealing and Dopant Activation in Single Crystal SiC." I have examined the final electronic copy of this dissertation for form and content and recommend that it be accepted in partial fulfillment of the requirements for the degree of Doctor of Philosophy, with a major in Materials Science and Engineering.

William J. Weber, Major Professor

We have read this dissertation and recommend its acceptance:

Accepted for the Council:

Dixie L. Thompson

Vice Provost and Dean of the Graduate School

(Original signatures are on file with official student records.)

Ion Irradiation Effects on Damage Annealing and Dopant Activation in Single Crystal SiC

A Dissertation Presented for the
Doctor of Philosophy
Degree
The University of Tennessee, Knoxville

Lauren Nuckols
May 2021

Copyright © 2021 by Lauren Nuckols
All rights reserved.

Dedicated to my husband, Michael and my father, David.

ACKNOWLEDGEMENTS

I would like to express my gratitude to my chair and advisor, Prof. William J. Weber for his support, guidance, and patience throughout my graduate school career. I would also like to thank the rest of my thesis committee members, Prof. Yanwen Zhang, Prof. Miguel Crespillo, and Prof. Maik Lang, for their encouragement and thoughtful advice.

My thanks to Chen Xu, a former lab member, for being the best ion irradiation partner.

Also, my gratitude goes out to Prof. Eric Lukosi and Jessica Charest for their help with sheet resistivity testing.

Finally, I'd like to thank my family and friends for their constant emotional support and love. I am forever grateful to my husband, Michael, who now knows more about ionization induced annealing in silicon carbide than any software developer should.

ABSTRACT

Energetic ions deposit their energy into a target material through elastic and inelastic processes: termed nuclear and electronic energy loss. In SiC [silicon carbide], these two processes are coupled and often competing, where nuclear energy loss generates defects and disorder, and electronic energy loss anneals the material. This work examines the relationship between these energy deposition processes and their impact on single crystal, 3C- and 4H-SiC microstructure via intermediate energy ion irradiations. With increasing incident ion atomic mass, decoupling between the two processes takes place, and inelastic energy deposition becomes less effective at inducing in-cascade annealing. Further, there are thresholds in electronic energy loss above which, disorder induced by damage energy is totally suppressed. These thresholds increase sub-linearly with incident ion atomic number. The feasibility of inelastic energy deposition inducing dopant activation is also studied. While 21 MeV Ni irradiation failed to activate implanted As ions, the irradiation did reduce implantation damage and altered the disorder and defect distribution in SiC. Overall, electronic energy loss from intermediate to higher energy ions can significantly alter physical disordering processes and electrical properties in SiC.

TABLE OF CONTENTS

Chapter One Introduction and General Information 1
1.1 Brief History of Nuclear Energy Use in the United States 1
1.2 Generation IV+ Fission Reactors: Overview 2
1.3 Fusion Reactors: Overview 5
1.4 Silicon Carbide: Overview 8
1.5 Transmutation reaction and dopant effects in SiC 12
Chapter Two Literature Review 17
2.1 Ions used as a surrogate for neutron irradiations 17
2.2 Ion Energy Deposition 19
2.2.1 Nuclear Energy Loss 19
2.2.1 Electronic Energy Loss 22
2.2.3 Nomenclature 23
Chapter Three Review of previous irradiation effects in SiC studies 26
3.1 S_e Annealing During SiC Irradiation 26
3.2 Temperature Effects 31
Chapter Four Methodology 36
4.1 Single Crystal SiC 36
4.2 Ion Irradiations 37
4.2.1 Stopping and Range of Ions in Matter (SRIM) Simulations 37
4.2.2 Ion Beam Materials Lab 37
4.3 Ion Beam Analysis 40
4.3.1 Rutherford backscattering spectrometry (RBS) 40
4.3.2 Channeling RBS (RBS/C) 43
4.4 Sheet Resistivity 45
Chapter Five Effects of recoil spectra and coupled inelastic and elastic energy dissipation on defect survival in 3C-SiC 48
5.1 Experimental Methods 48
5.2 SRIM and IM3D Simulations 49

5.3 Recoil Spectra 49
5.4 Disorder Comparison: 5 MeV Si and 10 MeV Au Ion Irradiations........................ 56
Chapter Six Coupled effects of electronic and nuclear energy deposition on damage accumulation in ion irradiated SiC 61
6.1 Experimental Methods 61
6.2 Lower Energy Si Irradiation Disordering 67
6.3 Higher Energy Si, Ti, and Ni Disordering 69
6.4 Electronic energy loss and disordering processes.. 72
6.5 S_e Thresholds 74
Chapter Seven Ion induced ionization effects on dopant activation in 4H-SiC 76
7.1 Methods.. 76
7.2 Arsenic Distribution and Activation 79
7.3 Disorder on the Si-Lattice.. 83
7.4 Sheet Resistivity.. 86
Chapter Eight Conclusions 90
List of References 93
Vita.. 106

LIST OF TABLES

Table 1-1 Concentration in appm of solid transmutation products produced in SiC for fluences of 10^{23} n/cm^2 from magnetic and inertial fusion energy reactors (MFE and IFE) and the High Flux Isotope Fission Reactors (HFIR), along with the minimum threshold neutron energy for formation. Data from ref. [31]. 15

Table 3-1 Summary of experiments using SHIs to anneal pre-existing damage in SiC. The S_e values for the SHI range from 20-33 keV/nm. 28

Table 5-1 SRIM (5 MeV Si) and IM3D (10 MeV Au) predicted total ionization energy, damage energy, and total ionization energy to damage energy depositions ratios at different depths. 53

Table 6-1 SRIM predicted surface values of S_e, S_n, and ion range values for various ions in 4H-SiC. 62

Table 6-2 Tested ion species, fluences, and fluxes. 66

Table 6-3 $S_{e,th}$, E_{th}, and dose (dpa) for a fluence of 1×10^{15} cm^{-2} at total damage suppression threshold values for all irradiations. (*) represents data obtained by ref [34]. 75

Table 7-1 Implantation and irradiation conditions for different area on 4H-SiC samples. 78

LIST OF FIGURES

Figure 1-1 Timeline of nuclear power plant designs, starting with Gen I prototype reactors to Gen IV future reactors [6]. 3

Figure 1-2 MSR schematic including freeze plug and emergency dump tanks, as published in ref. [14]. 6

Figure 1-3 Schematic of VHTR as published in ref. [14]. 6

Figure 1-4 Schematic of tokamak reactor [18]. 9

Figure 1-5 NIF schematic of inertially confined fusion process. 192 laser beams are directed to a dime size, gold cylinder heating the fuel pellet [20]. 9

Figure 1-6 Dose and temperature requirements for structural materials for fission and fusion reactors [9]. 11

Figure 1-7 Estimated operating temperatures for nuclear structural material with 10 to 50 dpa damage levels [9]. 11

Figure 1-8 Unit cells of 3C-, 4H-, and 6H-SiC [32]. 13

Figure 1-9 Gaseous transmutation production (appm/full power year) and damage rates verses depth from plasma for (a) magnetic fusion energy reactor and (b) inertial fusion energy reactor [35]. 15

Figure 2-1 SRIM predicted electronic and nuclear energy loss per unit depth for 2 MeV Au and 21 MeV Si ion in SiC. 20

Figure 2-2 Energy loss mechanisms as a function of gold ion energy and energy per gold atomic mass in SiC 20

Figure 2-3 SRIM predicted energy partitioning processes of 21 MeV Ni traversing through SiC. Differences between inelastic and elastic processes are largest for the EOR of the ions, where much of the energy transferred to PKAs is deposited inelastically. 25

Figure 3-1 Si lattice damage profiles for SiC pre-damaged from 700 keV I ions then annealed with 827 MeV Pb ions (S_e ~33 keV/nm). Fluence units are in ions/cm^2 [71]. 27

Figure 3-2 Plots indicating little detectable damage from irradiations (a) XRD results of nanostructured SiC irradiated with 95 MeV Xe ions, (b) RBS/C results of SC 6H-SiC irradiated with 910 MeV Xe ions [76]. 30

Figure 3-3 Annealing comparison for two initial relative disorder fractions: (a) 0.36 and (b) 0.72 [78]. 30

Figure 3-4 Linear dependence of critical amorphization dose (determined at disorder level of 0.97) on the ratio of ionization to dpa rate [63]. 32

Figure 3-5 Annealing stages for SiC irradiated at 170 K with 2 MeV Au ions [81]. 34

Figure 3-6 Disordering as a function of irradiation temperature [83]. 34

Figure 3-7 Critical temperature of amorphization dependence on incident ion E/M ratios [83-87]. 35

Figure 4-1 IBML (a) schematics and (b) photo from beamline 6 side of laboratory. 38

Figure 4-2 Schematic of ion irradiation area projection due to tilting of the target material. The area size due to projection in one direction is the beam size divided by the cosign of the angle of tilt. 41

Figure 4-3 K-factor as a function of target mass at θ = 155°. The slope of the spectra is a measure of mass resolution. Note the greater slope for the lower mass targets, indicating improved mass resolution. 41

Figure 4-4 Schematic of RBS basic process. 42

Figure 4-5 RBS spectra for pristine 4H-SiC in random and channeling orientations. Yield from the SiC in channeling orientation is greatly diminished. 44

Figure 4-6 Schematic of defect effects on incident RBS beam in a channeling orientated crystal: (a) dechanneling due to a substitutional defect, (b) channeling in a pristine channel, and (c) backscattering due to a displacement or interstitial defect. 46

Figure 4-7 Four-point probe sheet resistivity measurement set-up from the MPRF. Four collinear, equally spaced probes are placed on the surface of the sample. Current is applied through contacts 1 and 4, while the voltage is measured with a voltmeter between contacts 2 and 3. 46

Figure 5-1 (a) SRIM and IM3D predicted depth profiles of local displacement production per ion for 5 MeV Si ions in SiC, and (b) experimentally derived relative disorder derived and reported Xue et al. [63] 50
Figure 5-2 (a) comparison of SRIM and IM3D predicted local displacement production per ion for 10 MeV Au ions in SiC. Differences stem from IM3D simulation employing a new experimentally derived electronic stopping power, and (b) experimentally derived Si disorder. 50
Figure 5-3 The partitioning of incident ion energy per unit depth to total ionization energy and to the damage energy for (a) 5 MeV Si ions and (b) 10 MeV Au ions. 51
Figure 5-4 Radial distribution of displacement collisions by full-cascade SRIM simulations along a section of pathlength from 700 to 800 nm predicted for (a) 5 MeV Si ions and (b) 10 MeV Au ions. Electronic and damage energy depositions to the atomic lattice over a pathlength of 700 to 800 nm by (c) 5 MeV Si ions and (d) 10 MeV Au ions. 54
Figure 5-5 Weighted primary recoil spectra for 5 MeV Si ions, 10 MeV Au ions in SiC compared with HFIR neutrons and fusion neutrons calculated by Guo et al. [98]... 55
Figure 5-6 Relative disorder on Si sublattice at the damage peak as a function of damage dose in 3C-SiC irradiated with 5 MeV Si ions and 10 MeV Au ions. 57
Figure 5-7 Relative disorder fraction on the Si sublattice in 3C-SiC as a function of damage dose (dpa) at different depths: (a) 5 MeV Si ions in SiC (adapted from Ref[63]), and (b) 10 MeV Au ions. 57
Figure 5-8 Linear dependence of inverse dose to achieve a specific level of disorder on the ratio of ionization energy to damage energy in SiC at 300 K; (a) disorder level of 0.15 and 0.2 under 5 MeV Si irradiation and (b) disorder levels of 0.2 and 0.4 under 10 MeV Au irradiation. 59
Figure 6-1 SRIM predicted electronic (S_e) and nuclear (S_n) energy loss along with predicted damage doses (dpa) for a fluence of 1×10^{15} cm^{-2} for (a) 10 MeV Si, (b) 21 MeV Si, (c) 23 MeV Ti, and (d) 21 MeV Ni irradiations. Shaded region represents RBS/C characterization region. 64

Figure 6-2 Disorder on Si-sublattices as a function of depths for (a) 10 MeV Si, (b) 15 MeV Si, and (c) 18 MeV Si irradiations. 68

Figure 6-3 Si-lattice disorder as a function of either fluence (a) or dose (b). (a) 15 MeV Si irradiation shows constant disorder with fluences ranging from 5 to 20 × 10^{15} cm^{-2}. (b) Comparison of disorder accumulation for 5, 10, and 15 MeV Si irradiations. ... 68

Figure 6-4 Si-sublattice disorder as a function of depth for (a) 21 MeV Si, (b) 20 MeV Ti, (c) 23 MeV Ti, and (d) 21 MeV Ni irradiations. 70

Figure 6-5 Radial distribution of displacements and radial temperature profiles from inelastic thermal spike model for (a) 18 MeV Si and (b) 20 MeV Ti...................... 71

Figure 6-6 (a) Si disorder as a function of S_e (data from 1×10^{15} cm^{-2} fluence irradiations). (b) Rate of disorder as a function of incident ion Z values (slopes from (a))........... 73

Figure 6-7 Electronic energy loss thresholds above which full damage suppression occurs. 75

Figure 7-1 SRIM predicted energy partitioning from 21 MeV Ni ions in SiC. Shaded region represents RBS/C characterization probing depth. 80

Figure 7-2 Normalized RBS/C spectra of 4H-SiC implanted with 1 MeV As ions at 60° incident angle then irradiated with 21 MeV Ni ions. (Left) Implantations were performed at 250°C and (right) 500°C. All Ni irradiations were performed at room temperature. 80

Figure 7-3 RBS/C results of arsenic peak yield and distributions comparison of channeling and random orientations after irradiations at fluences ranging from 5 × 10^{14} to 1.5 × 10^{15} cm^{-2} for (a) 250°C implantation and (b) 500°C implantations......................... 81

Figure 7-4 (a) RBS/C spectra and (b) disorder measured on the Si lattice comparing 250°C and 500°C doping temperatures.. 84

Figure 7-5 Disorder on the Si-lattice (smoothed with the Savitzky-Galay method) from implantations and implantations + Ni irradiations for (a) 250°C implantation temperatures and (b) 500°C implantation temperatures. 84

Figure 7-6 Depth profiles of the As yield implanted in SiC overlaid with disorder on the Si-lattice resulting from the As implantation at (a) 250°C and (b) 500°C. 87

Figure 7-7 Sheet resistivity values as a function of Ni irradiation fluences for 250 and 500°C implantation temperatures. 87
Figure 8-1 Graphical summary of the experiments and conclusions of this work. 92

CHAPTER ONE
INTRODUCTION AND GENERAL INFORMATION

1.1 Brief History of Nuclear Energy Use in the United States

The United States Atomic Energy Commission (AEC) was formed in 1946, shortly after the end of the second world war and the atomic bombings of Hiroshima and Nagasaki. The purpose of the AEC was to encourage and control research on peacetime applications of atomic technology and sciences [1]. However, only two years later in 1948, partly as a response to the ramping-up Cold War, President Truman and congress made it clear to AEC directors that the true priority of the commission was to develop and build up an arsenal of new atomic weapons, including hydrogen bombs [2]. In the AEC's 1949 spending, over 65% of the budget (> $423 million) was designated for developing and producing plutonium and weapons, while only 0.3% of the budget ($1.8 million) was designated to a power reactor development program [3]. It was not until 1954, two years after developing and testing the first hydrogen bombs, that construction on the first commercial nuclear power reactor, the Shippingport plant, began [2,4].

The Shippingport plant was developed largely for political purposes, so that the US would not lose face as the world's scientific powerhouse and would be the first nation to develop a commercial nuclear power plant, as, at the time, Russia, Canada, and Britain were all interested in atomic energy and close to building commercial plants. Because of this, Shippingport was designed to maximize build speed. The pressurized light-water reactor used was originally developed for a nuclear-powered aircraft carrier and required 93% enriched uranium and was capable of 60 MWe power output. At the time, the power output and efficiency from the Shippingport plant was impractical and disappointing compared to coal plants. However, the appeal of efficient nuclear power was still a powerful motivator, so the U.S. government began to invest more into atomic energy and offered subsidies for utility companies to develop next generation nuclear power plants. The next commercial nuclear plants built were boiling water reactors (BWR), where the reactor core boils demineralized water, driving a steam turbine to generate electricity.

Many of these were developed by General Electric as way to make nuclear power plants as cost effective as possible by limiting and standardizing design complexity [1,2,4].

Since the first commercial nuclear power plants, interest and investments in nuclear power has generally increased, and there has been several nuclear power reactor designs and concepts over time. Reactor designs are sorted by generation, ranging from Gen 1 early prototype reactors, like in the Shippingport facility, to Gen IV conceptual reactor designs anticipated for future power needs [5], shown in Figure 1-1[6]. Presently, with greater instances of climate change induced natural disasters caused by increasing atmospheric greenhouse gases largely from fossil-fuel use, there is renewed interest in more efficient and safe nuclear power plants that utilize fusion and Gen IV fission reactors [7,8]. However, the greater capabilities and safety from next generation power plants require improved technologies.

The development of fusion and Gen IV fission reactors are, in-part, material limited, as the structural materials required to build the reactors must be extremely high-performance in terms of radiation tolerance, thermal properties, and mechanical properties for a sustained time [9,10]. Energic neutrons produced from fission and fusion reactions cause atom displacements from lattice sites, generating point defects and displacement cascades. Accumulated radiation damage leads to radiation embrittlement, creep, volumetric swelling, and other changes in mechanical properties that shorten the functional lifetime of the irradiated material. Fully understanding and modeling how materials perform long-term in extreme radiation environments at elevated temperatures and doses is necessary for future nuclear power [9].

1.2 Generation IV+ Fission Reactors: Overview

In the year 2000, 10 countries formed the Generation IV International Forum (GIF) for the purpose of selecting the best and most practical new commercial nuclear reactors that could be in use before 2030. GIF evaluated over 100 potential designs before settling on six general reactor concepts as having the highest potential in achieving the safe, clean, and proliferation-resistant objectives set by the forum. The six reactor concepts considered for

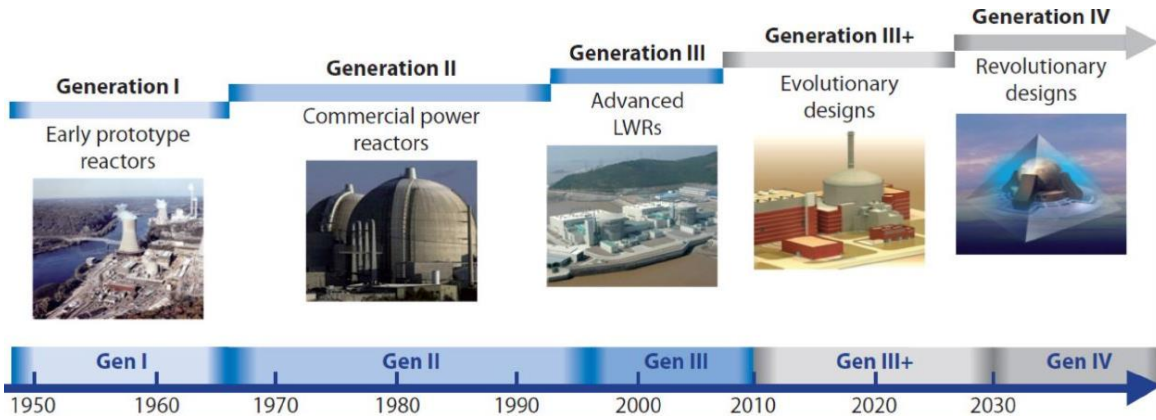

Figure 1-1 Timeline of nuclear power plant designs, starting with Gen I prototype reactors to Gen IV future reactors [6].

Gen-IV are: sodium cooled fast reactors (SFR), gas cooled fast reactors (GFR), lead cooled fast reactors (LFR), supercritical-water-cooled-reactors (SCWR), super high temperature reactors (VHTR), and molten-salt-fueled reactors (MSR) [11].

Reactors are considered 'fast' if fission chain reactions are sustained by energetic (> 0.5 MeV) neutrons [12]. These reactors are designed to be more efficient than current light water reactors as both primary isotopes of Uranium (U-238 and U-235) and Plutonium (Pu-239) may be used as a fissile source, potentially limiting nuclear proliferation and allowing for nuclear waste from water-cooled reactors to be used a fuel. Gen-IV fast reactor designs are sorted by coolant, all these coolants must be weak neutron moderators limit neutron energy loss and to allow for fast neutron fission reactions. Liquid metal cooled designs, such as SFR, LFR, and MSR are appealing due to their high thermal conductivity, improved inherent safety, as the reactors do not have to be pressurized, and greater efficiency, as reactors may be operated at higher temperatures compared to LWRs due the high vaporization temperatures of liquid metal coolants. SFRs are the most developed of the all the Gen-IV reactor designs and have already been built and operated in Russia, Japan, and France. Issues with sodium-cooled reactors are largely associated with the reactiveness of sodium to air and water, making coolant leaks significantly more dangerous than water leaks in LWRs. Issues with LFRs are associated with the high density and melting temperature of the lead coolant, making systems heavy and difficult to engineer as to mitigate risks of lead solidifying, which can damage pumps and other equipment. MSRs are also cooled via liquid metal, primarily molten fluoride salt. However, MSRs are characterized based on fuel source used; fissile materials dissolved directly into the coolant and which can be designed to use thermal or fast neutrons. The appeal of liquid fuel is that fission products may be removed and replaced with fissile materials in situ, allowing for over 50% greater fuel burn up to be achieved. Additionally, passive safety features can be added easily to MSRs, most notably frozen salt plugs, or freeze plugs, keeping fuel and coolant in the reactor vessel. These plugs must be constantly and actively cooled to be kept solid, so that in the event of a power outage or overheating due to run-away reactions, power cooling the plugs is shut off, melting them, and allowing the molten salt to flow to

spaced-out emergency dump tanks immediately stopping any nuclear activity [11,13,14] Figure 1-2 shows the schematic of a basic MSR design [14].

GFR is a general term for a fast reactor that uses gas, such as CO_2 and He, as a coolant. There is no risk of sudden coolant phase change induced explosions in GFRs. Additionally, VHTRs, Figure 1-3, designs are typically conceptualized also using a gas coolant. VHTR reactions use thermal neutrons where graphite, configured in either prismatic blocks or as pebbles, in the core act as a neutron moderator. As the name implies, these reactors are designed to operate at temperatures near 1000°C, meaning that enthalpy from heated coolant can be used to generate hydrogen via thermo-chemical processes. The high operating temperature, however, also puts significant thermal stress on reactor structural materials [11,14,15].

SCWRs are a more thermally efficient version current water reactors. These reactors are designed to operate at very high pressures (> 22.1 MPa) so that coolant water can be heated past its boiling point without boiling. SCWR core designs utilize either thermal or fast neutrons and are more efficient, approaching 44% efficiency, than boiling and light water reactors (up to 36% efficiency) because of their higher operating temperatures and simpler design; only one coolant pump is required to feed cooled coolant back to the reactor. However, the more compact design of SCWR also means smaller coolant buffers, so operating temperatures may become too high for reactor structural materials to withstand, leading to meltdown. Further, the higher operating temperature and pressure of SCWR leads to greater engineering challenges for vessel materials [11,14,16].

1.3 Fusion Reactors: Overview

In contrast with fission, where a large amount of energy (~ 200 MeV) is released when a neutron splits the nucleus of an unstable fissionable isotope into smaller atoms and additional neutrons, energy from fusion (~17.6 MeV) occurs when two light atomic nuclei react to form a larger nucleus. The only known self-sustaining, natural fusion occurs in the heart of stars. However, on earth even replicating the conditions on the sun at a smaller scale would not yield sufficient energy for practical fusion power output; this requires

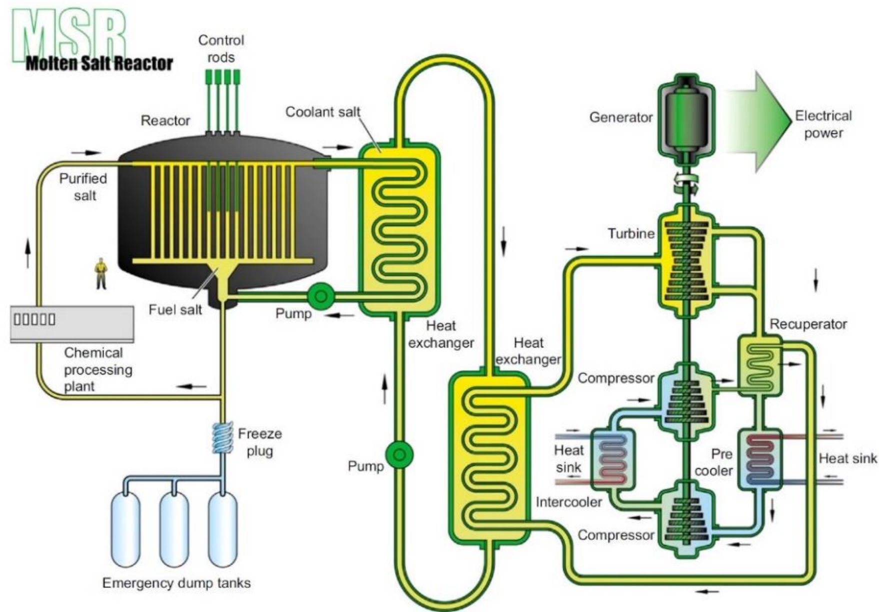

Figure 1-2 MSR schematic including freeze plug and emergency dump tanks, as published in ref. [14].

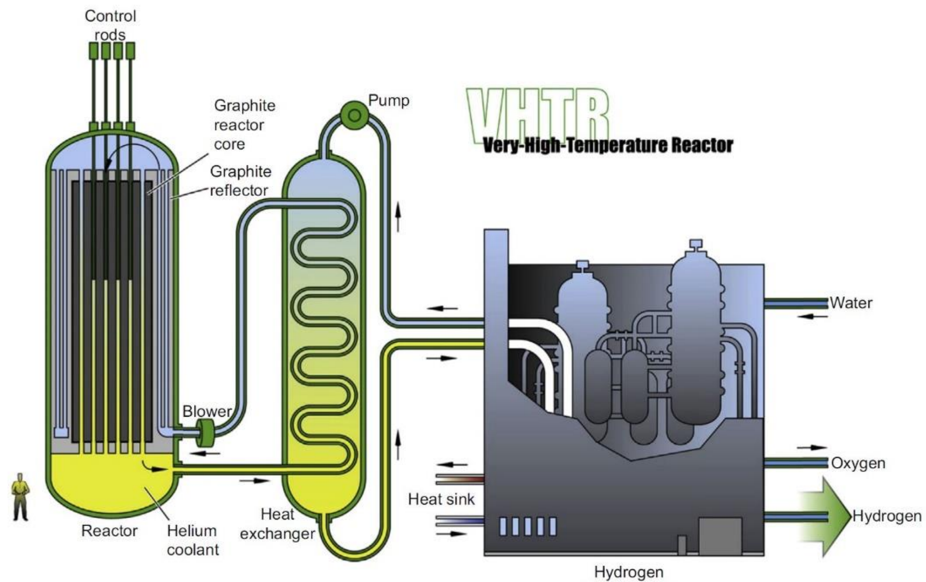

Figure 1-3 Schematic of VHTR as published in ref. [14].

much greater temperatures. In order to fuse, atoms must overcome Coulombic repulsion to allow for nuclear strong forces to take over to join the atoms. In fusion reactors, this is done by both exciting via heat, so that atoms travel faster, and by maximizing the density of fusion fuel. The temperatures required to induce fusion at a rate fast enough to generate a practical energy yield is approximately 150 million K, around 10 times greater than the interior of the sun. While achievable, there are no materials capable to withstand these conditions, but because the high temperatures strip electrons off atoms producing a charged plasma consisting of free electrons and positively charged ions, methods besides physical barriers may be used for containment.

Because of the extreme conditions required for these reactions, just experimenting with fusion requires massive, expensive, and technologically advanced facilities. Presently, there are no operational, power-producing fusion reactors. However, motivation to develop fusion power is huge because:

(1) Fusion fuel sources (most likely deuterium and tritium) are practically unlimited and do not require mining as they can be harvested from sea water or be bred from either fission or fusion reactors.

(2) Fusion reactors do not produce greenhouse gases.

(3) No long-lived radioactive nuclear waste is produced from fusion reactors, and the waste that is produced is minimal compared to fission reactors.

(4) There is greater inherent safety in running fusion reactors compared to fission reactors. If fusion plasma containment is compromised, the plasma will diffuse, cooling the plasma and halting fusion.

There are two established fusion plasma confinement methods currently functioning in fusion test reactors: magnetic and inertial confinement. Magnetic confinement employs a magnetic field to confine the fusion plasma away from container walls. Earliest attempts at fusion starting in the late fifties all utilized magnetic confinement. These reactor designs were characterized based on the path of the plasma from the magnetic field: either circular or helical. The most developed and well know fusion reactor design is the tokamak, where plasma is torus shaped via magnetic

confinement [17], as shown in Figure 1-4 [18]. The largest fusion reactor design currently being built, The International Thermonuclear Experimental Reactor (ITER), expected to be finished by 2025, is a Tokamak design [19].

Inertial confinement fusion (ICF) reactors, shown in Figure 1-5 [20], were first conceptualized in the 1970's and built in the 1980's. These reactors use high energy and flux lasers to compress and heat a small, ~10 mg, deuterium-tritium fuel pellet to induce an explosion on the outer layer of the pellet, forcing the interior of the pellet inward compressing and heating to induce fusion. The largest fusion cross-section reaction occurs through Equation 1-1. This reaction requires temperatures greater than 10 million °C to overcome columbic repulsion between fusing nuclei.

$$D + T \rightarrow n(14.1\ MeV) + \ {}^{4}He(3.5\ MeV) \qquad \text{Eq (1-1)}$$

ICF studies are largely limited to the National Ignition Facility (NIF) at Lawrence Livermore National Laboratory. The goal of the ICF reactor is to achieve ignition, where energy from formed alpha particles is deposited back to the plasma, increasing the temperature and reaction rate, resulting with an energy output much greater than the energy input and loss due to cooling through x-ray radiation and electron conduction [21].

1.4 Silicon Carbide: Overview

Structural materials for future fusion and fission reactors must be mechanically, thermally, and chemically resistant to the extreme radiation environments over a prolonged time. The international standard for quantifying and predicting damage induced by varying sized ions, electrons, and neutrons is the Norgett, Robinson, and Torrens (NRT), displacements per atom (dpa) formulation. The NRT model is an adaption of the Kinchin-Pease (KP) model, where damage is calculated as the deposited energy (T_d) divided by two times the displacement energy (E_d, i.e., the minimum incident energy required for an atom in a material to be displaced a sufficient distance to form a stable defect). The NRT model accounts for the fact that around 20% of the displaced atom sites tends to be refilled by another atom, because of this, the NRT model adds a 0.8 prefactor to the KP equations. The number of atomic displacements (N_d) as a function of deposited energy (T_d) predicted

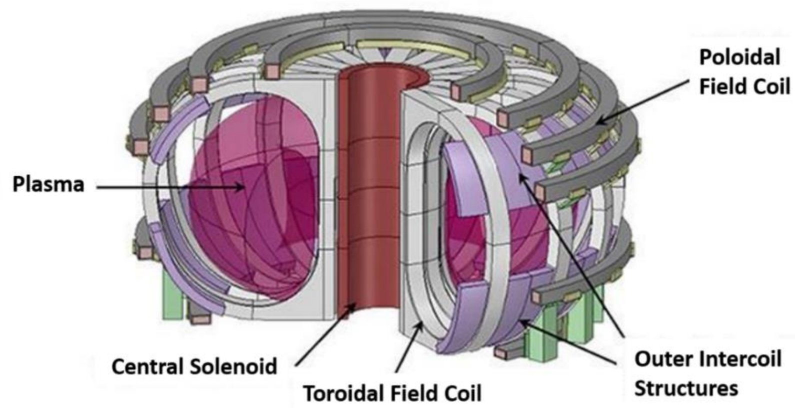

Figure 1-4 Schematic of tokamak reactor [18].

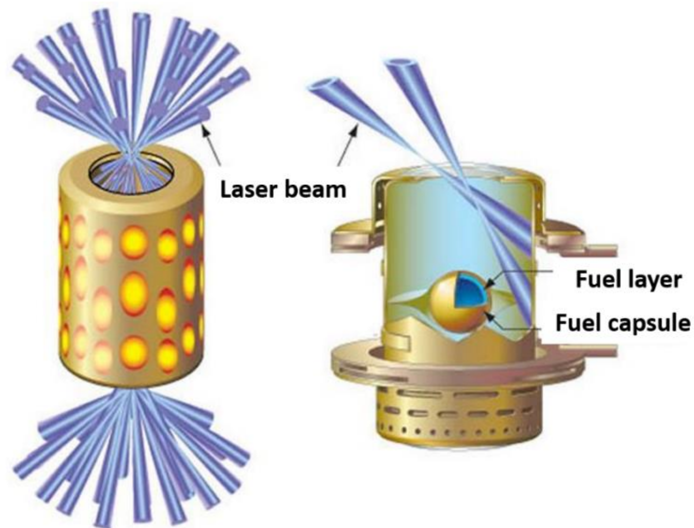

Figure 1-5 NIF schematic of inertially confined fusion process. 192 laser beams are directed to a dime size, gold cylinder heating the fuel pellet [20].

by the NRT equations is shown in Equations 1-2. NRT dpa is then obtained by normalizing the number of defects in a volume with the average volume per atom [22,23].

$$N_d = \begin{cases} 0, & T_d < E_d \\ 1, & E_d < T_d < \frac{2E_d}{0.8} \\ \frac{0.8T_d}{2E_d}, & \frac{2E_d}{0.8} < T_d < \infty \end{cases} \quad \text{Eq (1-2)}$$

Figure 1-6 shows the thermal and displacement damage dose operating requirements of structural materials in current fission reactors and anticipated fission and fusion reactors. Additionally, a plot showing the estimated operating temperatures for structural materials with damage levels ranging from 10 to 50 dpa is shown in Figure 1-7.

The focus of these studies is on single crystal silicon carbide (SC SiC), with the understanding that fundamental research on irradiation effects on SC SiC will, to an extent, translate not only to SiC_f/SiC (SiC fibers in a SiC matrix) composites for nuclear, structural applications but also to the development of irradiation-effects models for other covalently bonded ceramics. Further, SiC is a promising candidate base-material for electrical devices in harsh environment applications, such as for flow and temperature sensors for MSRs and other nuclear reactors [24], Schottky diodes for electronics on inner solar system probes [25], and power processing units for solar electric propulsion systems [26]. SiC is also currently used as a cladding layer in tristructural-isotropic (TRISCO) fuel particles [27] and some point defects within the SiC bandgap are potential qubits for quantum computing [28]. Therefore, understanding how SiC responds to irradiation is of significant interest for several applications.

For applications involving extreme environments, the primary appeal of SiC is that it is mechanically and chemically stable and radiation resistant at elevated temperatures. SiC is a wide bandgap semiconductor with a large thermal conductivity. It is primarily covalently bonded with a decomposition temperature exceeding 2700 K [29]. The ionic character of the C-Si bond is ~8% and has sp^3 hybridization [30].

SiC may form into more than 150 polytypes, the most commonly utilized polymorphs being 3C, 4H, and 6H where the number denotes the number of repeating layers (stacking sequence) in the close-packed structures, and the letter symbols (C or H)

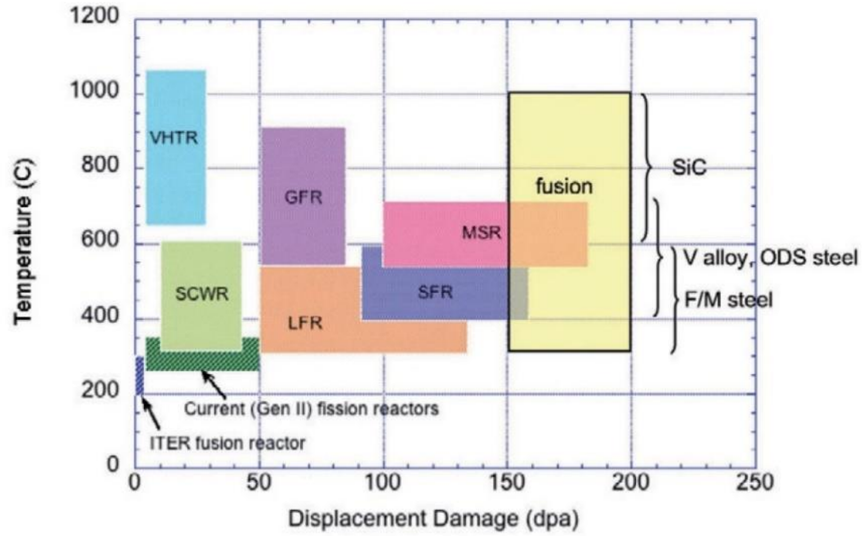

Figure 1-6 Dose and temperature requirements for structural materials for fission and fusion reactors [9].

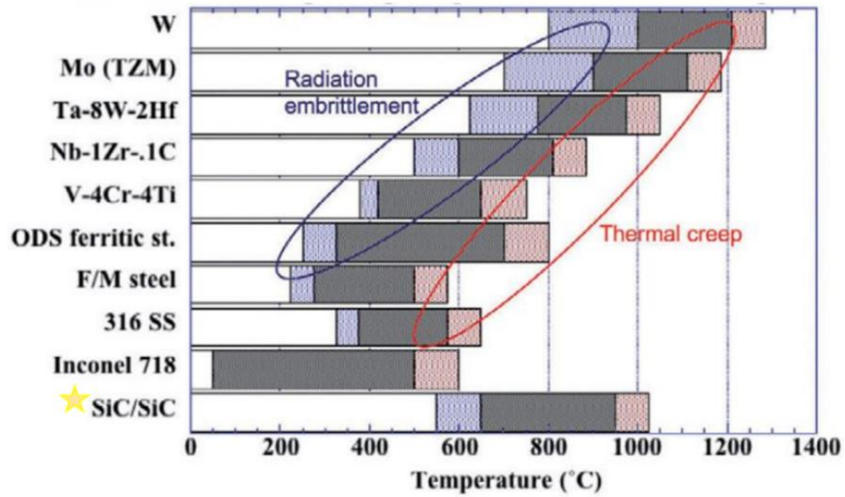

Figure 1-7 Estimated operating temperatures for nuclear structural material with 10 to 50 dpa damage levels [9].

denote the crystallographic systems (either cubic or hexagonal). Each layer in the stacking sequence consists of a closed-packed plane of Si atoms and a close-packed plane of C atoms nested together. SiC unit cells are shown in Figure 1-8 [31,32]. All polytypes are built based on tetrahedra SiC_4 and corner-sharing CSi_4 and differences are due to variations in the stacking sequences of bonded Si-C bilayers [30]. 3C-SiC is the primary polytype considered for structural nuclear applications, i.e., as the crystal structure of matrix for SiC_f/SiC composites and as the cladding for TRISO fuel, while 6H- and 4H-SiC ar preferred for electronics applications due to their larger bandgaps (~3.0 and 3.2 eV, respectively compared to 2.2 eV of 3C-SiC) [33]. However, because of the negligible differences in SiC polytype (3C, 4H, and 6H) response to irradiation displacement damage, predictive model development for irradiated behavior on a single polytype can be applied to the others [34].

1.5 Transmutation reaction and dopant effects in SiC

Plasma facing materials (PFMs) in fusion reactors are directly exposed to the plasma in the reactor. These materials are exposed to a wide energy range of ions and neutrons, extreme heat, and high electromagnetic flux that work to erode the surface of PFMs [35,36]. Despite these extreme conditions, it is generally considered that fusion reactor first wall components need to be functional for a minimum of five years [37]. A higher proportion of fusion neutrons are significantly higher energy (E_{max} = 14.1 MeV, eq 1-1) when compared to fission neutrons (E = 0.1-2 MeV). The higher energy neutrons better facilitate the production of solid and gaseous transmutation products. Plasma facing SiC components may produce helium at rates up to 130 appm/dpa while the helium production rate per dpa in SiC for a typical fission neutron spectrum is reported to be approximately 2.5 appm/dpa [38]. The lowest threshold energy for (n, α) reactions in carbon is ~6 MeV and ~3 MeV in silicon. In functional, SiC-based fusion materials, a significant production of helium content is made through the (n, n3α) reaction with carbon (~8 MeV threshold energy) [39,40]. Accumulation of excess gaseous products in irradiated materials can lead to significant alterations in mechanical properties. Due to the high He diffusivity and low

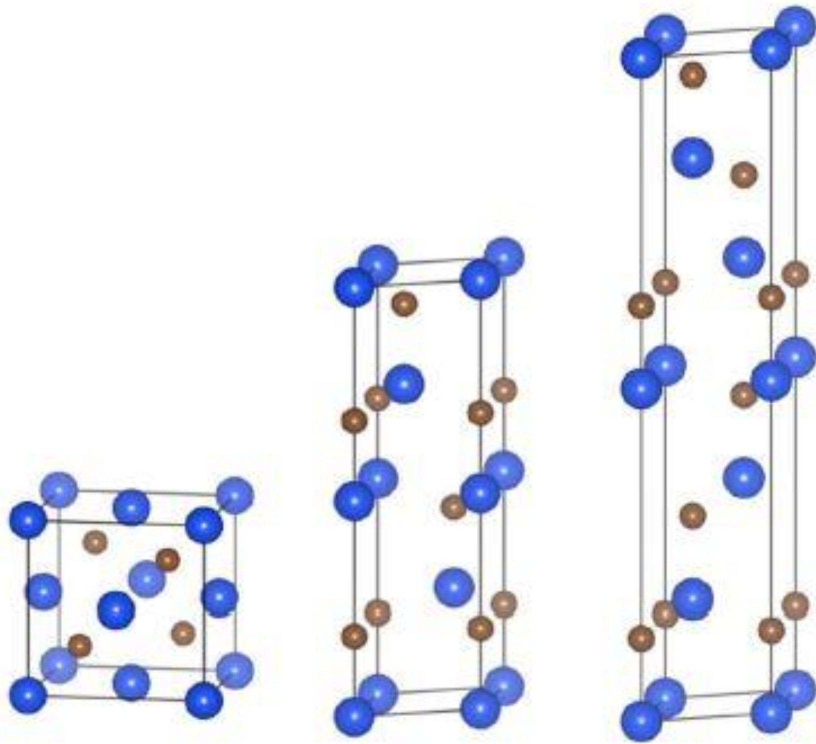

Figure 1-8 Unit cells of 3C-, 4H-, and 6H-SiC [32].

solubility in SiC, He atoms tends to agglomerate and form cavities or bubbles at elevated temperatures ($0.5T_m$) causing volume swelling and embrittlement [35,41–44]. Figure 1-9 below illustrate the He and H production rates as a function of depth from plasma face for magnetically and inertially confined fusion reactor [35].

Energetic neutrons also invoke solid transmutation products in SiC. The most concerning of which is the ^{26}Al isotope, produced via either of the two processes described in Equations 1-2 and 1-3.

$^{28}Si(n, d) \rightarrow {}^{27}Al(n, 2n) \rightarrow {}^{26}Al$ Eq (1-2)

$^{28}Si(n, n'd) \rightarrow {}^{27}Al(n, 2n) \rightarrow {}^{26}Al$ Eq (1-3)

This isotope is long-lived with a half-life of 726,000 years and radiologically hazardous [43]. Additionally, solid transmutation products may act as n- or p-type dopants in SiC, altering electrical properties in the material. Metallic transmutation products can also lead to changes in chemical properties in SiC, facilitating corrosion and oxidization [42]. Table 1-1 below compares the primary transmutation products produced in SiC from fast neutrons created in magnetically and inertially confined fusion systems and the High Flux Isotope Fission Reactor (HFIR).

While transmutation reactions induce unwanted impurities into a material, SiC is often intentionally doped to alter its electrical or optical properties. SiC is an appealing semiconductor material for high-power electrical and micromechanical devices for harsh environment applications, as SiC-based devices can operate at much higher temperatures than traditional semiconductor-based electronics. Processing techniques, particularly selective doping, are necessary for developing functional SiC devices. In SiC, both the silicon and carbon atoms have four valance electrons, so doping with n-type, donor dopants (atoms with more than four valance electrons) or p-type, acceptor dopants (atoms with less than four valance electrons) improves the conductivity of the doped region as electrical current can more easily flow, allowing for the creation of n^+p and p^+n junctions which then can be used to fabricate devices.

Generally, selective area doping of SiC must be done via ion implantation due to limitations in diffusion coefficients of dopants in SiC making other doping methods, such

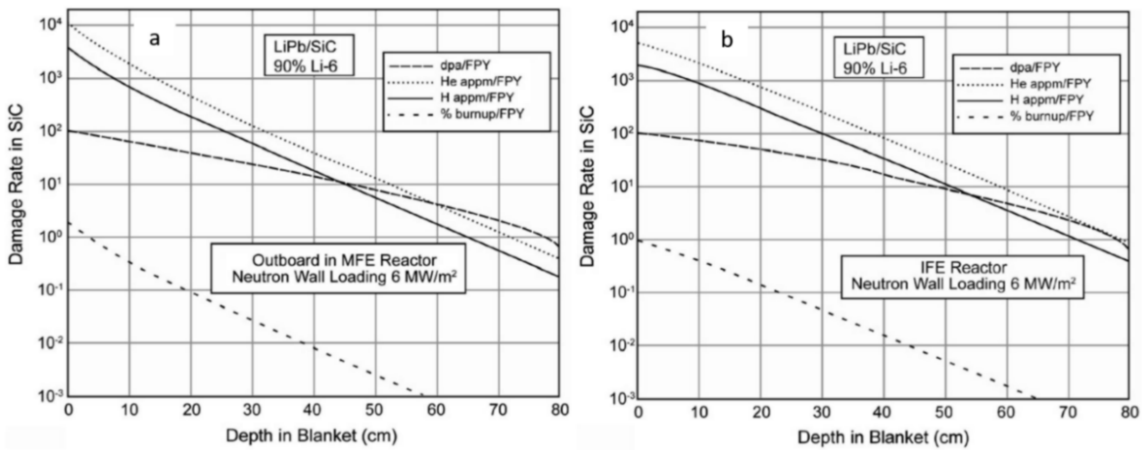

Figure 1-9 Gaseous transmutation production (appm/full power year) and damage rates verses depth from plasma for (a) magnetic fusion energy reactor and (b) inertial fusion energy reactor [35].

Table 1-1 Concentration in appm of solid transmutation products produced in SiC for fluences of 10^{23} n/cm^2 from magnetic and inertial fusion energy reactors (MFE and IFE) and the High Flux Isotope Fission Reactors (HFIR), along with the minimum threshold neutron energy for formation. Data from ref. [31].

	MFE fusion reactions	IFE fusion reactions	HFIR fission reactions	**Threshold neutron energy for formation (MeV) [31]**
Neutrons with E > 0.1 MeV	75.5%	71.9%	24.3%	
Be	851	482	4.5	**6.2**
Mg	2232	1189	8.7	**2.7**
Al	16.4	19.6	0.1	**4.0**

as vapor deposition, impractical in already formed substrates [45]. Ion implantation utilizes low energy ion beams to implant precise concentrations of dopants into target materials. Implantation in SiC is often done at elevated temperatures (500 to 1000°C) to avoid complete amorphization, as it is challenging to anneal fully amorphous SiC back to a pristine, single crystal of the desired polytype. After implantation, dopant atoms sit largely in interstitial lattice sites, so added electrons or holes do not readily alter material conductivity. Therefore, to make ion implanted doped SiC functional, post-implantation heating up to 1800°C is required to electrically activate the dopants, i.e., move the implanted ions to substitutional lattice sites. Post implantation heating also acts to anneal defects produced by ballistic collisions during implantation [46].

Limitations in commercial SiC electrical devices are largely due to the high temperatures required to create functional dopants, also prolonged thermal annealing leads to SiC surface degradation caused by the sublimation of Si surface atoms [47]. Because of this, athermal, laser activation of dopants has also been studied. Ahmed et al. achieved activation of RT implanted N and Al dopants using a pulsed excimer laser [48]. However, there are shallow depth limitations of laser induced electrical activation techniques. The most common SiC donor dopants are nitrogen and phosphorus, while common acceptor dopants are aluminum, boron, and gallium. Carrier ionization energy, atomic size, and solubility are the primary factors in dopant choice.

CHAPTER TWO
LITERATURE REVIEW

2.1 Ions used as a surrogate for neutron irradiations

The core structural components in Gen IV sodium fast reactors must be able to withstand damage doses up to 200 dpa at temperatures up to 400°C. Fusion structural components must be able to withstand an estimated 200 dpa at temperatures up to 1000°C [9,49,50]. So, in order to develop and characterize materials for safer, cost-effective, and more powerful nuclear reactors, fully understanding how materials respond to high radiation doses at elevated temperatures is necessary. Neutron irradiation studies are performed by placing samples in test reactors, such as HFIR, for irradiation followed by sample characterization. However, it is experimentally difficult to analyze radiation effects at very high doses as current test reactors are limited to damage rates below 20 dpa/year, making high dose experiments impractical and high dose-rate studies impossible [49,51]. Because of this, ion irradiation produced with particle accelerators is often used in-lieu of neutrons for high dose experiments. Ions can be produced and controlled significantly easier than neutrons, and ion damage rates are up to 10^4 times greater than test reactor neutrons. Additionally, in ion accelerator experiments, temperature, dose, and flux are more controlled, characterization can often be performed in situ, and because most ion-solid interactions do not result in activated samples, unlike in neutron-solid interactions, post-irradiation characterization is more feasible and cost effective [49,51,52]. Ion irradiation can also be used to study and simulate damage produced by primary knock-on atoms (PKAs). PKAs are energetic atoms displaced by fission and fusion neutrons that produce atomic collisions [52].

While significantly more practical than reactor experiments, ions are not a perfect surrogate for neutrons for several reasons:

(1) Ions have charge which interact with the electrons of a target material, making the collision cross sections of ions greater than that of neutrons. Ions lose energy through both electronic and nuclear energy loss, and the damage profile from an

energetic ion is non-uniform as the energy loss processes of the ion changes throughout the ion path. Neutrons, however, are electronically neutral and do not interact with the electrons in a target material, resulting in uniform damage profiles that span over long (≈ mm's) distances [49].

(2) Because ions are produced as a beam via particle accelerators, the energy of the ions produced is constant. This is directly in contrast with neutrons produced by reactors, the energy of which varies over multiple orders of magnitude, resulting in a more complex damage profile.

(3) Ion irradiation can achieve the same doses in hours as neutron irradiation in years. The effects of extreme difference in dose rates between ions and neutrons is not entirely understood [49,52]. The effects of dose rate on radiation-induced segregation (RIS) and void growth in metallic alloys may, in-part, be resolved with the invariance theory by Mansur. The theory states that RIS and void growth from accelerator irradiation would match RIS and void growth from reactor irradiation, if the accelerator irradiation was performed at a corresponding elevated temperature [53]. However, this effect only holds for early stages of radiation-induced degradation and there is still much uncertainty about dose rate effects in compositionally complex and covalently bonded materials, and only limited experiments have been performed on these processes [54,55].

There are several issues related to simulating neutron damage with ions that must be considered before making predictions on how a material may behave over long-term exposure in extreme nuclear environments. However, ion irradiation experiments allow for the study of high-dose and dose-rate effects on microstructure evolution and facilitate the ability to isolate and study distinct irradiation processes, making ion irradiation experiments a necessary component for nuclear materials characterization and fundamental irradiation effects studies.

2.2 Ion Energy Deposition

Energetic ions lose their energy in a target material through two primary processes, nuclear and electronic, that are quantified as the average energy loss of a particle of a given energy per unit pathlength of the ion [39]. Ion energy portioning depends on the target material, the energy of the ion, and the ion species, as shown in Figure 2-1 and Figure 2-2.

2.2.1 Nuclear Energy Loss

Nuclear energy loss (S_n) is the transfer of kinetic energy via elastic scattering collisions to atomic nuclei when an energetic ion traverses through a target. In solid materials, the absorption of nuclear energy by a target atom can result in the permanent displacement of the atom and formation of a vacancy only if the transferred energy is above the displacement threshold energy, E_d, of the lattice atom. Target atoms that are displaced by an incident ion are called primary knock-on atoms (PKAs). The transfer of kinetic energy from the PKAs to other atoms can generate further atomic displacements, which in turn can create additional displacements, resulting in a cascade of collisions (or collision cascade) that creates a local concentration of lattice vacancies and interstitials. If the transferred energy is below the E_d of the target atom, then the atom will only be temporarily displaced, and the energy from these interactions is largely dispersed by lattice vibrations (i.e., phonons).

Modeling elastic collision reactions is done using classical physics where relationships between ion energy, columbic forces, incident angle, target density, and mass ratio of ion and target nuclei are used to determine energy transferred in a scattering event. The kinetic energy transfer (T) resulting from an elastic collision is described by the relationship in Equation 2-1.

$$T = \frac{2m_1m_2}{(m_1+m_2)^2}E_0(1-cos\theta^*) \qquad \text{Eq (2-1)}$$

Here, E_0 is the projectile energy, m_1 is the projectile mass, m_2 is the target nucleus mass, and θ^* is the scattering angle [52]. The Stopping and Range of Ions in Matter (SRIM) code [57] is one of the most widely used applications for determining both nuclear and electronic energy loss values for ions. For elastic ion-target interactions, SRIM utilizes the universal

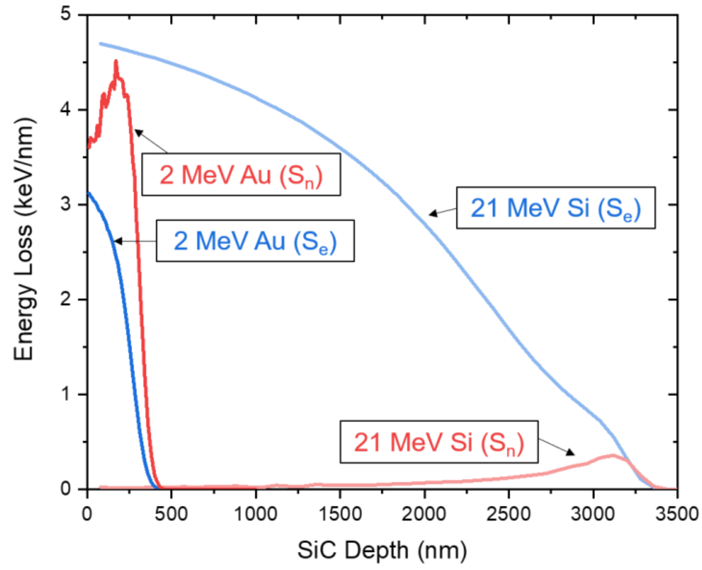

Figure 2-1 SRIM predicted electronic and nuclear energy loss per unit depth for 2 MeV Au and 21 MeV Si ion in SiC.

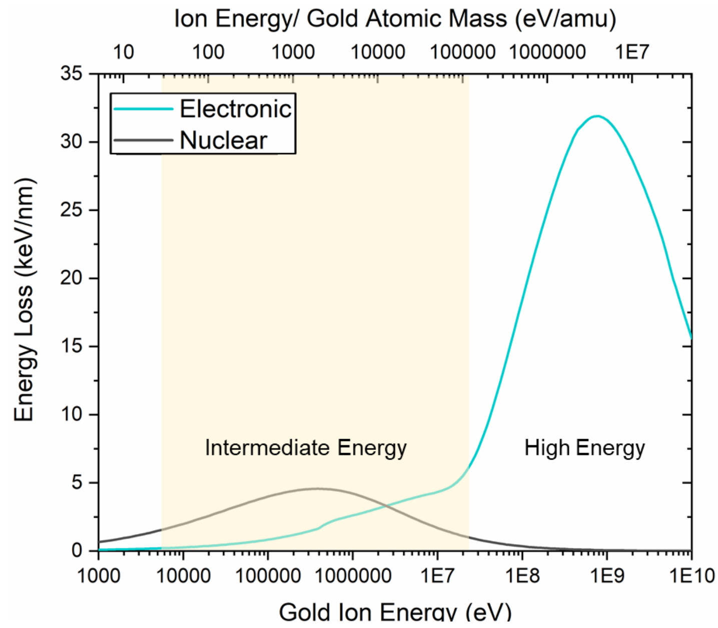

Figure 2-2 Energy loss mechanisms as a function of gold ion energy and energy per gold atomic mass in SiC.

Ziegler, Biersack, and Littmark scattering potential (ZBL potential) [58] to calculate the elastic energy transfer and scattering angle from binary nuclear collisions between moving and stationary atoms [57].

The SRIM code has the option of predicting damage profiles with two different methods: (1) modified Kinchin-Pease (quick TRIM) and (2) detailed calculation with full cascade damage (full-cascade TRIM). Both methods are based on a binary collision approximation and utilize a Monte Carlo approach to account for energy transferred to electrons and stochasticity in the transfer of energy from incident ions to PKAs. Furthermore, both methods utilize the same SRIM predicted electronic stopping powers (S_e) and ZBL scattering potential for incident ions in the target material. Consequently, both methods yield statistically identical ion range profiles and PKA energy spectra [57]. The primary difference between quick and full-cascade TRIM is how PKA energy dissipation is calculated. Under quick TRIM simulations, the energy loss to electrons, damage energy (T_{dam}), and the number of atomic displacements (ν) for a given PKA is calculated based on the semi-empirical Norgett, Robinson, and Torrens (NRT) model [23] given by Equation 2-2.

$$\nu_{NRT} = \frac{0.8 \cdot T_{dam}}{2 \cdot E_d} \qquad \text{Eq (2-2)}$$

On the other hand, full-cascade TRIM simulations utilize SRIM S_e values and ZBL scattering potentials for the target atoms within the material, and Monte Carlo approach to follow the electronic and nuclear energy transfers for each PKA and all additional atomic recoils until their energy is less than the E_d value for the atoms in the target. Thus, in full-cascade TRIM, the total average number of displaced atoms, ν, is found by tabulating the vacancies and replacement events over each ion's trajectory and averaging over all incident ions in the simulation. While quick TRIM is not recommended by the code authors for calculating displacement events in materials, it does have a marginal validity for monoatomic materials; however, as noted in a recent review [59], full-cascade TRIM provides a more accurate description of the displacement process for all materials.

Nuclear energy loss is the primary energy loss mechanism for PKAs, ions at their end of range (EOR), as well as for lower energy ions with energy to mass ratios (E/m) less

than 0.01 MeV/amu. Nuclear energy loss is also generally more damaging to target materials and associated with typical radiation damage, such as void swelling and radiation embrittlement.

2.2.1 Electronic Energy Loss

Electronic energy loss (S_e) is the inelastic transfer of energy from incident ions to target electrons (i.e., ionization) creating hot electrons that initiate a cascade of electron-electron energy transfer processes. Eventually (<100 fs) most of this energy is transferred to the atomic lattice via electron-phonon coupling, resulting in a highly localized thermal spike [60]. This inelastic thermal spike can result in local phase transitions via melt-quench/recrystallization processes, local defect annealing, and enhanced defect and atomic diffusion. The intensity of the thermal spike is generally greater in ceramic materials compared to most metals, as the electron mean-free path is smaller and electron-phonon coupling is stronger in ceramics. S_e is the dominant energy loss mechanism for intermediate and higher energy ions. Figure 2-2 illustrates the stopping power for gold ions in SiC as a function on ion energy. At low energies, nuclear energy loss is the dominant energy deposition mechanism; while at higher energies ($E/M > 0.1$ MeV/amu), electronic energy loss is the more prevalent energy deposition mechanism. However, it should be noted that some of the nuclear energy loss to PKAs is transferred to electrons by the PKAs and secondary recoils, so a clear separation of energy partitioning to electrons and displacement production cannot be determined solely by the S_e and S_n values of the incident ions.

Isolated electronic energy loss effects can be studied using swift heavy ions (SHI), which are defined as ions with energy to mass ratios generally greater than 0.1 to 1 MeV/amu and have largely negligible nuclear energy loss effects. These ions can be used to alter the microstructure of some materials via localized melting, quenching, and amorphous recrystallization along the ion path, resulting in the formation of ion tracks which are long, straight, and can be engineered to precise lengths for different ions and target materials [34,61–63]. Electronic energy loss models require greater complexity than

two body, elastic S_n models as dynamic charge and energy effects alter S_e behavior. SRIM code calculates S_e by extrapolating fits of experimentally derived S_e values [57].

While all ion-solid interactions involve some degree of both nuclear and electronic energy loss, the two energy loss pathways have historically often been simplified as entirely separate processes, resulting in knowledge gaps on the effects of energy transfer mechanisms for intermediate energy ions where the coupling of energy loss dissipation processes can exhibit significant effects. This is discussed further in section 3.1.

2.2.3 Nomenclature

There are multiple methods to define and quantify inelastic and elastic energy partitioning from ions. In this thesis, different terms for the energy deposition are used, and while these groups of terms for each deposition process are conceptually similar, they are not synonyms and are not calculated the same way. This section defines the terms used in this work.

Elastic Energy Deposition Terms [59,64–66]:

Nuclear Energy Loss (S_n). Nuclear energy loss is the average energy transferred per unit depth from incident ions to atomic nuclei in a target material due to elastic scattering processes.

Damage Energy. Damage energy is the total elastic energy that goes into creating displacements. It is also calculated as the average energy deposited per unit depth. Damage energy is given by the nuclear energy loss of the incident ion minus all the energy loss to electrons by the PKAs and recoils, which is equivalent to the total amount of energy dissipated to phonons from both incident ions and resulting recoils [66].

Inelastic Energy Deposition Terms [59,64–66]:

Electronic Energy Loss (S_e). Electronic energy loss is the average energy transferred from incident ions to target electrons per unit depth in a target material.

Ionization Energy. Ionization energy is a measure of the total inelastic energy deposited to electrons by incident ions. As with damage energy, it is measured as the average energy deposited per unit depth. Ionization energy is determined by the total amount of energy dissipated to electrons from both incident ions and resulting recoils.

General Energy Deposition Terms [59,64–66]:

Total Energy. Total energy is the sum of the ionization and damage energy. It measures the total amount of energy deposited into a material both from incident ions and resulting recoils. It is measured as energy deposited per unit depth.

Actual electronic energy loss and ionization energy values along with S_n and damage energy values have the largest variance with low energy ion irradiations and at the EOR of ions. Under such conditions, PKAs have significant electronic energy losses, i.e., some of the elastic energy transferred initially from incident ions is then deposited inelastically from the resulting PKAs. There is then a reduction of value going from nuclear energy loss to damage energy and an increase in value moving from electronic energy loss to ionization energy values. Figure 2-3 gives the SRIM predicted S_e, S_n, ionization energy, and damage energy values for 21 MeV Ni ions traversing through SiC.

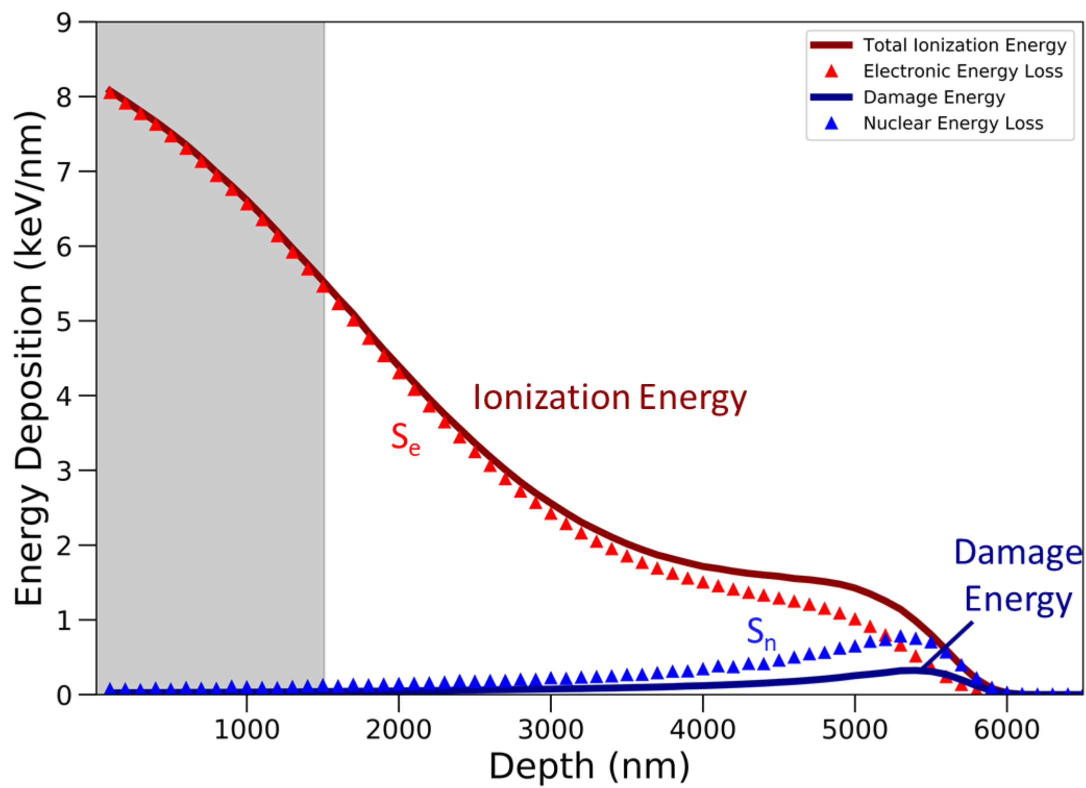

Figure 2-3 SRIM predicted energy partitioning processes of 21 MeV Ni traversing through SiC. Differences between inelastic and elastic processes are largest for the EOR of the ions, where much of the energy transferred to PKAs is deposited inelastically.

CHAPTER THREE
REVIEW OF PREVIOUS IRRADIATION EFFECTS IN SIC STUDIES

3.1 S_e Annealing During SiC Irradiation

During ion irradiation of SiC, it is established that S_e largely acts to anneal both damage induced by S_n along the ion trajectory, as well as pre-existing defects. This was first revealed in very energetic swift heavy ion (SHI) irradiation. These types of irradiations are associated with the production of ion tracks in ceramic materials, formed from localized melting and quenching around the ion path. However, in SiC there are no known irradiation conditions that cause ion track formation, which was historically attributed to the high thermal conductivity (~350 W/m-K) from the short electron-lattice mean free path in the material, allowing for thermal energy from S_e to rapidly dissipate radially, with little effect on the lattice [67–69]. But in the early 2000's, experiments with SHI irradiation of pre-damaged SiC verified that S_e from high energy irradiations facilitate local annealing along the ion path in the material. One of the earliest reports of SHI induced annealing of SiC was published Jiang et al. [70] who found that the nearly amorphous region of damaged 6H-SiC was reduced following a 50 MeV I irradiation. Benyagoub et al. [71] then reported that irradiation of 6H-SiC, pre-damaged to ~30% disorder, with 827 MeV Pb ions resulted in almost full annealing at room temperature, as well as significant, but not complete, recrystallization of fully amorphous SiC. Their results are shown in Figure 3-1. Annealing effects by SHI irradiations on pre-damaged SiC are presently well established and have also been observed with 167 MeV Xe ions at both 500°C [72] and RT [73], 870 MeV Pb ions at RT [74,75], and 910 MeV Xe ions at RT [76]. Table 3-1 summarizes the material, pre-damaged conditions, and annealing results for several SHI induced recovery studies. These studies found that S_e-induced annealing, while extremely effective for partially amorphized or small regions of amorphization, is not as effective for large regions of completely amorphized material, indicating that S_e annealing is dependent on the presence of a crystalline scaffold.

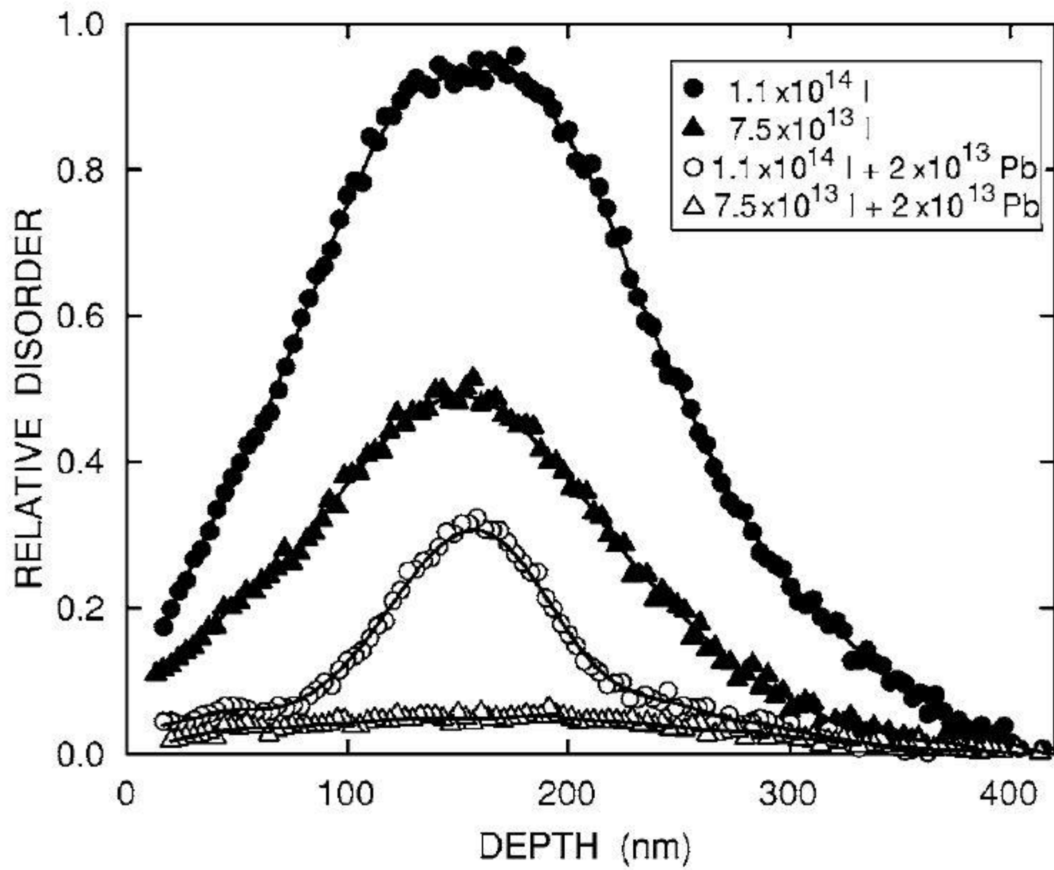

Figure 3-1 Si lattice damage profiles for SiC pre-damaged from 700 keV I ions then annealed with 827 MeV Pb ions (S_e ~33 keV/nm). Fluence units are in ions/cm^2 [71].

Table 3-1 Summary of experiments using SHIs to anneal pre-existing damage in SiC. The S_e values for the SHI range from 20-33 keV/nm.

Study	**SHI species and energy**	**T_{irr}**	**Pre-damaged state**	**Annealing Overview**	**Material**	**Charact-erization**
[72]	167 MeV Xe	500° C	Amorphized from surface to 230 nm	Amorphous region shrunk	Polycrystalline SiC	Raman, TEM
[73]	167 MeV Xe	RT	Partially amorphous region at 10 keV He damage peak	Damage recovery on partially amorphous region boundaries	4H-SiC	TEM
			Amorphized surface layer from 220 keV Ti irradiation	No detected recovery		
[74]	870 MeV Pb	RT	Fully amorphous surface layer to 50 nm	Amorphous region shrunk	3C-SiC	RBS/C
			Partially amorphous layer, max disorder fraction ~0.95	Damaged region shrunk, max disorder fraction ~0.60		
[75]	870 MeV Pb	RT	Fully amorphous surface layer	Recrystallization at amorphous region boundaries	3C-SiC	RBS/C, TEM
			Partially amorphous, onset amorphization at damage peak	Recrystallization along entire damage area		
[76]	910 MeV Xe	RT	Max disorder fraction ~0.60 at damage peak	Annealing of disorder, max disorder fraction ~0.12	6H-SiC	RBS/C
[70]	50 MeV I	RT	Near fully amorphous at damage peak, max disorder fraction ~0.92	Recrystallization at amorphous region boundaries	6H-SiC	RBS/C

Later studies on interactions between coupled S_e and S_n in single SHI irradiations found that there is a competing relationship between the energy loss processes. A report by Audren et al. [76] found that nanostructured 3C-SiC and SC 6H-SiC irradiated with 910 MeV Xe ions at room temperature would not amorphize even at dpa doses far exceeding the total amorphization threshold in SiC for lower S_e irradiations, as shown in Figure 3-2. Sorieul et al. [77] studied this further, using UV-visible optical and micro-Raman spectroscopy to analyze the formation of point defects resulting from SHI irradiations (106 MeV Pb, 332 MeV Ti, and 2.7 GeV U ions). They reported that isolated point defect concentration increases with dose, where the highest tested fluence was $2x10^{12}$ cm^2, ultimately altering optical and electrical properties [77].

While anticipated, S_e annealing effects from lower or intermediate energy (E ~ tens of MeV) ion irradiations were not fully established until relatively recently. Zhang et al. [78] reported a 'surprisingly low' threshold in S_e at ~1.4 keV/nm for annealing processes on pre-existing defects in SiC. For reference, this corresponds to Si PKAs or ions with energies above 750 keV and C PKAs or ions with energies above 850 keV. Thus, under most intermediate ion irradiation conditions, S_e effects are present. However, as with SHI annealing, S_e-induced recovery from intermediate energy ions is more effective for lower initial damage states. The higher disordered materials likely have more thermally stable, complex defects, such as clusters or amorphous microdomains, compared to less disordered materials. This effect is shown in Figure 3-3 where the recovery induced by a range of ions is compared for two different pre-damaged states (fractional disorder of 0.72 and 0.36) [78].

The low S_e threshold for annealing effects in SiC leads to questions on the effects of competing S_e and S_n processes at intermediate ion energies, where both energy loss processes are spatially and temporally coupled along the ion trajectories, on defect production and damage evolution in SiC. Zhang et al. [34] performed and reported on an experiment where 4H-SiC was irradiated with 4.5 MeV C, 6.5 MeV O, 21 MeV Si, and 21 MeV Ni ions. The damage profiles resulting from the irradiations were compared at varying target depths in order to determine the dependence of disordering processes on

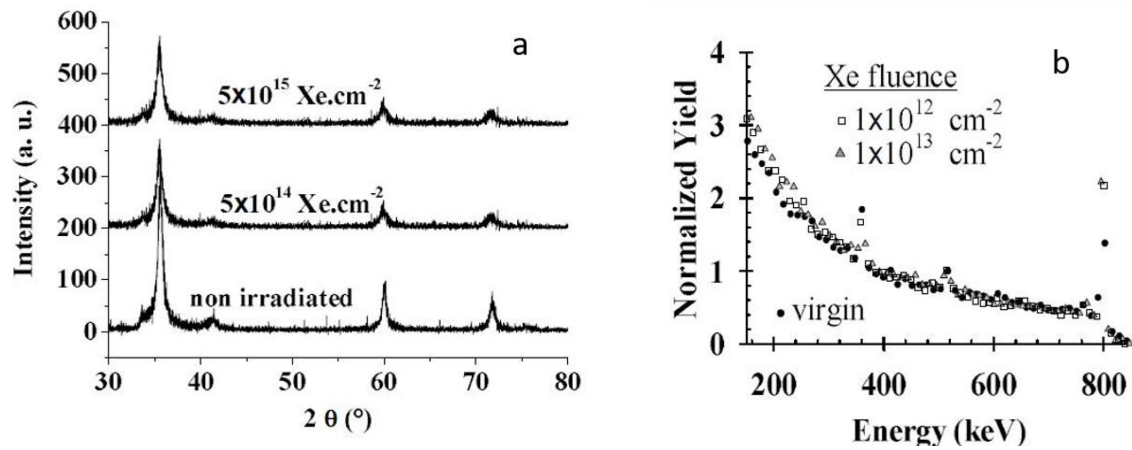

Figure 3-2 Plots indicating little detectable damage from irradiations (a) XRD results of nanostructured SiC irradiated with 95 MeV Xe ions, (b) RBS/C results of SC 6H-SiC irradiated with 910 MeV Xe ions [76].

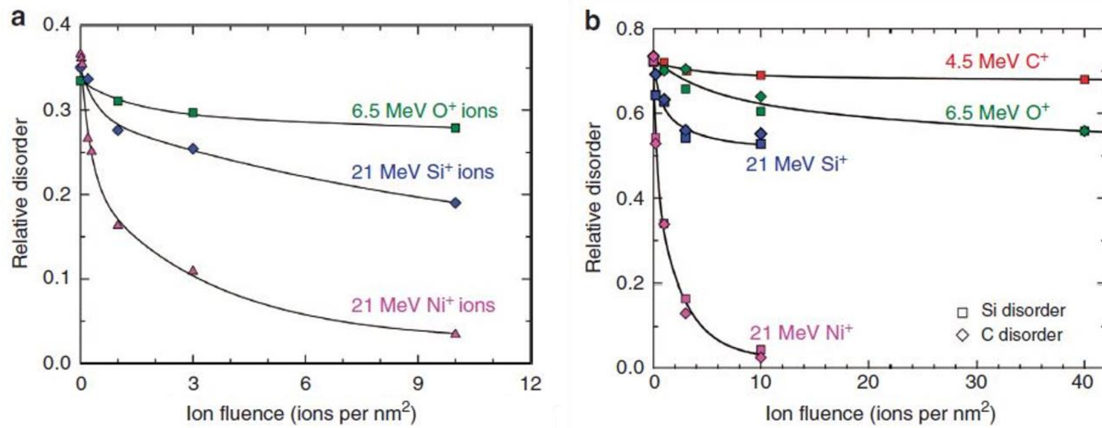

Figure 3-3 Annealing comparison for two initial relative disorder fractions: (a) 0.36 and (b) 0.72 [78].

S_e/S_n ratios. The resulting RBS/C profiles indicated that C, O, and Ni ion irradiations all generated noticeable damage to the first 1.5 μm of the pristine SiC, while the SiC spectra after the 21 MeV Si irradiation indicated no detectable damage. Given the high ratio of S_e/S_n for the C and O ions (388 and 336 at 650 nm) that is comparable to the S_e/S_n ratio value to 21 MeV Si (416 at 650 nm), it was expected that defect buildup at the surface region after irradiation from the C and O ions would also be insignificant. This discrepancy is attributed to differences in the thermal spike temperatures caused by the S_e deposition from the ions, as the S_e from the Si irradiation was at least twice the S_e values from the C and O irradiations. Xue et al. [63] furthered the study of the effects of coupled S_e and S_n by irradiating 3C-SiC with 1.5 and 5.0 MeV Si ions at incident angles of 7° and 60°, respectively, off the normal surface. As these ions penetrate the SiC samples, both the S_e/S_n ratio and the overall energies of the ions decrease, so by analyzing defect accumulation at varying depths, generalized effects of coupled S_e and S_n processes could be determined. Through measuring the fractional disorder as a function of displacement dose at different depths, a linear relationship between amorphization doses and S_e/S_n ratio was determined, as shown in Figure 3-4.

3.2 Temperature Effects

Under irradiation, SiC disorder rate decreases with irradiation temperature due to increasing dynamic recovery. Several irradiation-induced amorphization models for ceramics predict kinetic effects by adjusting parameters that have to do with the recovery rate of defects as a function of temperature [79]. Thermal annealing of irradiation damage is not strictly linear but occurs in stages that depend on defect type, concentration, and initial disorder fraction. Recovery stage I is associated with the onset of self-interstitial atom migration and recombination. Stage II corresponds to the migration of small interstitial clusters, and stage III is associated with vacancy migration and the annihilation of vacancies with interstitial clusters [52]. Weber et al. [80] reported the activation energy for recovery stages of the Si lattice in SiC after 2 MeV Au irradiations as: stage I is 0.3 ± 0.15 eV (150-300 K temperature range), stage II is 1.3 ± 0.25 eV (450-550 K temperature

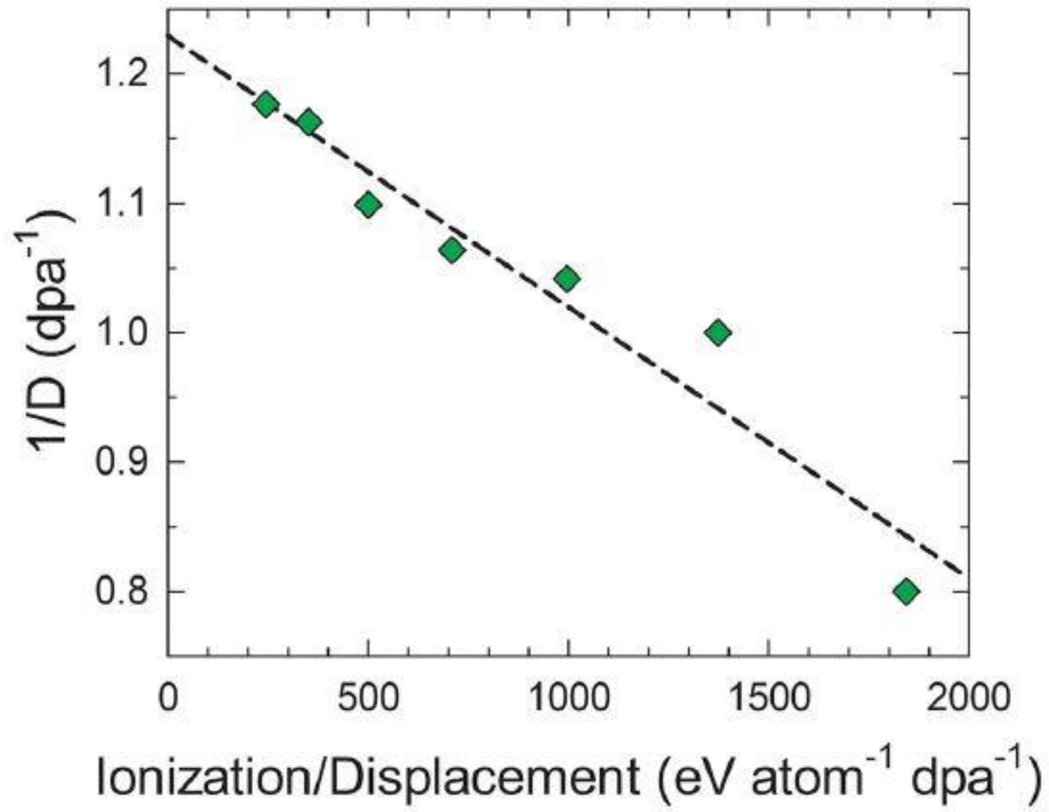

Figure 3-4 Linear dependence of critical amorphization dose (determined at disorder level of 0.97) on the ratio of ionization to dpa rate [63].

range), and stage III is 1.5 ± 0.3 eV (570-720 K temperature range). Figure 3-5 shows the isochronal recovery of disorder in the Si and C lattices after the 2 MeV Au irradiation. Complete thermal annealing of damage caused by heavier ions requires higher temperatures. This is attributed to the greater thermal stability of defects produced from larger ions, defect clusters and amorphous regions [81].

Dynamic thermal annealing also has a strong effect on disordering processes and has been observed in SiC irradiated at 170 and 300 K with 1 MeV Ar^+ ions [82], 170 and 300 K with 2 MeV Au^{2+} ions [81], 180 and 300 K with 550 keV C^+ ions [83], 150 and 190 K with 550 keV Si^+ ions [80]. Figure 3-6 shows how the disordering curve for 6H-SiC irradiated with 550 keV C ions reaches a fully amorphous state at a lower dose for lower temperatures. This same study reports that at temperatures close to or greater than $0.2T_m$, during the 550 keV C irradiation, dynamic annealing becomes large enough that total amorphization cannot be reached. This is referred to as a critical temperature for amorphization [83]. Similar critical temperatures for amorphization in SiC have been reported for 360 keV Ar^{2+} irradiations [84], 230 keV Ga^+ irradiations [85], 560 keV Si^+ irradiations [86], and 1.50 MeV Xe^+ irradiations [87], summarized in Figure 3-7.

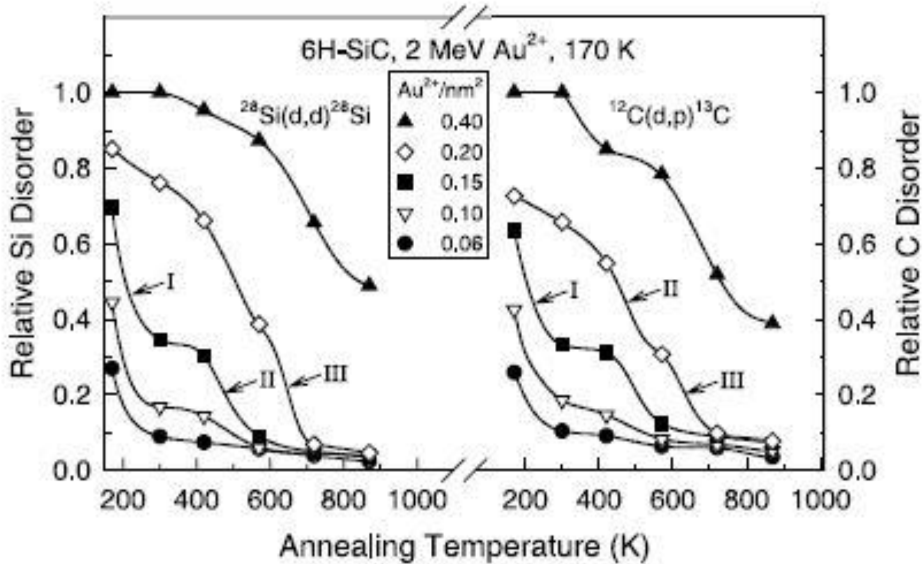

Figure 3-5 Annealing stages for SiC irradiated at 170 K with 2 MeV Au ions [81].

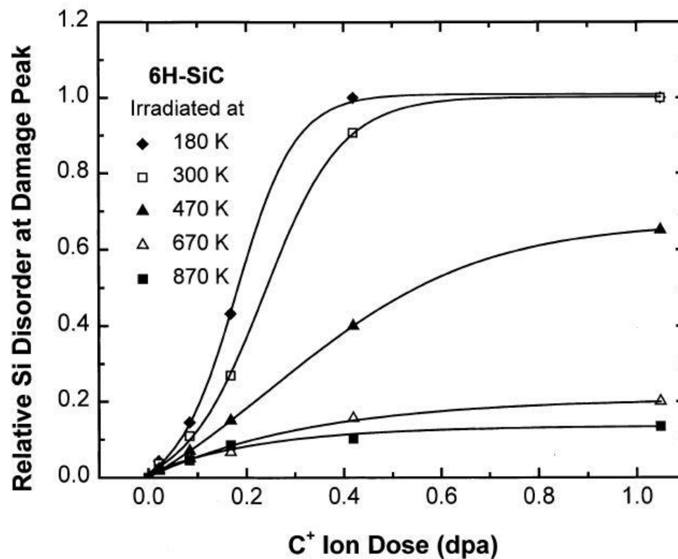

Figure 3-6 Disordering as a function of irradiation temperature [83].

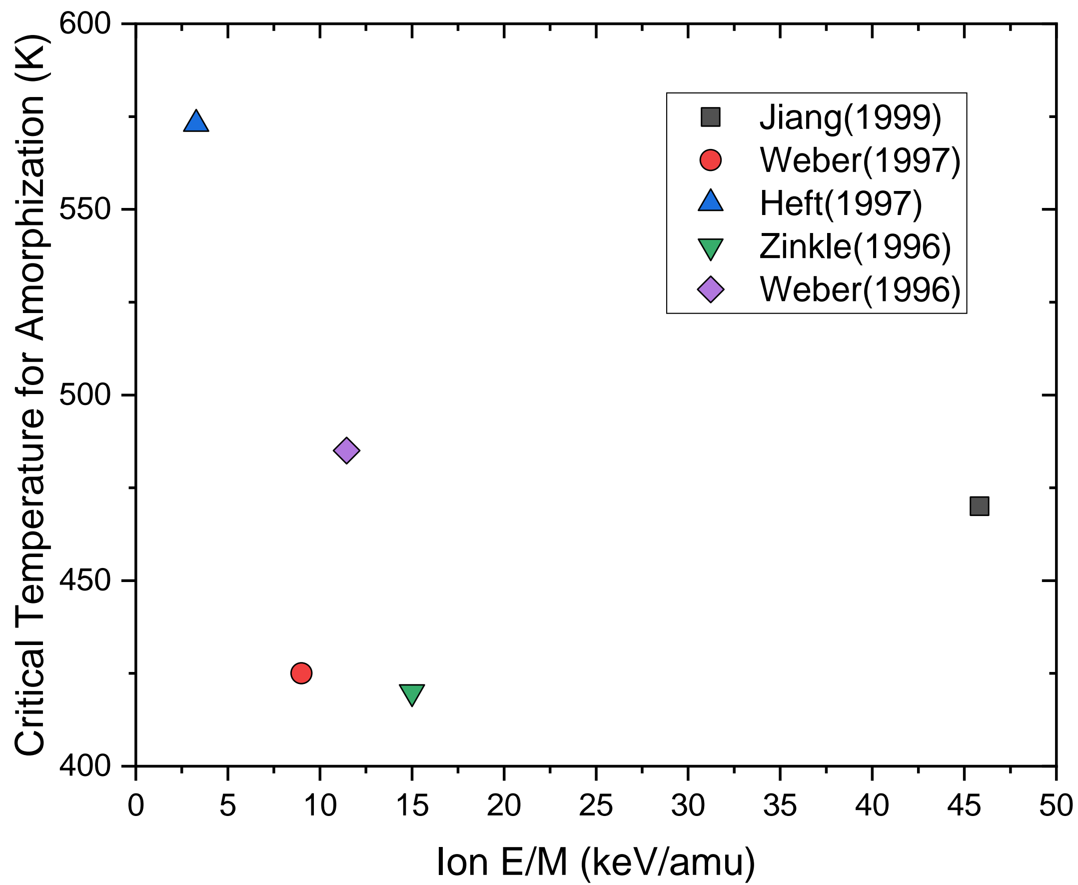

Figure 3-7 Critical temperature of amorphization dependence on incident ion E/M ratios [83-87].

CHAPTER FOUR
METHODOLOGY

4.1 Single Crystal SiC

All the materials used in this work were single crystal, n-type 3C- or 4H-SiC orientated along the <100> and <0001> axis, respectively. All the 3C-SiC samples used in the studies described in this work came from a single wafer that was produced and epi-polished to a surface roughness of < 10 Å by NovaSiC. 3C-SiC (also commonly referred as alpha-SiC) is the only possible cubic arrangement of SiC and is the most thermodynamically stable of the polytypes. It can be grown at temperatures < 1500°C, which make typical physical vapor transport (PVT) growth of 3C-SiC impossible [88,89]. Because of this, high quality, single crystal 3C-SiC used in this work was grown on a silicon substrate via chemical vapor deposition. The 3C-SiC layer on the Si substrate used was 3.8 μm thick. There is typically a significant lattice mismatch between the Si substrate and the 3C-SiC layer, leading to stress along the Si/SiC interface. However, characterization on damage accumulation on 3C-SiC was limited to depths < 1.5 μm, well away from effects induced by substrate/SiC layer stresses.

The <0001>-oriented, bulk, single crystal 4H-SiC wafers used in the studies were epi-polished and manufactured via PVT growth by Cree, Inc. The wafers are 257 μm thick and have nitrogen net doping density of 5×10^{14} cm^{-3} on the Si face and 1×10^{16} cm^{-3} on the C face, the lowest nitrogen doping density offered by Cree, Inc to minimize the impact of the nitrogen dopants on SiC resistivity. The bulk resistivity of the 4H-SiC wafer was tested and reported by Cree, Inc to be 0.012 ohm-cm.

All samples were cut using a diamond scribe to avoid lattice strain. Sample areas for implantation, irradiation, and any characterization were less than 12x12mm^2 and cut from bulk wafers.

4.2 Ion Irradiations

This work relies heavily on ion implantations, irradiations, and characterization to study ionization and displacement energy transfer mechanism effects on dopant and defect formation, migration, and activation. Rutherford backscattering spectroscopy in channeling geometry (RBS/C) is used in situ to characterize disorder and dopant concentration of a shallow depth range in single crystals. RBS/C spectra are compared with Stopping and Range of Ions in Matter (SRIM) code predictions.

4.2.1 Stopping and Range of Ions in Matter (SRIM) Simulations

The Stopping and Range in Matter (SRIM) code (v2013) is used for simulating damage in a target material to calculate depth profiles of displaced atoms and electronic and nuclear energy losses for each ion type and energy tested. SRIM is based on Monte Carlo simulations, where the binary collision approximation is used to calculate impact parameters of incident and resulting recoil ions.

As recommended by Weber et al. [59], full cascade simulations with the SRIM were performed with displacement energies of 20 eV for C and 35 eV for Si with a target density set to 3.21 g/cm^2 to determine the statistical depth profiles of displacement damage [90]. Quick TRIM simulations were used to calculate depth profiles of electronic and nuclear energy loss of the incident ions to obtain better statistics on the stochastic nuclear energy loss. Pysrim [91] is a python library created to automate SRIM calculations and analysis. This program was used to determine and plot the radial details of full cascade collision events along the ion ranges.

4.2.2 Ion Beam Materials Lab

All ion implantations, irradiations, and ion beam analysis in this work was performed at the University of Tennessee, Knoxville in the Ion Beam Materials Laboratory (IBML) [92]. The IBML facilities, shown in Figure 4-1, are made up of two ion sources, an injection and switching magnet, an electrostatic accelerator, three high energy beam lines, and four end stations. The two sources are: (1) the Alphatross, which generates helium ions via radio

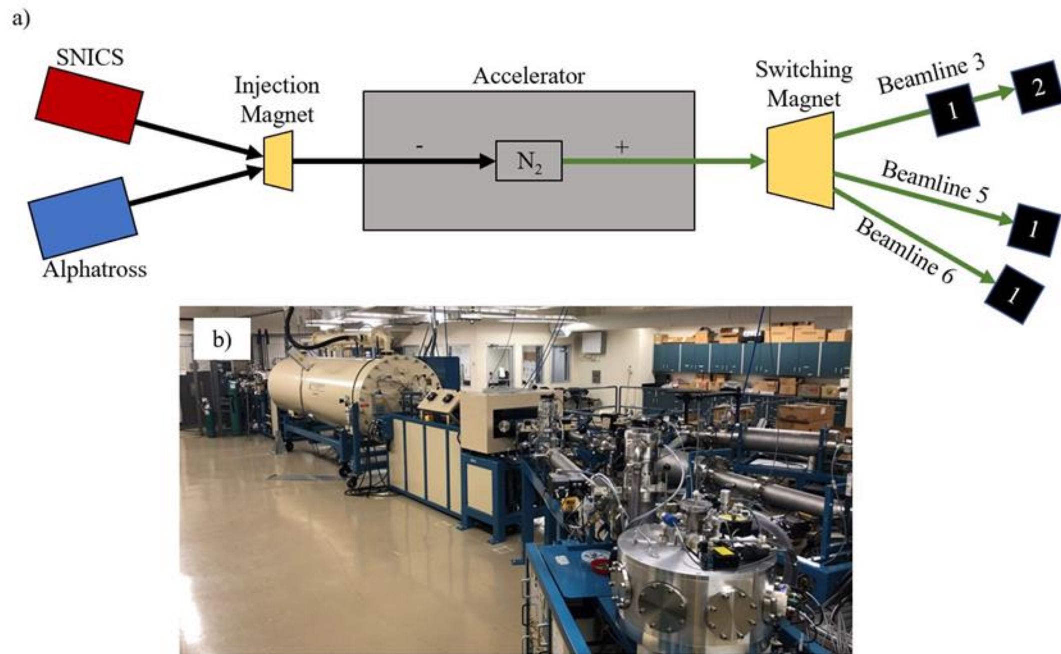

Figure 4-1 IBML (a) schematics and (b) photo from beamline 6 side of laboratory.

frequency charge exchange between the helium-gas ion source and Rb vapor and (2) the source of negative ions by cesium sputtering, or SNICS, that generates negative ions by cesium ion sputtering of a cathode. Both sources produce negative ions that are extracted and directed with the injector magnet into the 3.0 MV Pelletron accelerator, manufactured by the National Electrostatics Corporation (NEC). The negative ions are accelerated by the positive potential (up to 3 MV) at the center of the accelerator, where a charge exchange chamber, filled with nitrogen 'stripping' gas, strips electrons off the negative ions, creating positive ions of varying valance states. The positive potential then accelerates the positive ions to higher energies out of the accelerator towards the switching magnet, which directs the ions, of a chosen single charge state, to any of the end stations. The accelerator can produce 1 to 25 MeV energy ions with masses ranging from 1 to 197 amu. The end station chambers all operate at pressures below 1×10^{-7} torr and have different capabilities. Chamber 3-1 is connected to a closed loop, He-cooling system, allowing the chamber to reach temperatures as low as 30 K, so irradiations and characterization can be carried out at cryogenic temperatures. Chamber 3-2 has elastic recoil detection analysis (ERDA) capabilities. Chamber 5 is equipped with the most sophisticated manipulator of the IBML chambers, having three axes of rotation and translation which is optimal for channeling Rutherford backscattering spectroscopy characterization. Chamber 6 has both movable and fixed Si-detectors, allowing for varied back scattered ion detection configurations. Both chambers 3-2 and 5 have liquid N_2 connections for active temperature control and heating elements that allow controlled irradiation temperatures ranging from -123°C to 727°C.

Ion beam flux is predetermined and held constant throughout irradiations and implantations. The beam flux, Φ, is found based on Equation 4-1.

$$\Phi = \frac{I}{A \cdot q \cdot e} \qquad \text{Eq (4-1)}$$

Where I is the beam current as measured with a faraday cup, q is the charge state of the ions, e is the charge of an electron, and A is the beam area. During irradiations and implantations, ion beams are defocused and wobbled slightly to ensure uniform damage.

The irradiating area is controlled by two sets (one in the y-direction and one in the x-direction) of adjustable slits situated directly before the target chamber and the incident

angle of the beam or the orientation of the target, as shown in Figure 4-2. Beam current is typically directly proportional to area; however, when the beam area is enlarged due to projection (caused by changes in the incident beam angle) the current is not affected as the enlargement is caused by a projection of the beam.

4.3 Ion Beam Analysis

Ion beam analysis allows for detailed, in situ, and non-destructive characterization on irradiated and implanted samples. Rutherford backscattering spectroscopy is a common technique used for elemental and surface characterization, and, if done in channeling geometry, depth dependence of near-surface disordering can be determined.

4.3.1 Rutherford backscattering spectrometry (RBS)

RBS characterization is done by detecting ions that have been backscattered after colliding with surface and near-surface target atoms. The ratio of backscattered energy of ions to its incident energy, or the kinematic (K) factor, can be described with Equation 4-2 [93].

$$K = [(\frac{1}{m+M})(m \cdot cos\theta + \sqrt{M^2 - m^2 \cdot sin^2\theta})]^2 \qquad \text{Eq (4-2)}$$

Where M is the mass of the target ion, m is the mass of the backscattered ion, and θ is the scattering angle. A plot of K-factor for different incident ions masses is shown in Figure 4-3. Ions used for RBS are typically light; RBS at the IBML is almost exclusively done using He^+ ions with 2, 3, 3.5, and 4 MeV energies. The number and energy of backscattered He^+ ions correlate to the elemental composition of the target material as a function of depth. The basics of the ion-target interactions used for RBS analysis is shown in Figure 4-4.

Backscattered He^+ energy and counts are measured with a Si-detector set at a known angle from the target (25° in chamber 5-1 and 12° in chamber 6-1) [92]). The RBS spectra are plotted as the counts, which is a measure of the rate of backscattered ions at a given angle, as a function of energy or channel number, where each edge or peak corresponds to an element. Heavier target elements have higher backscattering cross-sections; because of this, RBS is especially effective at the detection of heavy elements with sensitivities on the order of a few parts per million. The depth capabilities of RBS

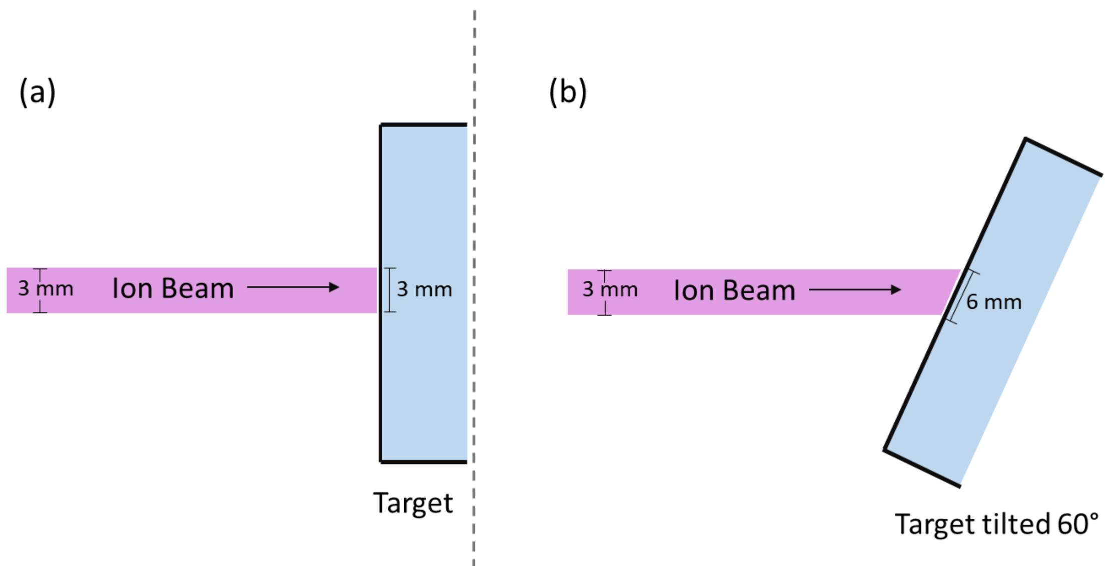

Figure 4-2 Schematic of ion irradiation area projection due to tilting of the target material. The area size due to projection in one direction is the beam size divided by the cosign of the angle of tilt.

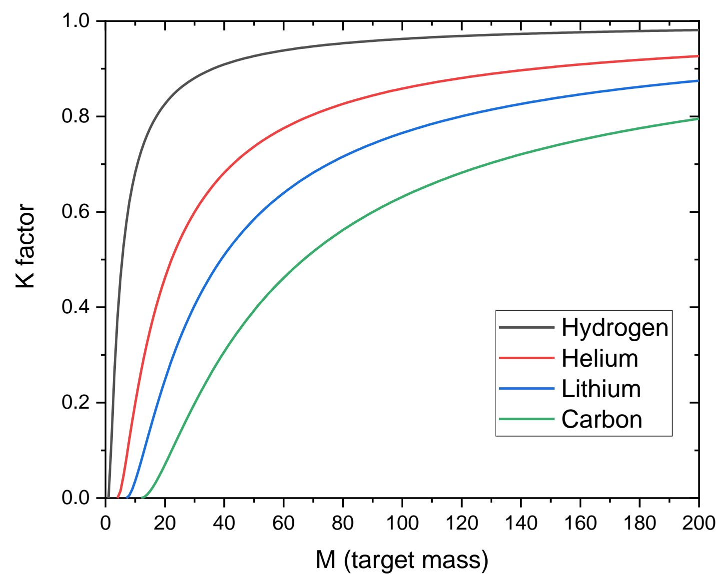

Figure 4-3 K-factor as a function of target mass at θ = 155°. The slope of the spectra is a measure of mass resolution. Note the greater slope for the lower mass targets, indicating improved mass resolution.

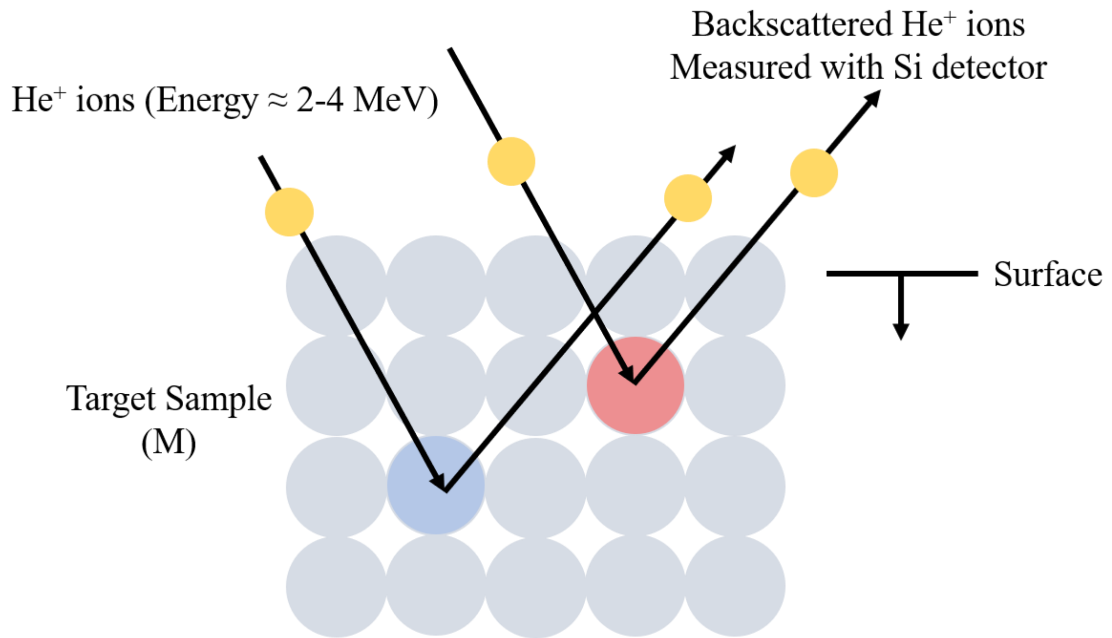

Figure 4-4 Schematic of RBS basic process.

vary based on target material density and incident ion energy [94]. In SiC, 3.5 MeV RBS has a depth resolution of around 1.5 μm and 2.0 MeV RBS has a depth resolution around 0.7 μm.

4.3.2 Channeling RBS (RBS/C)

Outside of elemental analysis and thin film thickness measurements, RBS may also be used to determine the degree of crystallinity in single crystals through channeling RBS, or RBS/C. Channeling occurs when rows of atoms in the target material lattice are aligned with the incident beam. Backscattered yield from a single crystal targets in channeling orientation is greatly diminished compared to yield not in channeling, or in random orientation. This is because the atomic rows in the target along the axis of the incident beam behave as hallways for the ions, limiting the probability of elastic collision. In high quality single crystals, the channeling yield is lower than 5% of the random yield [94]. A plot of 4H-SiC RBS/C spectra comparing a pristine crystal in channeling and random orientation is shown in Figure 4-5.

Defects such as interstitials and dislocations cause blockages and interruptions to atomic rows, limiting channeling effects. In an RBS channeling spectrum, defects can then increase the yield of backscattered ions. Therefore, by comparing the RBS results from a pristine crystal in channeling geometry to a damaged crystal in channeling geometry, lattice disorder can be quantified. The conversion from an RBS/C spectrum to a disorder curve is done using an iterative procedure [95] that eliminates artificial yield due to dechanneling effects from shallower depths. In addition to the RBS/C spectrum of the damaged crystal in a channeling orientation, this procedure also requires (1) the RBS/C spectrum of the pristine crystal in channeling orientation and (2) the RBS/C spectrum of the crystal in a random orientation. The iterative procedure equation used to determine the dechanneling as a function of channels (R(x)) is shown in Equation 4-3.

$$R(x) = P(x) + [1 - P(x)] \times (1 - \exp\left[-\sigma_D \times \sum_{x+1}^{z}[(\frac{n(x+1) - R(x+1)}{1 - R(x+1)})\right]) \qquad \text{Eq (4-3)}$$

Where *P(x)* is the pristine channeling spectrum normalized to the random yield, *n(x)* is the damaged channeling spectrum normalized to the random yield, *x* is the channel value, *z* is

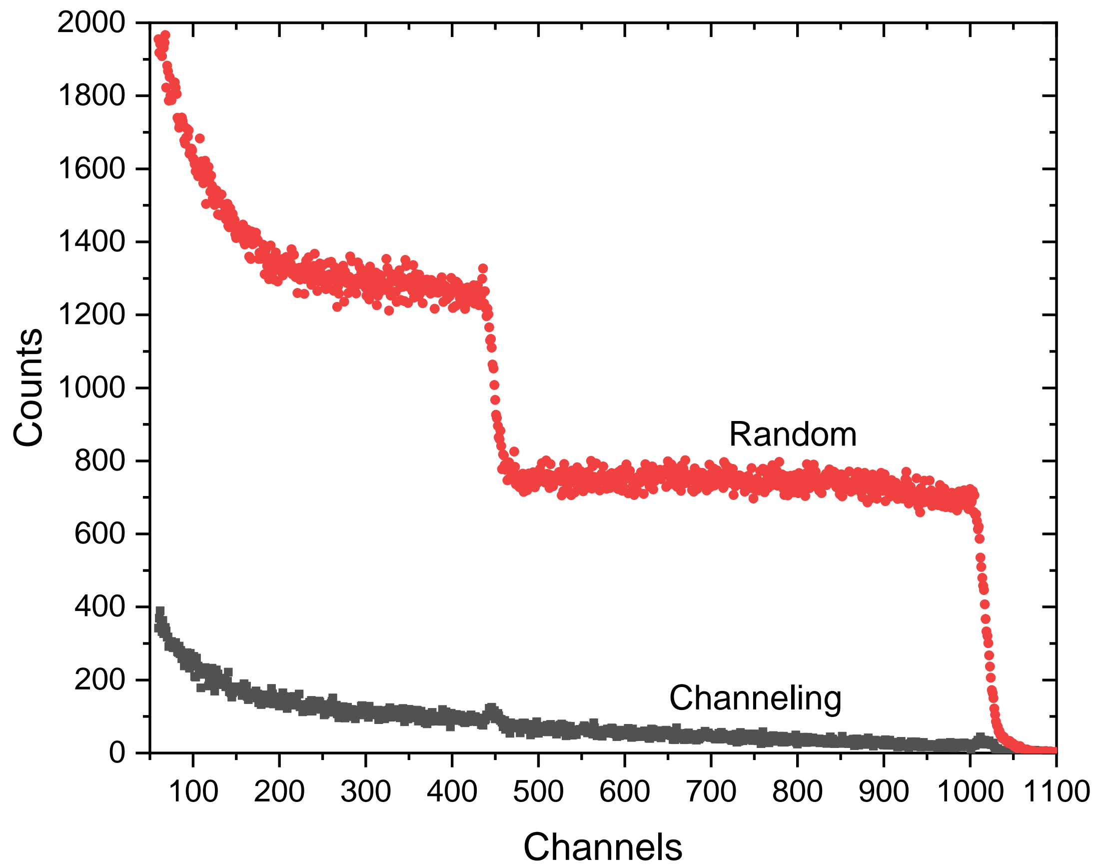

Figure 4-5 RBS spectra for pristine 4H-SiC in random and channeling orientations. Yield from the SiC in channeling orientation is greatly diminished.

the channel value correlating to the sample surface, and σ_D is an adjustable parameter that relates to the dechanneling cross section for the disorder. After finding the $R(x)$ along the damaged range the relative disorder can then calculated using Equation 4-4.

$$Disorder = [n(x) - R(x)]/[1 - R(x)] \quad \text{Eq (4-4)}$$

RBS can also be used to detect trace amounts of dopants and impurities, and RBS/C can be employed to characterize if dopants are on interstitial sites or on lattice sites, as a dopant in a vacancy site will not diminish channeling effects to the same extent as a dopant sitting in an interstitial site, as illustrated in Figure 4-6.

4.4 Sheet Resistivity

Electrical characterization via resistivity measurements is useful to determine the total concentration of defects in a material, as the presence of defects often impedes current flow and therefore increases resistivity. In this work, sheet resistivity measurements via the four point-probe technique are utilized to determine effectiveness of irradiation-induced dopant activation in SiC, as well as, to estimate on implantation and irradiation caused defect complexity as defect clusters and dislocation loops have a greater impact on electrical resistivity compared to point defects.

Sheet resistivity is the measurement of resistivity of a material surface or thin films. In this work, sheet resistivity is determined on 4H-SiC implanted with arsenic atoms near the material surface (< 250 nm). The four-point probe method uses four collinear, equally spaced contacts on a sample surface, as shown in Figure 4-7. The outer contacts supply electric current, while the inner contacts measure voltage as a function of applied current. The four-point probe method is advantageous over other resistivity measurement techniques because wire or contact resistances are not picked up during the measurements.

The general sheet resistivity (σ) equation (4-5) is shown below, where I is the applied source current, V is the voltage measured by voltmeter. Equation 4-5 is valid for sufficiently large samples, where the sample size is much larger than the probe spacing, and thin samples, where the tested material thickness is less than 40% of the probe spacing. Otherwise, geometric correction factors must be included in sheet resistivity calculations.

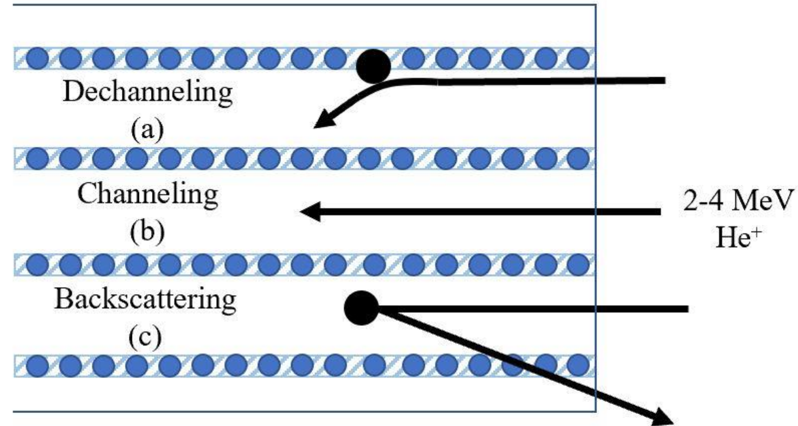

Figure 4-6 Schematic of defect effects on incident RBS beam in a channeling orientated crystal: (a) dechanneling due to a substitutional defect, (b) channeling in a pristine channel, and (c) backscattering due to a displacement or interstitial defect.

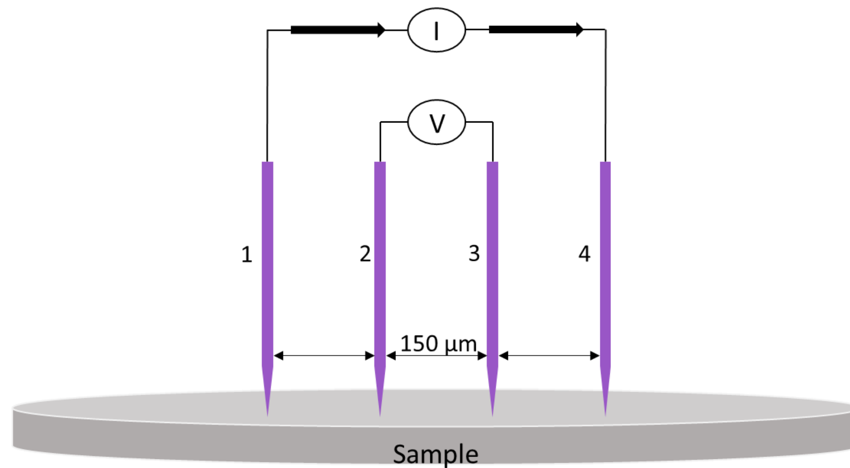

Figure 4-7 Four-point probe sheet resistivity measurement set-up from the MPRF. Four collinear, equally spaced probes are placed on the surface of the sample. Current is applied through contacts 1 and 4, while the voltage is measured with a voltmeter between contacts 2 and 3.

Sheet resistivity is measured in units of ohms per square (Ω/□) to distinguish sheet resistivity values from bulk or other resistivity values.

$$\sigma = (\frac{\pi}{ln2})(\frac{V}{I}) \quad \text{Eq (4-5)}$$

All sheet resistivity measurements were performed at the Micro-Processing Research Facility (MPRF), in the University of Tennessee, Knoxville using a Keithley 2410 high voltage source measure unit (SMU).

CHAPTER FIVE
EFFECTS OF RECOIL SPECTRA AND COUPLED INELASTIC AND ELASTIC ENERGY DISSIPATION ON DEFECT SURVIVAL IN 3C-SIC

A version of this chapter was originally published by Lauren Nuckols *et. al:* L. Nuckols, M.L. Crespillo, Y. Yang, J. Li, E. Zarkadoula, Y. Zhang, W.J. Weber, Materialia 15 (2021) [65].

The spatial coupling of inelastic and ballistic energy deposition was examined by comparing damage accumulation resulting from 5 MeV Si ions, performed and analyzed previously by Xue et al. [63] with damage accumulation from 10 MeV Au ions in 3C-SiC. Irradiations were done at 300 K and disorder was characterized with RBS/C. Stronger coupling between inelastic and elastic processes is associated with decreasing defect survival and greater sensitivity of irradiation-induced defect concentrations to changes in inelastic deposition intensities. It was found that the Si ions exhibited stronger spatial coupling than the Au ions, attributed to the more energetic recoil spectra of the Au ions.

5.1 Experimental Methods

In this work, single crystal 3C-SiC thin films in (001) orientation on a silicon substrate were used. All ion irradiations and ion beam characterization were performed in the IBML. The 5 MeV Si ions and 10 MeV Au ions were chosen because of similar electronic stopping powers and ion depth ranges, but significant differences in nuclear stopping powers and thus damage energy dissipation along the ion trajectories. For both ions, the irradiations were performed 60° off the (001) surface normal to create shallow damage that provided for more accurate analysis of disorder profiles by RBS/C. Ion fluences ranged from 8.7×10^{13} to 1.9×10^{15} cm^{-2} for the 5 MeV Si ions and from 5.0×10^{12} to 1.0×10^{14} cm^{-2} for the 10 MeV Au ions. Ion fluxes were 1.4×10^{12} cm^{-2}s^{-1} for the 5 MeV Si irradiations and 1.9×10^{11} cm^{-2}s^{-1} for the Au irradiations. The maximum temperature increase due to beam

heating was estimated based on power density calculations and was determined to be less than 8°C for both irradiation conditions. The RBS/C measurements were performed in situ along the <001> direction using 3.5 MeV He ions at room temperature under high vacuum.

5.2 SRIM and IM3D Simulations

SRIM 2008 code [57] was used to determine the depth profiles of local numbers of displacements and energy deposition for the 5 MeV Si ion irradiation. However, because the electronic energy loss values for Au ions in SiC are known to be overestimated by SRIM 2008 [96], the IM3D code [97] was used to predict the depth profiles of displacements and energy deposition for the 10 MeV Au ion irradiation. IM3D is a Monte Carlo code used for simulating ion transport and material defect production. It was developed largely for simulating damage accumulation in nanostructures—where only a portion of incident ion energy is deposited into the material, as the size of the elastic collision cascade from a single ion may consistently extend past the small structure. For this study, IM3D utilized new, experimentally derived electronic energy loss values for Au ions in SiC [59], that more accurately predicts the Au implantation profiles. The predicted damage profiles for irradiation conditions in this study along with RBS/C derived disorder as a function of depth for the 5 MeV Si irradiation and 10 MeV Au irradiation are shown in Figure 5-1 and Figure 5-2.

5.3 Recoil Spectra

As described in section 2.2.3, total ionization energy is a measure of the inelastic energy transfer to target electrons by the incident ion and resulting secondary recoils. It is similar to electronic energy loss, which is only the inelastic energy transferred by incident ions and not the following recoils. Damage energy is then a measure of the energy available to produce atomic displacements or lost to phonons (i.e., energy not lost to ionization). Figure 5-3 shows the partitioning of incident ion energy per unit depth to total ionization energy and damage energy under the 10 MeV Au and 5 MeV Si ion irradiations.

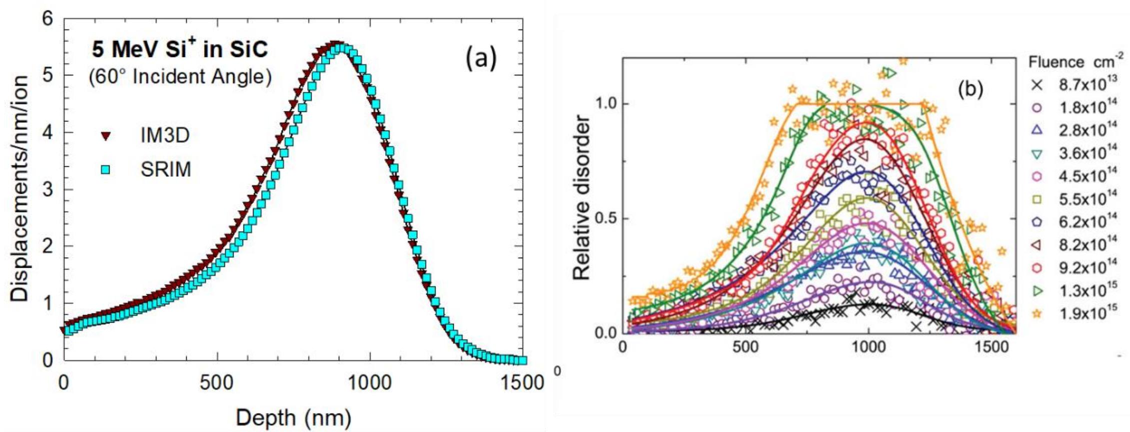

Figure 5-1 (a) SRIM and IM3D predicted depth profiles of local displacement production per ion for 5 MeV Si ions in SiC, and (b) experimentally derived relative disorder derived and reported Xue et al. [63]

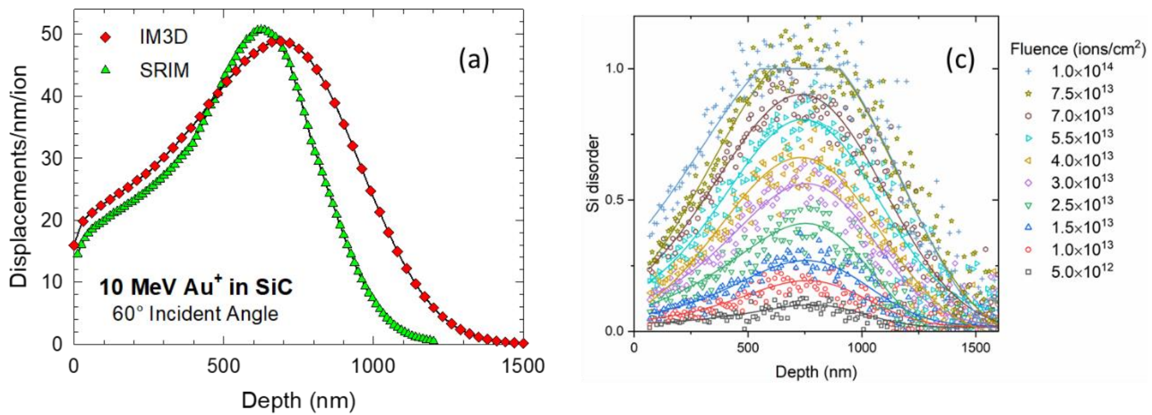

Figure 5-2 (a) Comparison of SRIM and IM3D predicted local displacement production per ion for 10 MeV Au ions in SiC. Differences stem from IM3D simulation employing a new experimentally derived electronic stopping power, and (b) experimentally derived Si disorder.

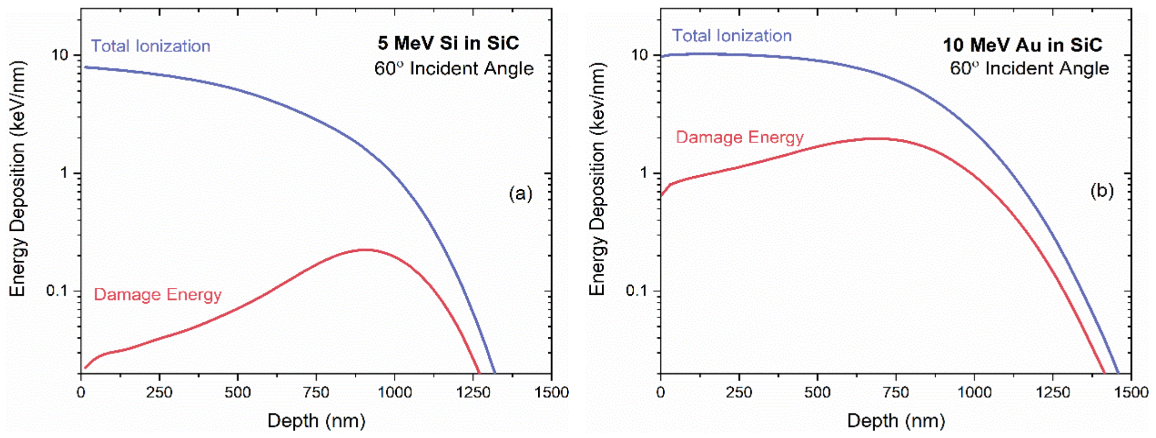

Figure 5-3 The partitioning of incident ion energy per unit depth to total ionization energy and to the damage energy for (a) 5 MeV Si ions and (b) 10 MeV Au ions.

The ionization energy for both the Au and Si irradiations are similar in magnitude. Additionally, under both irradiation conditions, the ionization energy is much larger than the damage energy. The only significant difference between the irradiation energy deposition processes between the two ions is the damage energy; as the damage energy for the 5 MeV Si ions is far less than the 10 MeV Au damage energy, the average values of which are shown in Table 5-1. The lower damage energy deposition from the 5 MeV Si ions results in a softer primary recoil spectrum compared to the 10 MeV Au ions. The differences in damage energy, and therefore ionization to damage energy ratios, provides a measure of the spatial and temporal coupling effects of the energy loss processes on defect survival and disorder accumulation.

Pysrim was used to determine the radial distribution of displacement collisions along the 700 to 800 nm pathlength for both ions, shown in Figure 5-4. This data was determined from full-cascade collision files created by SRIM 2008 code for 10,000 incident ions per irradiation condition. The greater radial distribution of vacancies from the 10 MeV Au ions is due to its relatively harder primary recoil spectrum. Pysrim was also used to determine the primary recoil spectra for the two irradiations based on the same full-cascade collision files. The primary recoil spectra can then be converted to the weighted primary recoil spectra, Figure 5-5, which is the fraction of damage energy produced by all primary recoils with energies less than a given primary recoil energy. Figure 5-5 gives the weighted recoil spectrum in SiC for 5 MeV Si and 10 MeV Au ions and compares it to the weighted recoil spectrum for neutrons produced in the High Flux Isotope Reactor (HFIR) and that expected in a fusion reactor [98]. The weighted primary recoil spectra indicate that the harder primary recoil spectrum from the Au ions is more similar to the recoil spectrum for fast neutrons in SiC, compared to Si self-ions. Self-ions have historically been used to simulate neutron irradiation damage, as self-ions are thought to both simulate PKAs and not introduce chemical entropy into the target material. However, using Si-self ions to achieve high doses requires at least 20 times greater ion fluence than Au ions for equivalent damage depths, leading to high Si interstitial concentrations that are highly mobile in SiC and can significantly affect microstructure evolution. Au interstitials, however, are inert

Table 5-1 SRIM (5 MeV Si) and IM3D (10 MeV Au) predicted total ionization energy, damage energy, and total ionization energy to damage energy depositions ratios at different depths.

	5 MeV Si at 60°			**10 MeV Au at 60°**		
Depth (nm)	**Ionization Energy (keV/nm)**	**Damage Energy (keV/nm)**	**Ratio**	**Ionization Energy (keV/nm)**	**Damage Energy (keV/nm)**	**Ratio**
200	7.1	0.04	177.5	10.2	1.05	9.7
300	6.6	0.04	165.0	10.0	1.22	8.2
400	5.9	0.05	118.0	9.6	1.42	6.8
500	5.1	0.07	72.9	9.0	1.70	5.3
600	4.2	0.10	42.0	8.1	1.89	4.3
700	3.2	0.14	22.9	6.9	1.96	3.5
800	2.4	0.19	12.6	5.3	1.82	2.9
900	1.7	0.22	7.7	3.7	1.43	2.6

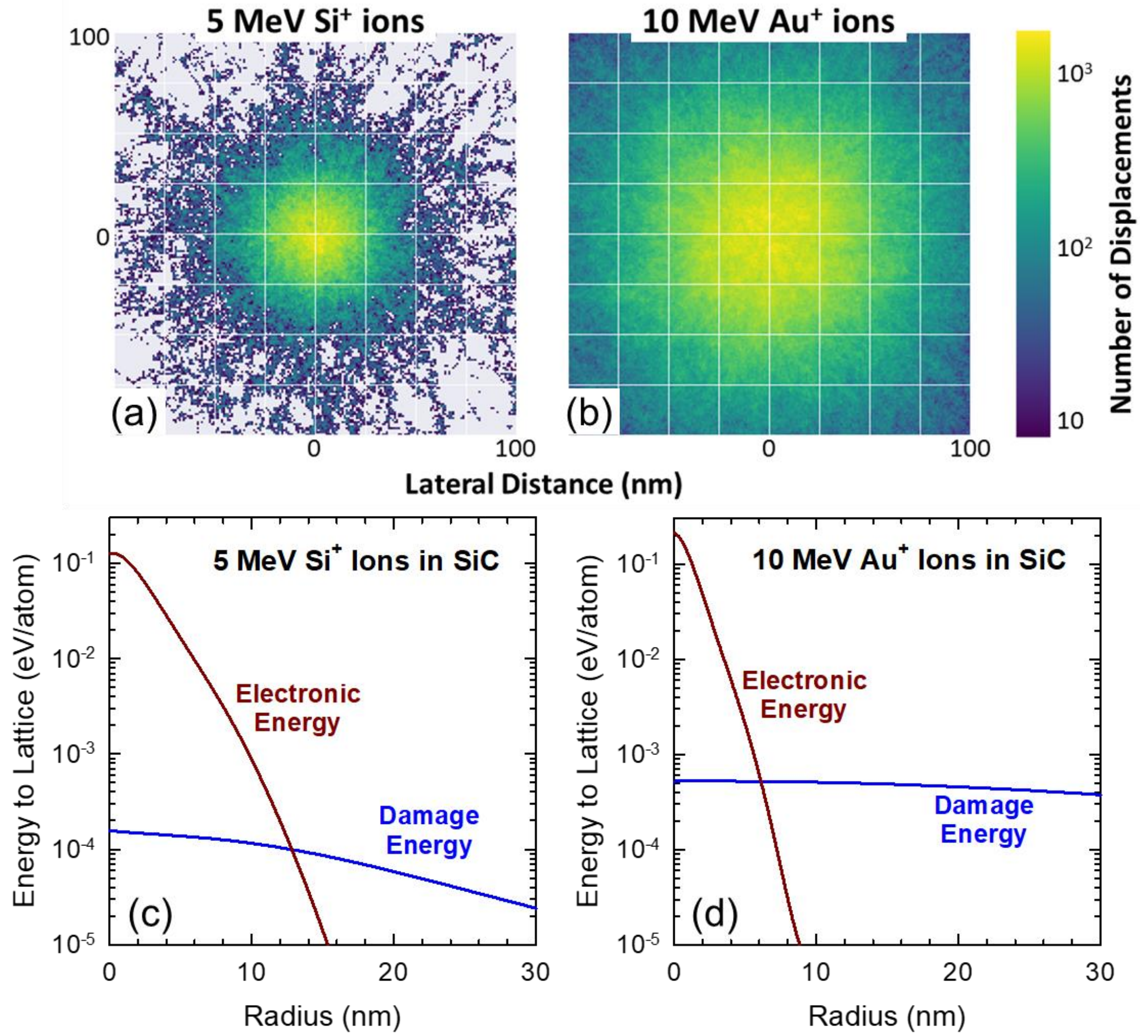

Figure 5-4 Radial distribution of displacement collisions by full-cascade SRIM simulations along a section of pathlength from 700 to 800 nm predicted for (a) 5 MeV Si ions and (b) 10 MeV Au ions. Electronic and damage energy depositions to the atomic lattice over a pathlength of 700 to 800 nm by (c) 5 MeV Si ions and (d) 10 MeV Au ions.

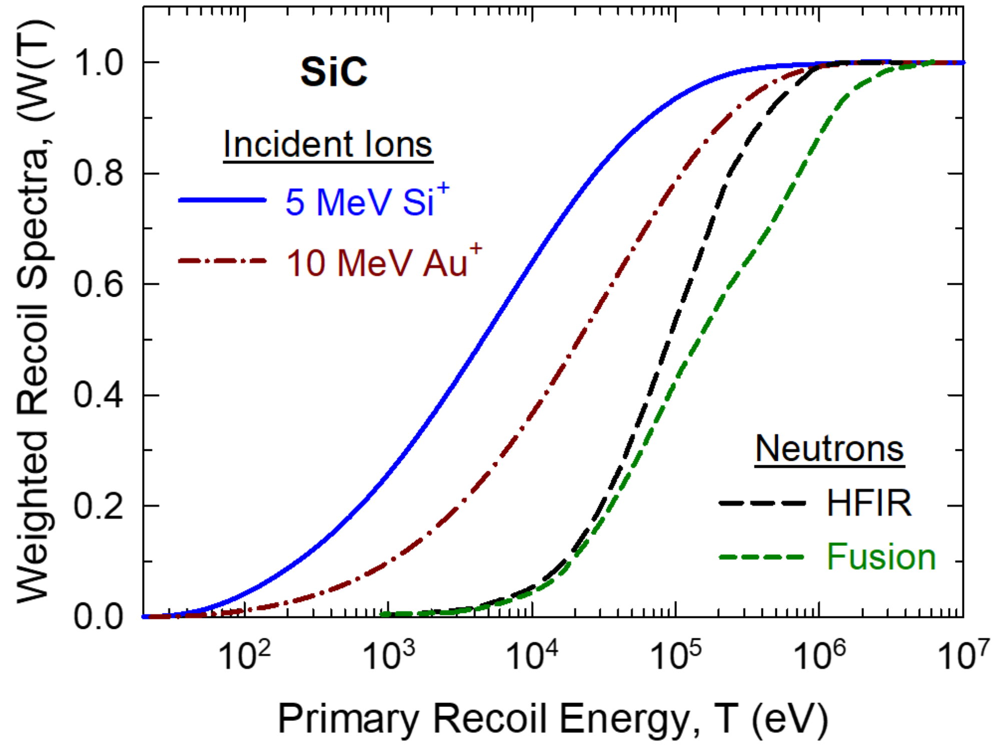

Figure 5-5 Weighted primary recoil spectra for 5 MeV Si ions, 10 MeV Au ions in SiC compared with HFIR neutrons and fusion neutrons calculated by Guo et al. [98].

and immobile in SiC, and therefore better candidates for simulating damage from fast neutrons.

5.4 Disorder Comparison: 5 MeV Si and 10 MeV Au Ion Irradiations

A comparison of the relative disorder accumulation at the damage peak as a function of dose (dpa) for the 5 MeV Si and 10 MeV Au ion irradiations is shown in Figure 5-6. The Au ions are more efficient than the Si ions in disordering SiC, and a fully amorphous state is achieved at a dose of roughly 0.4 dpa under 10 MeV Au irradiation, while full amorphization requires a dose of 0.7 dpa under the 5 MeV Si irradiation. Similar differences in disorder accumulation behavior has been reported in 6H-SiC irradiated at 170 to 190 K by 0.55 MeV Si ions and 2.0 MeV Au ions [99]; however, at 150 K, the disorder accumulation behavior as a function of dose for Si and Au ions is nearly identical [100], indicating that damage accumulation behavior under Si ion irradiation is more sensitive to thermal annealing behavior. Additionally, the dose for full amorphization at the damage peak in 3C-SiC under 10 MeV Au ion irradiation is nearly the same as that for 6H-SiC under 2 MeV Au ion irradiation at 300 K, suggesting that the high density of ionization energy from 10 MeV Au ions at the damage peak likely has minimal effect on defect survival.

The dependencies of relative disorder on local damage dose (dpa) at shallower depths, < 1 μm, are shown in Figure 5-7. The ionization energies from the two irradiation conditions are comparable in magnitude over the first several hundred nanometers of depth. However, the decrease in disordering rate is more pronounced near the surface (400 to 200 nm) under the 5 MeV Si irradiation than under the 10 MeV Au irradiation. Ionization effects are generally more significant near the SiC surface, where ionization energy deposition is maximized and damage energy is minimized for both irradiation conditions. The ratio of ionization to damage energy deposition then decreases from the surface to the damage peak. The total ionization energy, damage energy, and ratio of ionization energy to damage energy at multiple depths is summarized in Table 5-1.

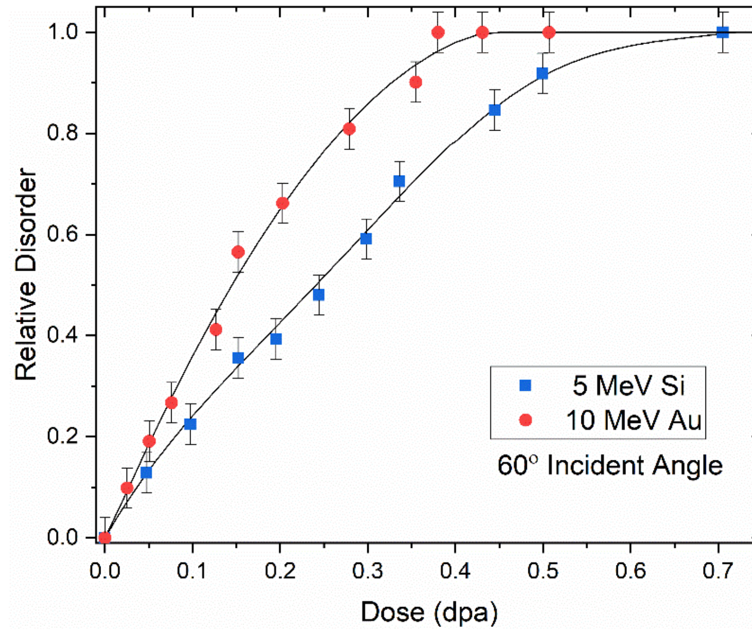

Figure 5-6 Relative disorder on Si sublattice at the damage peak as a function of damage dose in 3C-SiC irradiated with 5 MeV Si ions and 10 MeV Au ions.

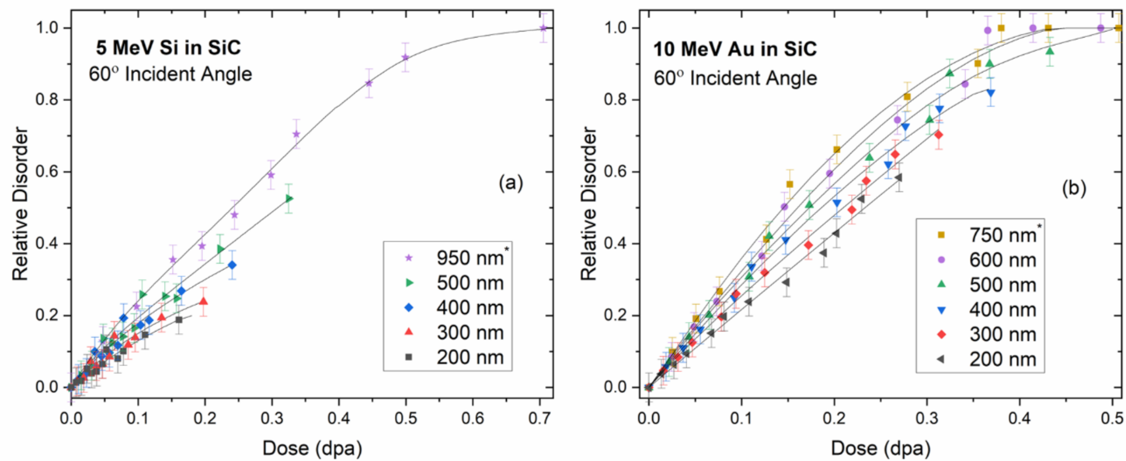

Figure 5-7 Relative disorder fraction on the Si sublattice in 3C-SiC as a function of damage dose (dpa) at different depths: (a) 5 MeV Si ions in SiC (adapted from Ref[63]), and (b) 10 MeV Au ions.

Previous studies at room temperature, where thermal annealing processes are negligible in SiC, demonstrated that the inverse dose for amorphization, $1/D$, is linearly dependent on the ratio of the ionization-induced recovery cross section, σ_i, to the elastic damage cross section, σ_d, and is given by the general expression:

$$1/D = (1/D_o)[1 - (\sigma_i/\sigma_d)\, exp(-E_{i_{rr}}/kT)] \qquad \text{Eq (5-1)}$$

where D_o is the amorphization dose at 0 K, where flux effects are negligible, and E_{irr} is the activation energy for the ionization-induced recovery. Equation 5-1 can be applied to the dose to achieve a specific amorphous state or level of disorder in SiC. At constant temperature (300 K for this study), the exp term is a constant, C, and the inverse dose to achieve a specific disorder is proportional to σ_i/σ_d with a slope C/D_0. The ratio σ_i/σ_d is directly proportional to the ratio of ionization energy to damage energy at a given depth, as summarized in Table 5-1. The doses to achieve disorder levels of 0.15 and 0.20 under 5 MeV Si ions and disorder levels of 0.20 and 0.40 under 10 MeV Au irradiation are determined from the curve fits in Figure 5-7. The inverse doses to achieve these specific levels of disorder are linearly dependent on the ratio of ionization energy to damage energy.

The dose required to achieve 0.2 disorder levels at 0 K (y-axis intercept) is larger for the 5 MeV Si ions than for the 10 MeV Au ions, again confirming that ionization effects are more effective at in-cascade annealing along the ion trajectory for the Si ions. For the Si ions, the results in Figure 5-8 (a) imply that above an ionization energy to damage energy ratio of 390, it may not be possible to achieve disorder levels above 0.15 to 0.20, suggesting disorder saturation levels where ionization-induced annealing processes are in equilibrium with damage production from elastic collision processes. For Au ions, Figure 5-8 (b), there is little difference in the ionization energy to damage energy ratio to suppress disorder levels between 0.20 and 0.40, and a ratio of 20 may suppress achieving disorder levels above 0.50. These results are consistent with the observed full suppression of damage accumulation in 4H-SiC under 21 MeV Si ion irradiation (ionization energy to damage energy ratio exceeding 940) and the predicted full suppression of all damage accumulation

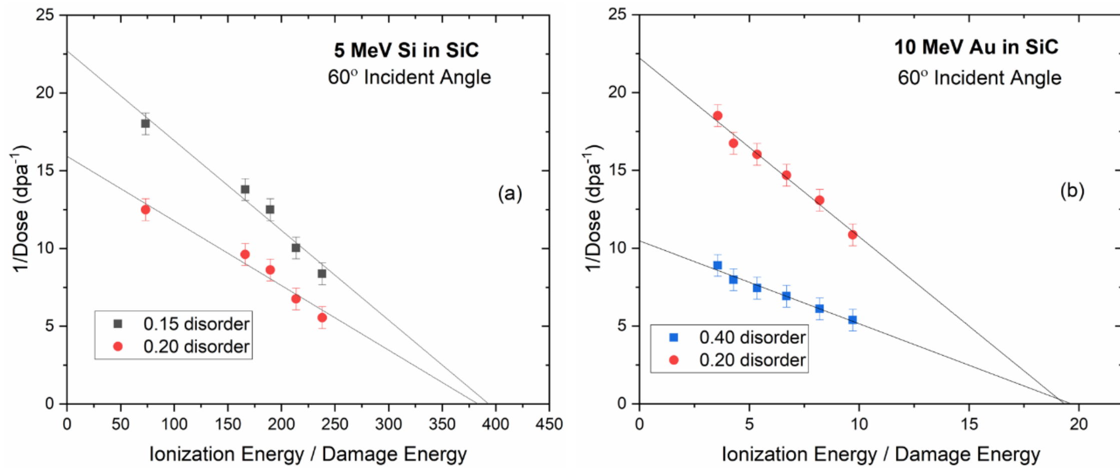

Figure 5-8 Linear dependence of inverse dose to achieve a specific level of disorder on the ratio of ionization energy to damage energy in SiC at 300 K; (a) disorder level of 0.15 and 0.2 under 5 MeV Si irradiation and (b) disorder levels of 0.2 and 0.4 under 10 MeV Au irradiation.

at an ionization to damage energy ratio of 33 in 6H-SiC irradiated with 25 MeV Au ions [34].

Overall, there is greater coupling between inelastic and elastic process for previously tested Si ions, so irradiation-induced defect concentrations from the Si ions are more sensitive to changes in ionization energy compared to the Au ions, where the more energetic recoil spectra lead to weaker spatial coupling between energy deposition processes. Therefore, the resulting damage at similar damage doses (in dpa) is greater from the Au ions compared to the Si ions, and Au ions have a harder recoil spectrum, more comparable to neutrons. Further, SRIM and IM3D based models of radial distributions of collision cascades, recoil spectra, energy partitioning, and displacements as a function of depths were determined. The IM3D code better predicts the Au displacement concentrations as a function of depth due to its utilization of better, experimentally derived, electronic energy loss values for Au in SiC ions.

CHAPTER SIX
COUPLED EFFECTS OF ELECTRONIC AND NUCLEAR ENERGY DEPOSITION ON DAMAGE ACCUMULATION IN ION IRRADIATED SIC

A version of this chapter was originally published by Lauren Nuckols *et. al:* L. Nuckols, M.L. Crespillo, C. Xu, E. Zarkadoula, Y. Zhang, W.J. Weber, Acta Materialia 199 (2020) 96–106. [101]

In this work, coupling between electronic and nuclear energy dissipation in ion-irradiated, SC, n-type, <0001> oriented 4H-SiC was investigated with 10, 15, 18, and 21 MeV Si ions; 20 and 23 MeV Ti ions; and 21 MeV Ni ions at 300 K, and irradiation damage accumulation was characterized using RBS/C. By comparing damage accumulation behavior from incident ions with different atomic numbers and energies, the effects of S_e and electronic to nuclear energy loss ratios (S_e/S_n) can be systematically studied. Table 6-1 summarizes the ion energies used and the SRIM predicted S_e, S_n, and ion ranges. It was found that the damage production rate from S_n decreases with increasing S_e. A dynamic threshold ($S_{e,th}$) in S_e was determined for each ion species, which defines two regions: i) $S_e > S_{e,th}$, where electronic energy dissipation fully suppresses damage production caused by S_n along incident ion paths, and ii) $S_e < S_{e,th}$, where simultaneous damage recovery due to S_e competes with damage production processes. It was determined that the $S_{e,th}$ increases sub linearly with incident ion atomic number.

6.1 Experimental Methods

Single crystal, n-type <0001>- orientated 4H-SiC wafers were used in this work. All samples were cut to areas less than 12×12 mm^2 with a diamond scribe to avoid lattice strain. Samples were cut from the same bulk wafer and mounted on the target holder with double-side carbon tape for the room temperature irradiations and RBS/C characterization.

The SRIM code [57] was used to calculate depth profiles of displaced atoms and

Table 6-1 SRIM predicted surface values of S_e, S_n, and ion range values for various ions in 4H-SiC.

Ion	**Irradiation Energy (MeV)**	**S_e (keV/nm)**	**S_n (keV/nm)**	**S_e/S_n**	**Ion Range (nm)**
Si	10	4.71	0.020	244	3138
	15	4.97	0.015	360	4161
	18	5.03	0.012	424	4758
	21	5.04	0.010	483	5350
Ti	20	6.96	0.040	175	4444
	23	7.23	0.036	202	4867
Ni	21	8.12	0.069	118	5426

electronic and nuclear energy loss for each ion type and energy, as shown in Figure 6-1 for some selected ions. Pysrim [91] was then used to determine the radial details of full-cascade TRIM simulation events over the projected ion range from 20 to 1500 nm.

All the irradiations and ion beam characterizations were performed at the IBML. Seven different irradiation conditions were performed at room temperature: 10, 15, 18, and 21 MeV Si, 20 and 23 MeV Ti, and 21 MeV Ni. Silicon ions were selected for study based in part on previous work where the ionization-induced thermal spike suppressed damage production for 21 MeV Si ion to a depth of ~1000 nm, while damage suppression for 4.5 MeV C, 6.5 MeV O, and 21 MeV Ni was only observed over shallow depths [34]. Additionally, high energy self-ions, such as Si are often preferred over C self-ions for high dose irradiation studies of SiC and SiC-based composites. The heavier, more energetic Si incident ions will have larger S_n values and, consequently, more nuclear scattering and larger recoil cascade [102]. It is therefore critical to understand the effect of electronic energy loss and electronic to nuclear energy loss ratios for Si ions on defect production through a systematic investigation. The Si irradiations were performed initially with lower energy (10 MeV) incident ions, and in subsequent irradiations, the incident ion energy and corresponding electronic energy loss was increased until total damage suppression was evident, which is clearly observed in the 18 and 21 MeV Si irradiations.

The irradiations were all carried out at 7° off the surface normal direction to prevent any undesired channeling effects in the single crystals. The charge states of the ions ranged from 3+ to 7+ depending on the ion and energy compatibility with the accelerator terminal voltage. While the charge states from the tested incident ions may have a limited effect on ion-target interactions, the charge equilibrium for the incident ions takes place within a very short distance and timeframe after entering the solid, so effects are limited to the very surface of the SiC [103]. During each irradiation, the ion beam was defocused and slightly wobbled to ensure a uniform damage distribution over the irradiated area. The flux was kept below 3.4×10^{12} $cm^{-2}s^{-1}$ to minimize beam heating. The maximum changes in temperature were estimated based on power density calculations using the energy deposited via ionization, irradiation flux, SiC heat capacity at room temperature, and the SiC sample

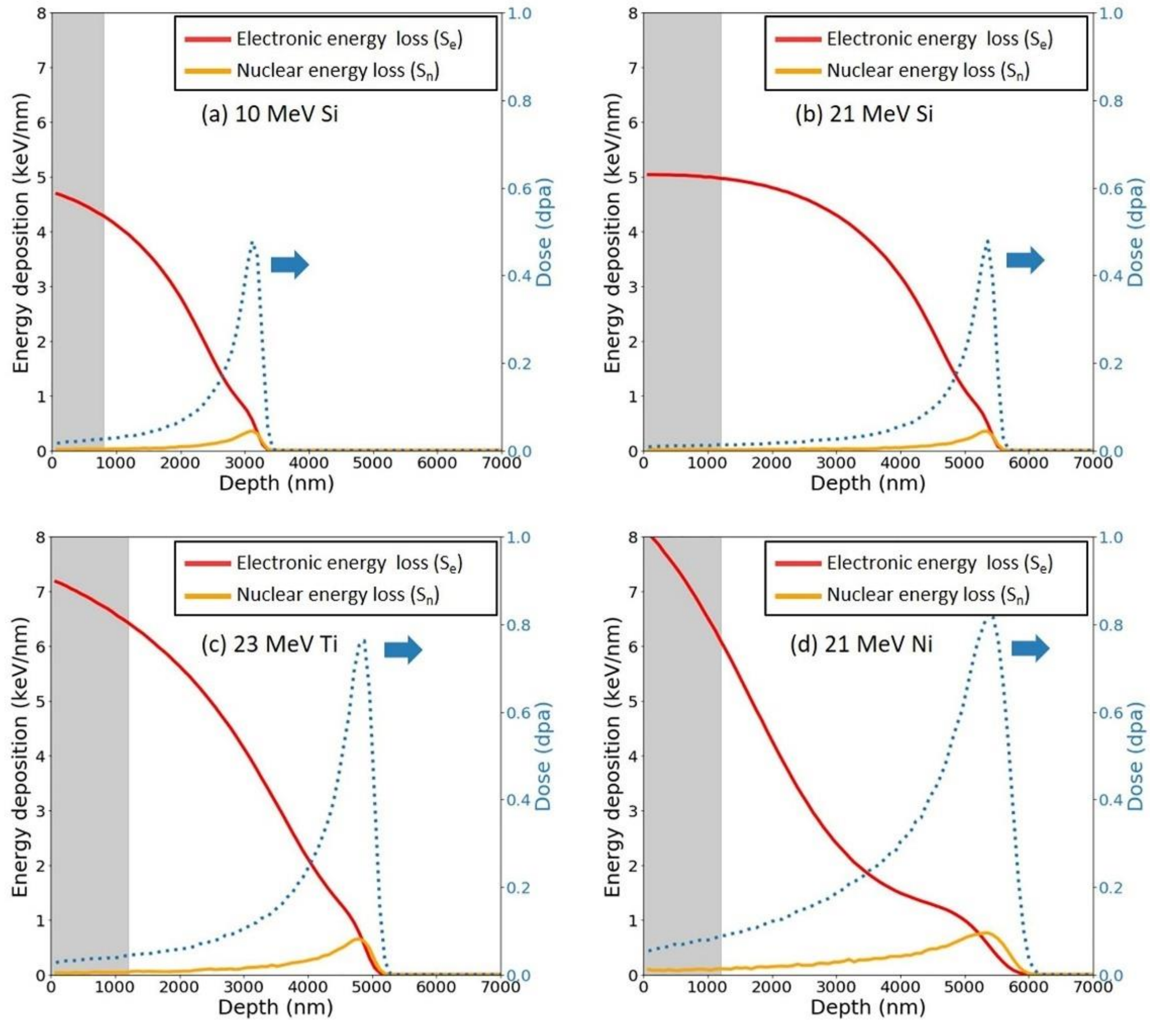

Figure 6-1 SRIM predicted electronic (S_e) and nuclear (S_n) energy loss along with predicted damage doses (dpa) for a fluence of 1×10^{15} cm^{-2} for (a) 10 MeV Si, (b) 21 MeV Si, (c) 23 MeV Ti, and (d) 21 MeV Ni irradiations. Shaded region represents RBS/C characterization region.

size, while any heat draining through the molybdenum sample holder was neglected. The higher estimated temperature increase was 60°C during the 15 MeV Si irradiation. The 10 MeV Si, 18 MeV Si, and 20 MeV Ti irradiation induced an estimated 30 to 45°C temperature increase, and the remaining irradiations induced an estimated temperature increase of less than 10°C. These temperatures shifts under the room temperature irradiations are sufficient to induce some decrease in disorder accumulation rates [104,105], and are accounted for in the following sections. The position and homogeneity of the beam was confirmed with a CCD camera using ion beam induced luminescence from a silica scintillator.

The ion energies and species were selected to represent a range of S_e values and S_e/S_n ratios that would induce damage annealing [63,78], as well as to provide a better understanding of the coupled and competing effects between electronic and nuclear energy dissipation processes. Ion fluences ranged from 5×10^{14} cm^{-2} to 2×10^{16} cm^{-2}. Fluences were selected based on damage dose dpa calculations to ensure that damage production from nuclear energy loss, if present, would be detectable with RBS/C characterization, as well as to ensure that deeper damage would not affect the RBS/C analysis performed on the shallower depths of interest. A table of the irradiating ion species with the tested fluences and fluxes are shown in Table 6-2.

Damage accumulation analysis was performed with RBS/C under high vacuum. RBS/C data was collected in-situ within the IBML using either a 2 or 3.5 MeV He ion beam. Characterization on the 10, 15, and 18 MeV Si irradiated samples was carried out using 2 MeV He RBS/C, and characterization of the 21 MeV Si, 20 and 23 MeV Ti, and 21 MeV Ni irradiated samples was performed with 3.5 MeV He RBS/C.

Disorder on the Si-sublattice, d_f, profiles were calculated with the following expression:

$$d_f = (X_i - X_p)/(X_r - X_p) \quad \text{Eq 6-1}$$

Where X_i, X_p, and X_r are the backscattered yield from the irradiated sample along the <0001> channeling direction, the backscattered yields from a pristine sample along the <0001> channeling direction, and the backscattered yields for a random orientation,

Table 6-2 Tested ion species, fluences, and fluxes.

Ion	Irradiation Energy (MeV)	Fluences ($\times 10^{15}$ cm^{-2})	Flux (cm^{-2}s^{-1})
Si	10	2, 5, 10, 15	3.01×10^{12}
	15	2, 5, 10, 15, 20	3.33×10^{12}
	18	1, 2	1.16×10^{12}
	21	0.5, 1	8.93×10^{10}
Ti	20	1, 2, 3	5.79×10^{11}
	23	0.5, 1, 2	1.49×10^{11}
Ni	21	0.5, 1	1.49×10^{11}

respectively. Damage peaks from all the irradiation performed were deeper than the maximum depth visible to 2 or 3.5 MeV He RBS/C beam, so the iterative procedure normally employed to eliminate dechanneling effects could not be used [95]. Because of this, disorder values at deep depth for all the irradiations are likely slightly overestimated. However, comparisons between disorder profiles from irradiations on the same wafer are only limited by RBS/C experimental error.

6.2 Lower Energy Si Irradiation Disordering

The disordering on SC 4H-SiC, determined with RBS/C, after 10, 15, and 18 MeV Si irradiations can be found in Figure 6-2. The general trend from these irradiations shows that at the same fluence, Si-lattice disorder decreases with increasing ion energy, confirming that S_e competes with disordering processes from $S_{n,}$ as the S_e values for these irradiations increase with overall ion energy.

Damage accumulation from the 10 MeV irradiation, Figure 6-2 (a), demonstrates that overall disorder has a positive correlation with fluence. However, this relationship between dose and lattice disorder breaks down in 15 MeV Si irradiation, shown in Figure 6-2 (b). During this irradiation, accumulated damage saturates at fluences greater than 5×10^{15} cm^{-2}, indicating that an equilibrium between damage production by ballistic collisions and annealing effects induced by ionization. Damage equilibriums that have little dependence on fluence were also observed during the 20 MeV Ti, 21 MeV Ni, and 21 MeV Si irradiations. A comparison of the disorder accumulation on the Si lattice 400 nm in depth as a function of fluence for the 10 and 15 MeV Si irradiation, along with 5 MeV Si data from previous studies on 3C-SiC [63], are shown in Figure 6-3 (b). As Si ion irradiation energy increases, the disorder devolves from a linear-type relationship to disorder saturation.

The 18 MeV Si disorder as a function of depth is shown in Figure 6-2 (c). There is negligible to no detectable Si-lattice disorder from the surface to 160 nm depth. This depth is considered the critical depth (D^*) crossover, as at deeper depths damage starts to linearly accumulate. D^* was determined by the zero-disorder intercept of a linear fit to the 2×10^{15}

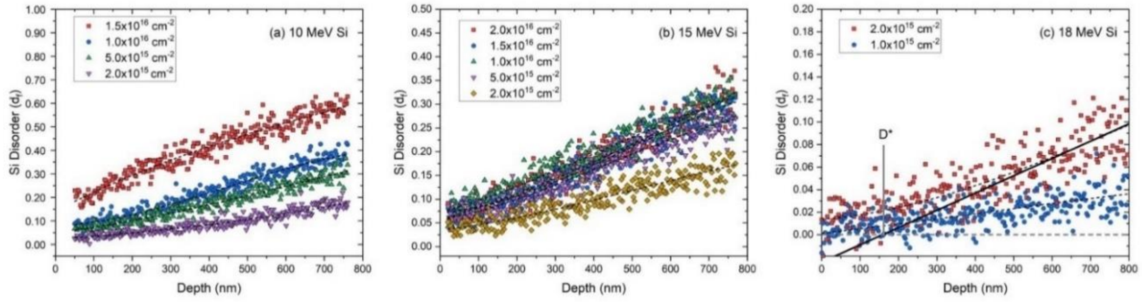

Figure 6-2 Disorder on Si-sublattices as a function of depths for (a) 10 MeV Si, (b) 15 MeV Si, and (c) 18 MeV Si irradiations.

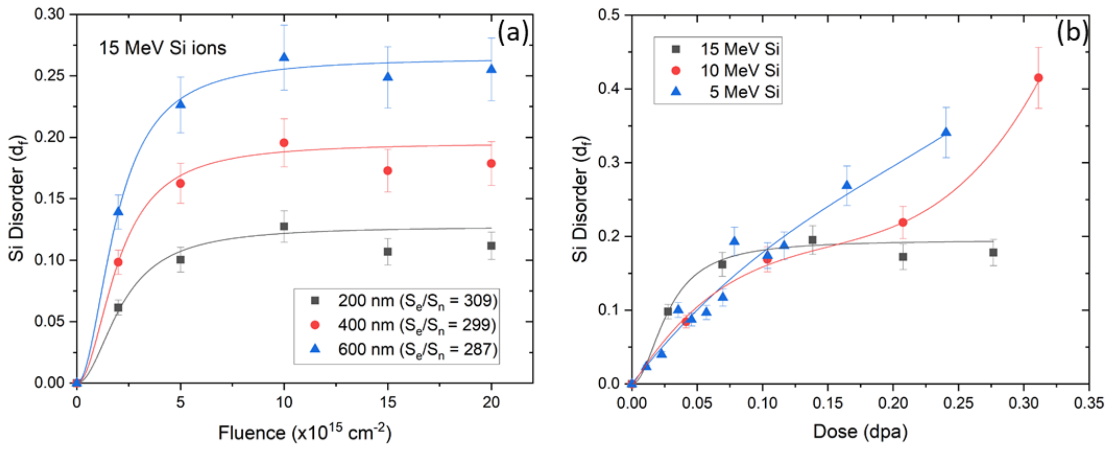

Figure 6-3 Si-lattice disorder as a function of either fluence (a) or dose (b). (a) 15 MeV Si irradiation shows constant disorder with fluences ranging from 5 to 20 × 10^{15} cm^{-2}. (b) Comparison of disorder accumulation for 5, 10, and 15 MeV Si irradiations.

cm^{-2} profile at depths greater than 550 nm. At D*, the Se is 5.02 keV/nm, the Se/Sn ratio is 407, and the average ion energy is 17.9 MeV.

6.3 Higher Energy Si, Ti, and Ni Disordering

The disordering on SC 4H-SiC after 21 MeV Si, 20 and 23 MeV Ti, and 21 MeV Ni irradiations can be found in Figure 6-4. The number of potential collision cascade sources in a material increases with fluence, generally increasing the total amount of disorder in a target material. However, these higher energy irradiation conditions, and the 15 MeV Si irradiation, all exhibit disorder accumulation with limited or no dependence on fluence. During these irradiations, competing disordering and annealing processes are in equilibrium with increasing ion fluence. Annealing processes from incident-ion S_e in ceramics can be modeled as a cylindrical thermal spike; the radial size and intensity of which increases with increasing S_e. Under the tested conditions, annealing is largely limited to within the radial dimensions of the thermal spike where there is sufficient energy to facilitate point defect mobility. For pre-existing defects, ionization-induced annealing takes place in SiC at values greater than 1.4 keV/nm [78], and for ionization-induced annealing of defects produced along the ion trajectory, 1.0 keV/nm [63]. Therefore, equilibrium conditions between annealing and disordering processes should occur when most displacements are within the thermal spike.

Disorder saturation may only occur over a range of fluences: at low fluences, annealing is the dominant process, and at higher fluences, there is an increasing probability of energetic recoils and collision cascades that extend radially beyond the influence of the thermal spike along the ion trajectory. Further, at sufficiently high doses, interstitial defects from deeper regions within the target may migrate towards the surface (i.e., down the defect concentration gradient), at room temperature. The Pysrim predicted radial distributions of displacements are compared to the radial temperature profiles from the inelastic thermal spike model for 18 MeV Si and 20 MeV Ti, as shown in Figure 6-5.

As with the 18 MeV Si irradiation, total damage suppression was detected after the 21 MeV Si irradiation. The D* determined after the 21 MeV Si irradiation is 487 nm,

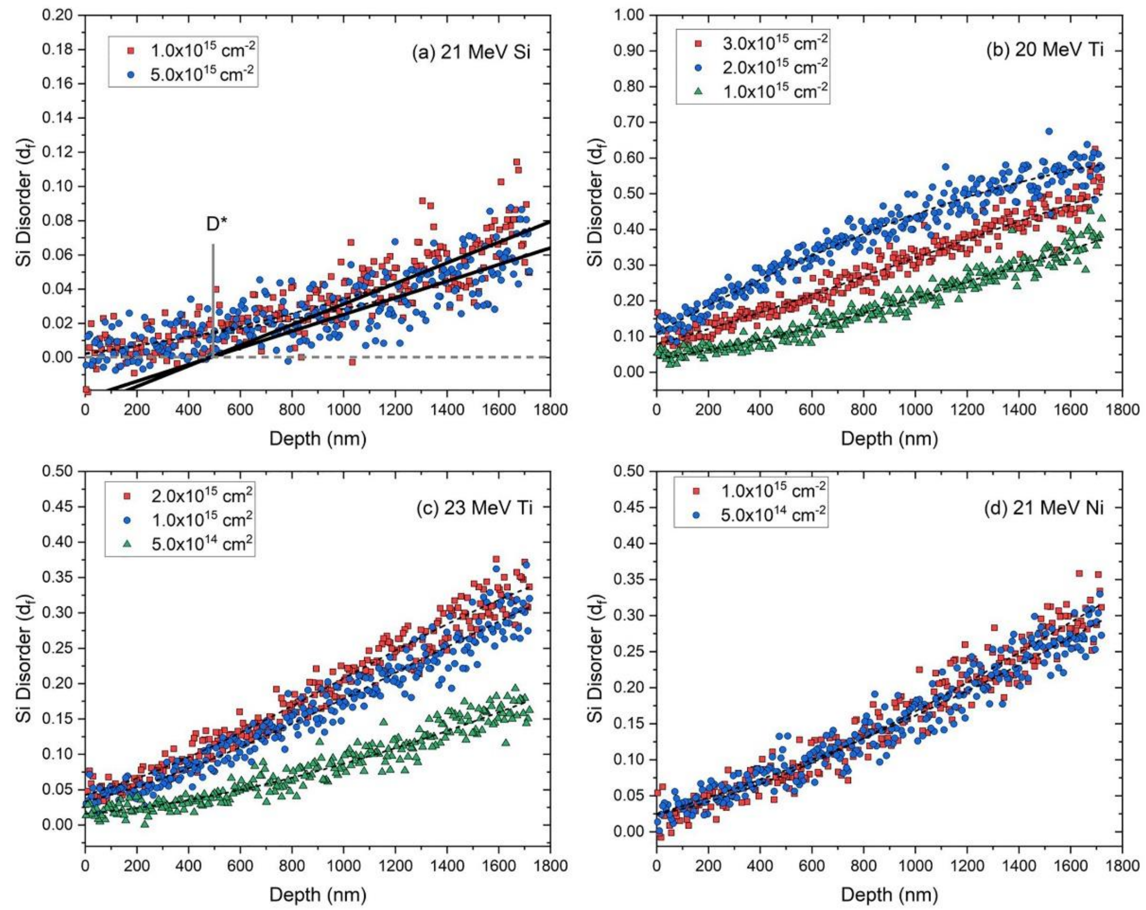

Figure 6-4 Si-sublattice disorder as a function of depth for (a) 21 MeV Si, (b) 20 MeV Ti, (c) 23 MeV Ti, and (d) 21 MeV Ni irradiations.

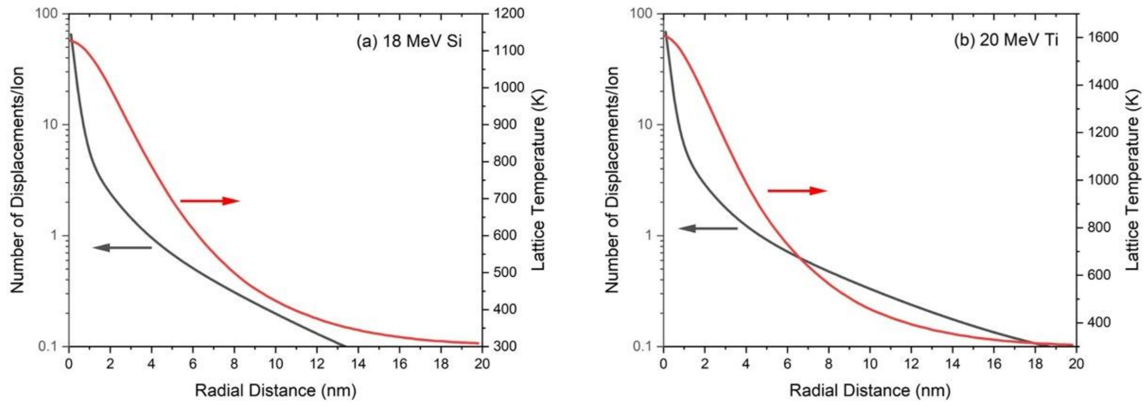

Figure 6-5 Radial distribution of displacements and radial temperature profiles from inelastic thermal spike model for (a) 18 MeV Si and (b) 20 MeV Ti.

corresponding to a S_e value of 5.03 keV/nm, an Se/Sn ratio of 439, and an average ion energy value of 19.2 MeV. There is a slight discrepancy in Se,th and average ion energy values at D* between the 18 and 21 MeV Si. Additionally, previous work using 21 MeV Si irradiation on 4H-SiC at 1×10^{15} cm^{-2} and flux of 1.7×10^{11} $cm^{-2}s^{-1}$, resulted in no measurable disorder to a depth of 1000 nm [34], while this study measured ~2-3% disorder at 1000 nm. Variations may be due, in part, to the migration of interstitial defects, which are mobile at room temperature, towards the surface. Stochastic defect generation differences between identical irradiation conditions should also be considered. Recoil collision cascade size and direction along the incident ion trajectories are calculated using the Monte Carlo Binary collision approximation within SRIM, which results in stochastic variation for a limited number of ions (10,000 in the present study). Because of this, D* and $S_{e,th}$ have a degree of uncertainty.

6.4 Electronic energy loss and disordering processes

RBS/C measured disorder as a function of S_e is summarized in Figure 6-6 (a) for the higher energy irradiations. At comparable S_e values for the 20 MeV Ti, 23 MeV Ti, and 21 MeV Ni irradiations the resulting disorder from the Ti ion irradiations are greater than the Ni irradiation, despite the fact that the S_e/S_n ratios for the Ti ions are higher than Ni ions. This could be a kinematic effect due to mass ratios or a more efficient role of ionization-induced annealing of prior-produced defects by the Ni ions which have larger S_e values.

The corresponding slopes of the Si disorder curves versus S_e plots are shown in Figure 6-6 (b). There is less than 10% difference in slope values between irradiations with the same ions, implying that there is an intrinsic relationship between incident ion Z values and disordering rates as a function of S_e. There is a clear linear correlation between incident ion atomic number and how sensitive the resulting disorder is to changes in S_e. So, damage accumulation in SiC from lighter incident ions is more sensitive to changes in S_e values than that of heavier incident ions. This may be due to the relative size of the recoil collision cascades along the ion trajectory compared to the ionization-induced thermal spike.

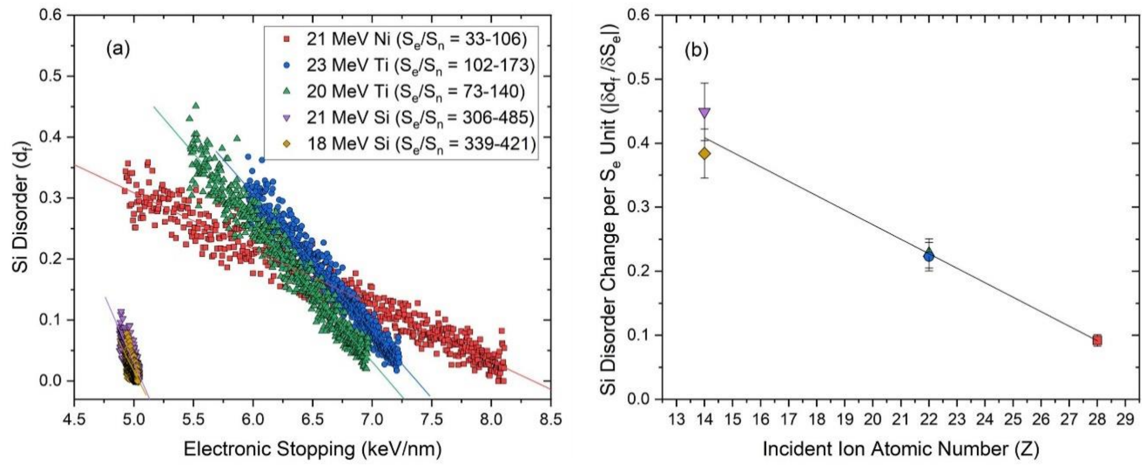

Figure 6-6 (a) Si disorder as a function of S_e (data from 1×10^{15} cm^{-2} fluence irradiations). (b) Rate of disorder as a function of incident ion Z values (slopes from (a)).

6.5 S_e Thresholds

$S_{e,th}$ for the tested ions is shown in Figure 6-7, while Table 6-3 includes the $S_{e,th}$, E_{th}, and dose at the threshold for 1×10^{15} cm^{-2} fluences. Data points for Si incident ions was found via the method described in section 6.2. For the remaining tested ion species, Ni and Ti, $S_{e,th}$ was estimated by extrapolating the linear dependence of Si disorder on electronic energy loss to zero disorder. Zhang et al. [34] also performed irradiations with 21 MeV Ni on 4H-SiC at a fluence of 1×10^{15} cm^{-2}. In that study, the RBS/C spectrum indicated damage production was fully suppressed from the surface to some depth. As an addition to this study, the RBS/C spectrum has been analyzed and yields an $S_{e,th}$ value of 7.12 keV/nm, as shown in Figure 6-7.

The $S_{e,th}$ for total damage suppression increases with incident ion atomic number (Z). Incident ion Z and S_n values increase with decreasing ion energy. The number and radial extend of defects produced along the incident ion trajectory due to recoils produced by S_n increases with incident ion Z values. Because of this, an increase in inelastic thermal spike intensity and radial size (i.e., higher S_e) should be required to suppress or decrease damage accumulation. For incident ion Z values greater than Ni, higher energies are required to achieve the necessary high S_e values to suppress damage production. Such high energies are beyond IBML accelerator capabilities but could be investigated at other facilities. Electronic energy loss thresholds for any damage annealing of pre-existing defects at room temperature is 1.4 keV/nm [78]. This value may correlate as the $S_{e,th}$ value for complete damage suppression from sufficiently low-Z incident ions, such as lithium or beryllium.

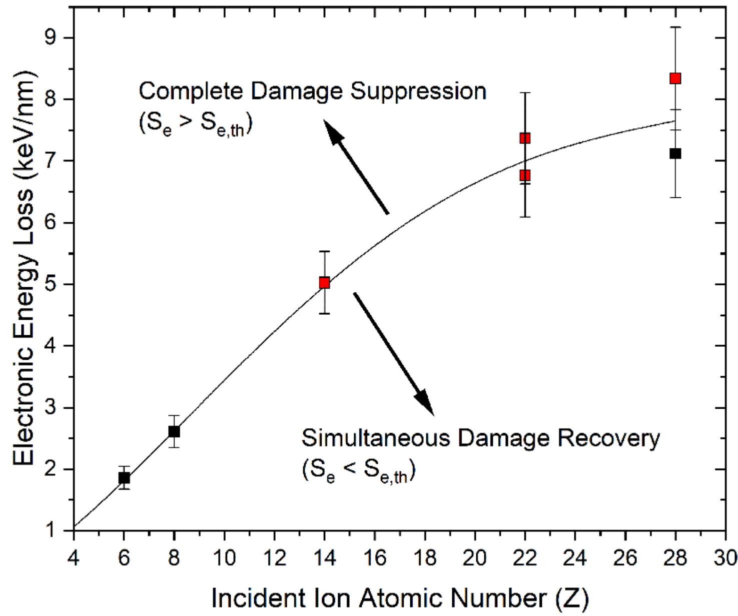

Figure 6-7 Electronic energy loss thresholds above which full damage suppression occurs.

Table 6-3 $S_{e,th}$, E_{th}, and dose (dpa) for a fluence of 1×10^{15} cm^{-2} at total damage suppression threshold values for all irradiations. (*) represents data obtained by ref [34].

Ion	Irradiation Energy (MeV)	Threshold S_e (keV/nm)	Energy at Threshold (MeV)	Dose at Threshold (dpa)
C	4.5*	1.86	3.25	0.005
O	6.5*	2.61	5.50	0.006
Si	18	5.02	17.9	0.010
	21	5.03	19.2	0.010
Ti	20	7.14	22.2	0.028
	23	7.38	25.5	0.026
Ni	21	8.34	22.3	0.048
	21*	7.12	15.8	0.076

CHAPTER SEVEN
ION INDUCED IONIZATION EFFECTS ON DOPANT ACTIVATION IN 4H-SIC

The electrical properties of SiC such as its wide bandgap, very high dielectric field strength and electrical drift velocity comparable to silicon, paired with its chemical and mechanical inertness at elevated temperatures make it an attractive material as the base for semiconductor devices for harsh environment, high power, and high frequency applications. In many of the current and potential applications of SiC-based devices, degradation due to irradiation from cosmic sources, fission or fusion neutrons, or fission fragments is a concern. While irradiation effects on SiC microstructure and defect behavior is well studied, the impact of irradiation, specifically ion-induced ionization effects, on electrical properties and dopant behavior is not as well understood. In this work, ion-induced ionization effects on SiC dopant and annealing behavior is investigated using 21 MeV Ni ion on 4H-SiC doped with As ions at 250°C and 500°C implantation temperatures. Arsenic activation and diffusion, along with implantation and implantation + irradiation induced disorder is characterized using RBS/C and sheet resistivity measurements. Arsenic distribution and activation are not altered by the Ni irradiation. However, disorder from the 250°C implantation temperature is reduced along the entire damage region due to ionization energy deposition, while disorder induced by the 500°C implantation is largely unaffected, attributed to the higher concentration of more thermally stable defects surviving the higher temperature implantation. Comprehensive understanding of ionization effects on annealing, electronic, and dopant properties in SiC is necessary to design function electrical devices exposed to harsh radiation environments.

7.1 Methods

Single Crystal, n-type. <0001>-orientated 4H-SiC was used in this study. Two samples were cut to a 7×12 mm^2 rectangle. Samples were mounted with silver paste on the target holder for implantations and irradiations. They were then moved to a separate holder for

RBS/C analysis. All implantations, irradiations, and ion beam analysis were performed at the IBML. Donor, n-type, 1 MeV As ions were chosen as the dopant species because the As distribution and changes in distribution in SiC can easily be detected via RBS/C. Additionally, As dopant thermal activation and effects in SiC has be extensively reported on previously [106]. Arsenic implantations were performed at incident angle of 60° so the distribution of As ions (25 to 420 nm) are sufficiently close to the SiC surface to alter surface resistivity and so any irradiation induced migration and/or electrical activation would be visible with RBS/C. A fluence of 2×10^{16} cm^{-2} was used for all implantations, well below the solubility limit of As in SiC (5×10^{16} cm^{-3} [107]) to prevent dopant species precipitation. The fluxes for all the implantations were 3.13×10^{12} cm^{-2}s^{-1}. Consistent flux is necessary particularly at temperatures near the critical temperature for amorphization [70]; studies using 100 keV Si implantation on SiC at 120°C found that implantation flux can have a significant impact on resulting damage. As flux increases there are more instances of overlapping collision cascades leading to the formation of complex defects able to withstand in-cascade annealing effects [108]. The implantations were performed at two temperatures 250 and 500°C to analyze the effects of initial disorder state on irradiation induced annealing.

Multiple implantations were performed sequentially at each elevated implantation temperature, so different implantation areas spent varying amounts of time at either 250 or 500°C, as summarized in Table 7-1. 21 MeV Ni ions were chosen as the irradiation species due to the large deposition of ionization energy near the surface of the target material. Based on the thermal spike model, the predicted lattice temperature in SiC irradiated with 21 MeV Ni ions exceeds 1427°C at a depth of 650 nm in 0.1 ps [34], near the typical post-implantation annealing temperatures for doped-SiC. Additionally, previous studies of similar energy Ni ions have shown significant annealing effects on pre-existing damage in SiC. 21 MeV Ni ions almost completely anneal SiC that was pre-damaged to a fractional disorder of 0.72 [78]. 21 MeV irradiation fluences ranged from 5.0×10^{14} cm^{-2} to 1.5×10^{15} cm^{-2}. A summary of the implantation and irradiation conditions for different spots on 4H-SiC wafer is provided in Table 7-1.

Table 7-1 Implantation and irradiation conditions for different area on 4H-SiC samples.

Spot	Implantation temperature (°C)	1 MeV As Implantation fluence (cm^{-2})	21 MeV Ni Irradiation Fluence (cm^{-2})	Time spent at implantation temperature (approximate)
Pristine	N/A	N/A	N/A	N/A
Spot A	500	2×10^{16}	N/A	2hr:50min
Spot B	500	2×10^{16}	5×10^{14}	4hr:40min
Spot C	500	2×10^{16}	1×10^{15}	1hr:00min
Spot D	250	2×10^{16}	N/A	1hr:00min
Spot E	250	2×10^{16}	5×10^{14}	4hr:40min
Spot F	250	2×10^{16}	1×10^{15}	2hr:50min
Spot G	250	2×10^{16}	1.5×10^{15}	1hr:00min

The SRIM code [57] was used to predict the energy partitioning deposited from the 21 MeV Ni ions, as shown in Figure 7-1. Energy partitioning was plotted using the Pysrim python program [91]. Characterization was done with 2 MeV RBS/C at room temperature under high vacuum, and sheet resistivity measurements were taken via the four-point probe method utilizing a Keithley 2419 current source-measure unit in the MPRF.

7.2 Arsenic Distribution and Activation

Figure 7-2 shows the RBS/C results comparing spectra from pristine SiC, doped SiC, and doped + irradiated SiC at the two tested implantation temperatures. The peak in channels 1300 to 1650 (equivalent to depths of 450 to 0 nm) correspond to the arsenic content in SiC. Arsenic yield is lower in all the channeling spectra compared to the yield in SiC in a random orientation. This relates to the sites occupied by the dopant species. The presence of atoms sitting on lattice sites or, in the case of extrinsic elements, substitutional sites will be diminished in RBS/C spectra taken while the sample is in a channeling orientation, see section 4.3.2 for more details. Therefore, the drop in RBS/C counts associated with arsenic is due to a portion of the arsenic atoms sitting on substitutional sites, which is correlated to dopant activation. Partial activation after implantation at elevated temperatures was anticipated and has been reported with previously with aluminum doping in SiC under similar conditions [45].

Plots comparing the arsenic distribution between the irradiation spots in random and channeling orientation for the implantations performed at both temperatures is shown in Figure 7-3. Both ionization from 21 MeV Ni ions and thermal annealing implantation temperature did not alter the arsenic distribution in SiC under the two implantation conditions. The diffusion coefficient of arsenic in SiC is very low, on the order of 10^{-17} cm^2s^{-1} at temperatures below 1400°C and orders of magnitude lower than other, smaller dopants such as phosphorous, aluminum, and nitrogen [109], so arsenic migration due to the thermal spike ionization energy deposition was not anticipated.

Under the 500°C implantation, Figure 7-3(b) differences in As yield between RBS/C random and channeling orientations appears to be independent of post-doping

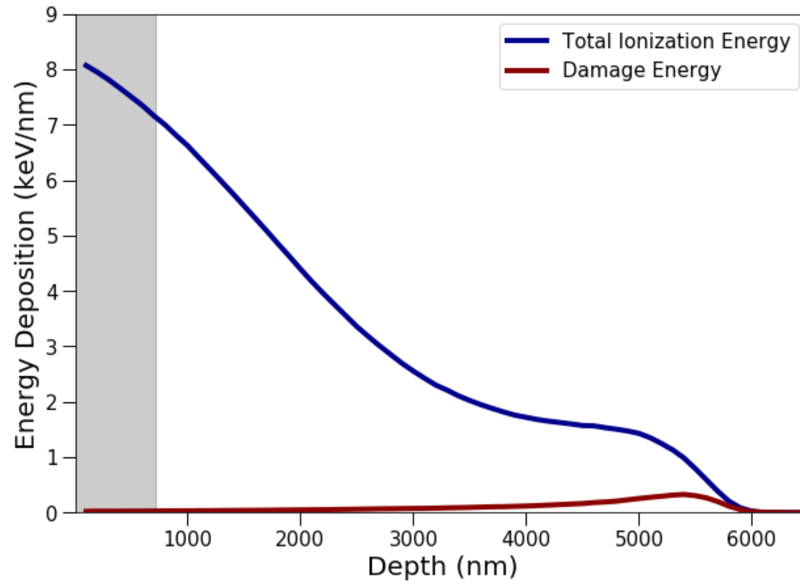

Figure 7-1 SRIM predicted energy partitioning from 21 MeV Ni ions in SiC. Shaded region represents RBS/C characterization probing depth.

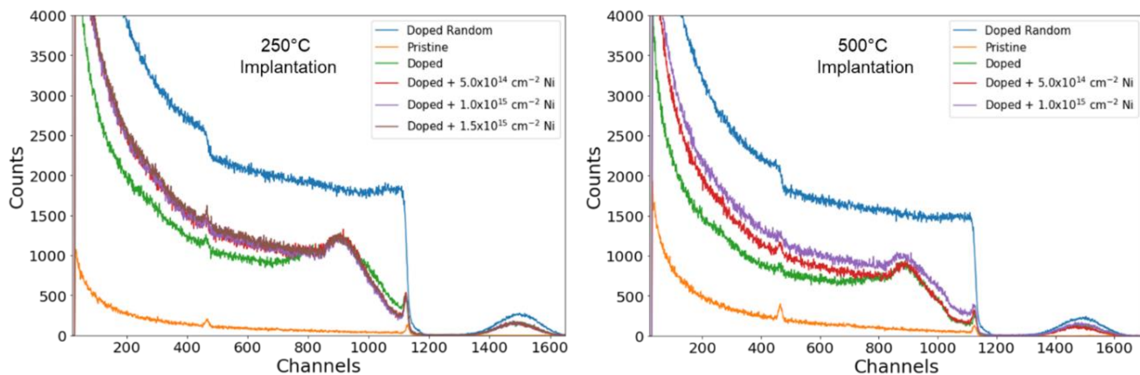

Figure 7-2 Normalized RBS/C spectra of 4H-SiC implanted with 1 MeV As ions at 60° incident angle then irradiated with 21 MeV Ni ions. (Left) Implantations were performed at 250°C and (right) 500°C. All Ni irradiations were performed at room temperature.

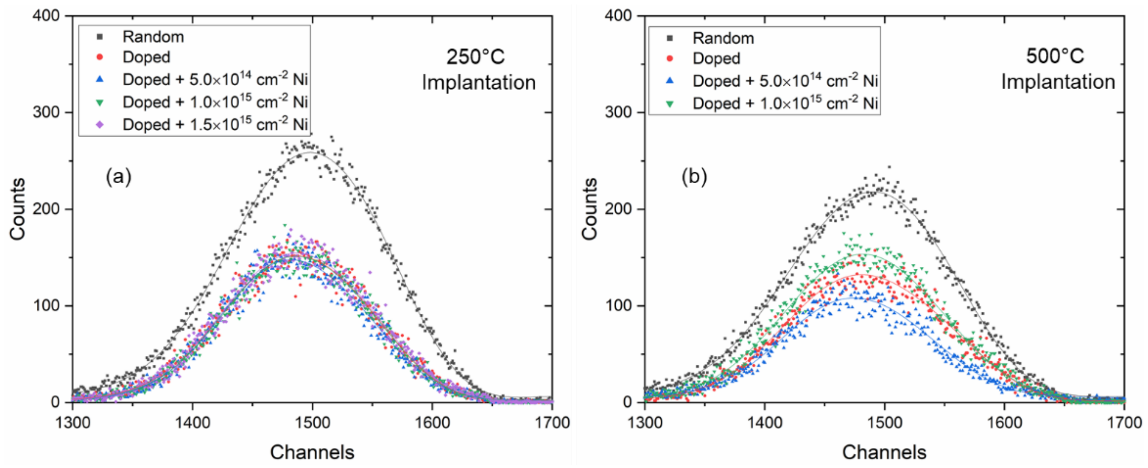

Figure 7-3 RBS/C results of arsenic peak yield and distributions comparison of channeling and random orientations after irradiations at fluences ranging from 5×10^{14} to 1.5×10^{15} cm^{-2} for (a) 250°C implantation and (b) 500°C implantations.

irradiation conditions. However, the ratio of arsenic yields between the spots does correspond to time spent at elevated temperatures after implantations (Table 7-1). This is due to the more mobile defects at 500°C. Figure 7-3(a) shows the As yield and distribution after the 250°C implantation at all spots. Here, As yield of all spots is consistent despite varying time spent at the implantation temperature and irradiation conditions, indicating diminished defect mobility at the lower temperature compared to 500°C. Overall, based on the yield ratios of the RBS/C spectra of As peaks in random to channeling orientations, there is no discernible increase in dopant activation resulting from the Ni irradiation under both implantation conditions, as As activation following the 500°C implantation is attributed to prolonged exposure to the elevated implantation temperature. Under the tested conditions, it is clear that ionization energy deposition from the post implantation irradiation was insufficient to induce measurable activation. This may be attributed to one or both of the following issues:

(1) The ionization induced thermal spike may have too short of a lifetime to induce dopant activation. Zhang, et al. [34] published the predicted SiC lattice temperature induced by ionization energy deposition as a function of both radial distance from the ion path and time resulting from 16 MeV Ni ions (equivalent to 21 MeV Ni ions after traversing through approximately 650 nm into SiC). The most intense predicted temperature resulting from these ions is 1450°C; this is reduced to 680°C in 0.4 ps. It is possible that the kinetics involved in vacancy migration and dopant activation makes it so that the ion induced thermal spike dissipates too quickly to induce activation. If this is the case, adjustments with post-implantation irradiation flux may have a significant impact on dopant behavior, as increasing instances of overlapping ionization energy depositions may result in more time for dopants to move to vacancy sites. However, it is important to note that the thermal spike intensities as a function of time were predicted assuming a defect-free SiC lattice, which would have greater thermal conductivity, a therefore a shorter-lived thermal spike compared to damaged lattice where the presence of defects decreases electron mean free paths.

(2) Insufficient total ionization energy deposition to induce detectable activation. The SRIM predicted energy deposition from the 21 MeV Ni ions is shown in Figure 7-1. The total ionization energy magnitude may not be sufficient to further electrical activation of the dopants after the elevated temperature implantations. Therefore, to induce post-high temperature implantation activation, the use of higher ionization energies may be necessary. Higher energy ions such as SHIs, with energy to mass ratios greater than 1 MeV/amu, that deposit significantly more ionization energy into a material than the tested 21 MeV ions, may be required to induce arsenic activation at room temperature in SiC; such high energy ions are not achievable in the IBML.

7.3 Disorder on the Si-Lattice

A comparison of the RBS/C spectra and disorder on the Si-lattice resulting from the two doping temperatures is shown in Figure 7-4. Both implantation conditions result in multipeak disorder curves on the Si lattice. This is due to enhanced defect migration and segregation These multi-peaks are more resolved in the disorder curves from the 500°C implantation correlating to greater defect mobility from the higher temperature. This behavior has also been observed in SiC under 2 MeV Au irradiation at elevated temperatures; a Au irradiation performed at 177°C induced single peak-shaped disorder while the same irradiation performed at 227°C formed disorder shaped by two peaks [70].

The maximum fractional disorders on the Si lattice from the 250°C and 500°C implantations (fluence of 2×10^{16} cm^{-2}) are 0.51 and 0.44 respectively. The dose (dpa) value at the damage peak from the implantation is 31.5 dpa. While amorphization doses in SiC vary depending on irradiation temperature, irradiation species, and flux [110], both implantations were done at temperatures above the predicted critical temperature for amorphization for similar ions, and amorphization in both 6H- and 4H-SiC has not been observed under comparably high temperatures.

Changes in disorder on the Si-lattice resulting from the Ni irradiations are shown in Figure 7-5. Under the 250°C implantation, disorder is reduced throughout the entire length of the damaged area, with a maximum disorder value decreasing from 0.51 to 0.45

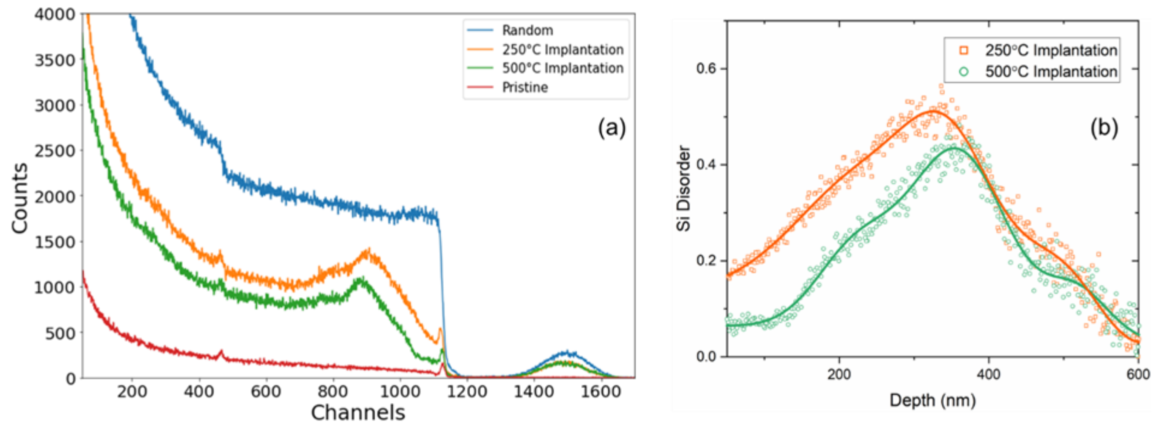

Figure 7-4 (a) RBS/C spectra and (b) disorder measured on the Si lattice comparing 250°C and 500°C doping temperatures.

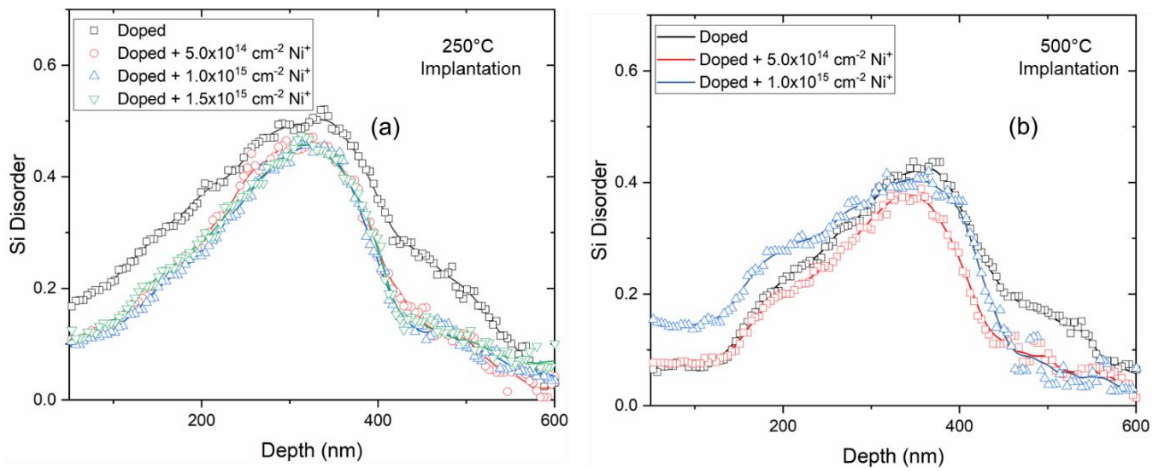

Figure 7-5 Disorder on the Si-lattice (smoothed with the Savitzky-Galay method) from implantations and implantations + Ni irradiations for (a) 250°C implantation temperatures and (b) 500°C implantation temperatures.

after irradiation. This reduction in damage is constant with the Ni fluences employed, evidence that ionization-induced annealing of the implantation damage saturates at a fluence of less than 5×10^{14} cm^{-2}. Under the 500 °C implantation, the Ni irradiation of SiC doped with As does not induce notable annealing at the damage peak. However, there is a reduction in disorder on the Si lattice at depths greater than 400 nm following the Ni irradiation. Mobile point defects and unstable, small defect clusters can diffuse down damage gradients. This was likely occurring under both implantation conditions, leading to defect segregation along the damage depth. Therefore, disorder sensitivity to ionization induced annealing varies depending on depth or damage region. Disorder at the damage peak for both implantations is the least affected by both ionization induced and thermal annealing, indicating a higher concentration of extended and more stable defects compared to other regions on the disorder curves.

Defects remaining after the higher temperature implantation were likely more stable and therefore less affected by ionization effects; however, there are some changes in the disorder distribution with depth that indicates some ionization-induced restructuring. While annealing stages can be difficult to quantify as the onset of any given stage can vary depending on initial damage states, as well as annealing and disorder kinetics [52], 500°C is well above the temperature range typically associated with SiC stage III annealing [80], where close Frenkel pairs recombine, and vacancies begin to migrate typically either agglomerating or annihilating with interstitial clusters [111]. Many of the defects surviving the 500°C implantations were likely extended defects such as clusters or dislocation loops; these are less effected by ionization-induced annealing compared to simpler point defects [34]. Under implantation at 250°C, Si vacancies are largely immobile so point defects likely make up a larger portion of the surviving defects. The initial reduction in disorder in the SiC implanted at 250°C following the lowest irradiation fluence is attributed to the annealing of these point defects, leaving more stable defects not altered by the higher irradiation doses. Most studies of ionization induced annealing of pre-existing defects in SiC look at irradiation effects after damaging at room temperature, where disorder is dramatically reduced following high ionization energy irradiations [71,78,112]. Further

analysis on disorder temperature and the resulting effectiveness of ionization induced annealing would be useful so that predictions on ionization effects on SiC microstructure and electrical properties could be made under all damaging conditions.

Figure 7-6 show the arsenic concentrations calculated from RBS/C spectra in random orientation overlaid with the disorder induced on the Si-lattice following implantations. The arsenic concentration exhibits a Gaussian distribution, peaking near 200 nm with a full width of ~400 nm. This is consistent with both implantation temperatures. The arsenic concentration peaks are also over 100 nm shallower than the damage peaks of the disorder curves on the Si lattice. This is largely due to interstitials, which were formed during the As implantation and are mobile under both implantation temperatures, migrating towards deeper depths. This behavior is consistent with previous implantation studies at elevated temperatures [70,113]. Arsenic peaks do match in depth to unresolved, secondary Si-lattice disorder peaks, correlating to a region rich with As substitutional defects. This region is more pronounced under the 500°C implantation, indicating a greater proportion of As on lattice sites, as expected under the higher temperature doping condition.

7.4 Sheet Resistivity

Sheet resistivity measurements for both implantation conditions are shown in Figure 7-7. The measurements indicate higher sheet resistivities compared to most other SiC-dopant studies [45,106,114–116]. This is partially due to the absence of a post-implantation annealing step performed on the SiC and is evidence to the fact that the post-implantation irradiation did not induce dramatic electrical activation or lattice annealing as postulated. However, implantations were performed with a single energy and dose, so the implanted As atoms have a gaussian distribution peaking approximately 200 nm from the SiC surface. It is difficult to compare sheet resistivity values from this type of doping with the more commonly used box-shaped implantation profiles extending to the substrate surface. Further, dopant species, concentration, and implantation conditions can alter sheet resistivity values by several orders of magnitude, so studies on dopant and defect effects

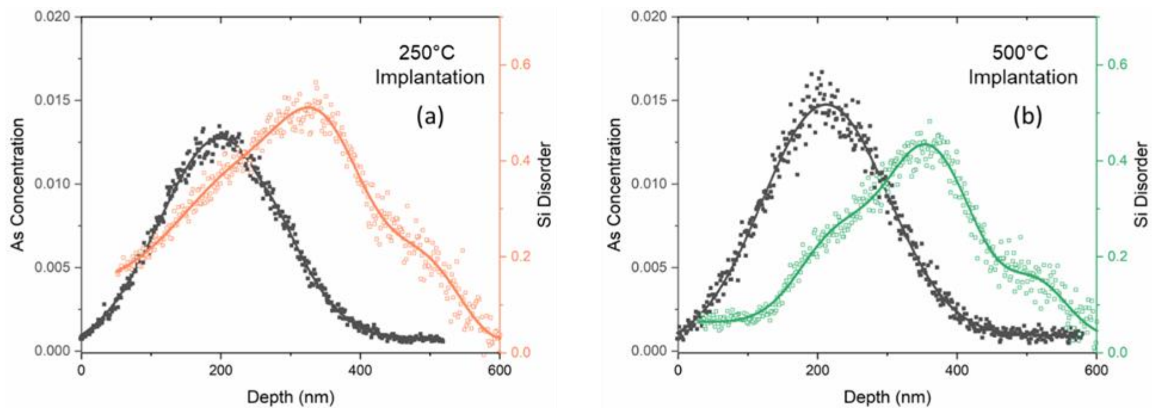

Figure 7-6 Depth profiles of the As yield implanted in SiC overlaid with disorder on the Si-lattice resulting from the As implantation at (a) 250°C and (b) 500°C.

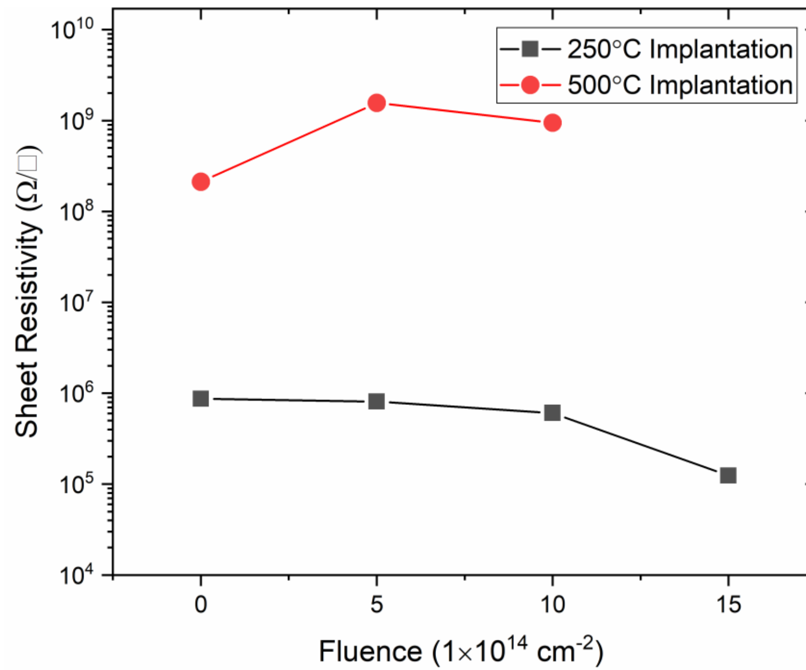

Figure 7-7 Sheet resistivity values as a function of Ni irradiation fluences for 250 and 500°C implantation temperatures.

on electrical properties must be done systematically, as to isolate the impact of individual implantation condition factors on conductivity and carrier concentrations.

Overall sheet resistivity values are higher for the 500°C implantation compared with the 250°C implantation. The electrical properties of SiC and other semiconductors are extremely sensitive to defect type, size, and concentration [117–119]. Therefore, the increase of sheet resistivity with implantation temperature is likely due to the higher concentration of extended and thermally stable defects following implantation.

For the 250°C implantation, the sheet resistivity decreases with increasing 21 MeV Ni irradiation fluence. This is indicative of irradiation-induced annealing of defects, which is also shown in the Si-disorder plots in Figure 7-5(a) via RBS/C analysis. However, the measured disorder on the Si-lattice does not significantly decrease with irradiation fluence as observed for the sheet resistivity measurements; likely because resistivity measurements are much more sensitive to defect concentrations compared to RBS/C analysis.

The interpretation of the sheet resistivity values for the 500°C implantation is less straight forward. These values do not correlate directly with either irradiation fluence or time spent at the implantation temperature. With a higher concentration of extended defects, more complex defect recovery and growth interactions may be taking place. The implanted sample irradiated to a Ni ion fluence of 5×10^{14} cm^{-2} has the lowest concentration of As atoms in interstitial sites and the lowest Si disorder compared to other implanted areas, yet has the highest measured sheet resistivity. This area spent the longest time at 500°C following implantation, and it is possible that while overall disorder is reduced, the surviving defects are more effective at trapping charge carriers or limiting mobility. The reduction in sheet resistivity when increasing the fluence from 5×10^{14} cm^{-2} to 1×10^{15} cm^{-2} may then be due to a combination of (1) the breakup of defect clusters at the higher fluence and (2) less stable extended defects being formed as this area spent over three hours less at 500°C compared to the 5×10^{14} cm^{-2} fluence area. Comparable behavior was observed by Negoro et al. [45] in 4H-SiC doped with Al ions to a fluence of 3×10^{16} cm^{-2} then annealed at 1800°C; with increasing annealing times (starting at 1 min to 180

min), sheet resistivity decreased. This was attributed to longer annealing times forming secondary defects.

CHAPTER EIGHT

CONCLUSIONS

SiC is an important structural and electronic material for nuclear and other harsh environment applications where irradiation exposure is a concern. This work examines the complex relationship between incident ion ionization and damage energy deposition and its resulting microstructural impact on doped- and pristine-single crystal SiC. This was done via ion irradiation experiments and ion beam analysis. Ionization-induced annealing can significantly alter disordering behavior in SiC, and total understanding of this effect, both separate and coupled with damage energy dissipation, is necessary to develop predictive models of SiC-based structural materials and electronic devices exposed to harsh radiation environments.

Chapter 5 compares 3C-SiC disorder accumulation resulting from 10 MeV Au ions with the disorder accumulation resulting from 5 MeV Si ions. The two irradiating ion species have comparable ionization energy deposition and pathlengths in SiC, however the damage energy of 5 MeV Si ions is significantly lower than 10 MeV Au ions. There is stronger coupling between inelastic and elastic processes for 5 MeV Si ions. Therefore, the formation, migration, and annihilation of irradiation-induced defects from the Si ions are more sensitive to changes in ionization energy compared to defects from the Au ions. Au ions have a more energetic recoil spectrum leading to weaker spatial coupling between energy deposition processes. This harder recoil spectrum from the Au ions is more comparable to neutrons. Consequently, SiC damage at similar dpa doses is greater from the Au ions compared to the Si ions.

The coupled effects of the two ion energy deposition processes are further studied in chapter 6, which compares disordering processes in 4H-SiC using Si, Ti, and Ni ions with energies ranging from 10 to 23 MeV. There are ionization energy thresholds above which, ion irradiation induced disorder is totally suppressed by inelastic energy deposition processes. These thresholds increase sub-linearly with incident ion atomic number and range from 1.86 keV/nm for C atoms to 8.34 keV/nm for Ni ions. Below these thresholds, dynamic ionization annealing occurs. This decreases the damage production rate and, under

the right conditions, can lead to damage saturation with increasing irradiation doses due to an equilibrium between defect production and ionization induced annealing.

Ionization energy deposition also induces annealing in 4H-SiC pre-damaged from elevated-temperature, As implantations. The magnitude of the annealing depends on implantation temperature and, consequently, the type of defects that survive implantation. Disorder from As implantations at 500°C are less sensitive to ionization-induced annealing compared to disorder from a 250°C implantation as the surviving damage from the higher temperature implantation is associated with larger concentrations of more thermally stable defects. A graphical summary of the experiments and conclusions of this work are shown in Figure 8-1.

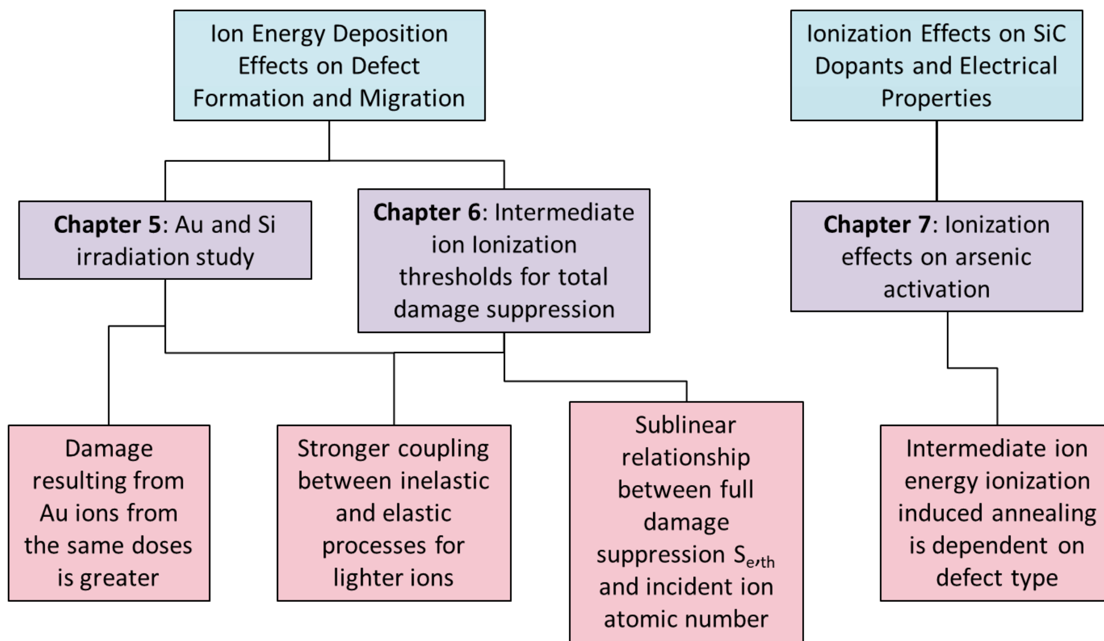

Figure 8-1 Graphical summary of the experiments and conclusions of this work.

LIST OF REFERENCES

[1] R.O. Niehoff, Organization and Administration of the United States Atomic Energy Commission, Public Adm. Rev. 8 (1948) 91. doi:10.2307/972379.
[2] R.S. Lowen, Entering the Atomic Power Race : Science, Industry, and Government, Polit. Sci. Q. 102 (1987) 459–479. doi:10.2307/2151403.
[3] 17th Seminnual Report of the Atomic Energy Commission, 1959. doi:10.1038/183437b0.
[4] J. Wood, Nuclear power, 2007. doi:10.1049/PBPO052E.
[5] S.M. Goldberg, R. Rosner, Nuclear Reactors: Generation to Generation, American Academy of Arts and Sciences, 2011.
[6] GEN IV International Forum, Technology Roadmap Update for Generation IV Nuclear Energy Systems, (2014). https://www.gen-4.org/gif/jcms/c_60729 /technology-roadmap-update-2013.
[7] C. Steven, Y. Cui, N. Liu, Materials for sustainable energy, Nat. Mater. 16 (2016) 15. doi:10.1038/nmat4838.
[8] Thomas J.Crowley, Causes of Climate Change Over the Past 1000 years, Science (80-.). 289 (2000) 270–277. doi:10.1126/science.289.5477.270.
[9] S.J. Zinkle, J.T. Busby, Structural materials for fission & fusion energy, Mater. Today. 12 (2009) 12–19. doi:10.1016/S1369-7021(09)70294-9.
[10] S.J. Zinkle, G.S. Was, Materials challenges in nuclear energy, Acta Mater. 61 (2013) 735–758. doi:10.1016/j.actamat.2012.11.004.
[11] GEN IV International Forum, GIF R&D Outlook for Generation IV Nuclear Energy Systems 2018 Update, (2018). https://www.gen-4.org/gif/jcms/c_108744/gif-r-d-outlook-for-generation-iv-nuclear-energy-systems-2018-update?details=true.
[12] P. Teplov, A. Chibiniaev, E. Bobrov, P. Alekseev, The main characteristics of the evoluation project VVER-S with spectrum shift regulation, in: Int. Conf. Phys. React., IAEA, 2015. doi:10.11484/jaea-conf-2014-003.
[13] C. Till, Y. Chang, W. Hannum, The Integral Fast Reactor-An Overview, Prog. Nucl. Energy. 31 (1997) 3–11. doi:10.1016/0149-1970(96)00001-7.
[14] I.L. Pioro, Handbook of Generation IV Nuclear Reactors, Woodhead Publishing, 2016. doi:10.1016/C2014-0-01699-1.
[15] W.F.G. Van Rooijen, Gas-cooled fast reactor: A historical overview

and future outlook, Sci. Technol. Nucl. Install. 2009 (2009). doi:10.1155/2009/965757.

[16] T.T. Yi, S. Koshizuka, Y. Oka, A linear stability analysis of supercritical water reactors, (II) coupled neutronic thermal-hydraulic stability, J. Nucl. Sci. Technol. 41 (2004) 1176–1186. doi:10.1080/18811248.2004.9726346.

[17] M. Kikuchi, A review of fusion and tokamak research towards steady-state operation: A JAEA contribution, Energies. 3 (2010) 1741–1789. doi:10.3390/en3111741.

[18] A. Haidari, Designing Nuclear Fusion Reactors with Simulation, Ansys. (2019). https://www.ansys.com/blog/designing-nuclear-fusion-reactors-simulation.

[19] Y. Shimomura, R. Aymar, V. Chuyanov, M. Huguet, R. Parker, I.J.C. Team, {ITER} overview, Nucl. Fusion. 39 (1999) 1295–1308. doi:10.1088/0029-5515/39/9y/307.

[20] LLNL, Inertial Confinement Fusion: How to make a star, Natl. Ignition Facil. Phot. Sci. (n.d.). https://lasers.llnl.gov/science/icf.

[21] R. Betti, O.A. Hurricane, Inertial-Confinement fusion with lasers, Nat. Phys. 12 (2016) 445–448. doi:10.1038/NPHYS3736.

[22] K. Nordlund, S.J. Zinkle, A.E. Sand, F. Granberg, R.S. Averback, R.E. Stoller, T. Suzudo, L. Malerba, F. Banhart, W.J. Weber, F. Willaime, S.L. Dudarev, D. Simeone, Primary radiation damage: A review of current understanding and models, J. Nucl. Mater. 512 (2018) 450–479. doi:10.1016/j.jnucmat.2018.10.027.

[23] M.I. Norgett, M.. T. Robinson, I.M. Torrens, A Proposed Method of Calculating Displacement Dose Rates, Nucl. Eng. Des. 33 (1975) 50–54.

[24] P. Joshi, T. Aytug, S. Mahurin, R. Mayes, S. Cetiner, H. Wang, I. Kravchenko, Y. Zhang, A. Ievlev, L. Nuckols, R. Kisner, Piezoresistive characteristics of silicon carbide for integrated sensor applications, 11th Nucl. Plant Instrumentation, Control. Human-Machine Interface Technol. NPIC HMIT 2019. (2019) 1416–1424.

[25] P. Godignon, X. Jorda, M. Vellvehi, X. Perpina, V. Banu, D. Lopez, J. Barbero, P. Brosselard, S. Massetti, SiC Schottky diodes for harsh environment space applications, IEEE Trans. Ind. Electron. 58 (2011) 2582–2589. doi:10.1109/TIE.2010.2080252.

[26] R. Scheidegger, W. Santiago, K.E. Bozak, L.R. Pinero, A.

Birchenough, (Invited) High Power SiC Power Processing Unit Development, ECS Trans. 69 (2015) 13–19. doi:10.1149/06911.0013ecst.
[27] L.L. Snead, T. Nozawa, Y. Katoh, T.-S. Byun, S. Kondo, D.A. Petti, Handbook of SiC properties for fuel performance modeling, J. Nucl. Mater. 371 (2007) 329–377. doi:10.1016/J.JNUCMAT.2007.05.016.
[28] L. Gordon, A. Janotti, C.G. Van De Walle, Defects as qubits in 3C- and 4H-SiC, Phys. Rev. B - Condens. Matter Mater. Phys. 92 (2015) 1–5. doi:10.1103/PhysRevB.92.045208.
[29] R.W. Olesinski, G.J. Abbaschian, The C−Si (Carbon-Silicon) system, Bull. Alloy Phase Diagrams. 5 (1984) 486–489. doi:10.1007/BF02872902.
[30] W.J. Choyke, G. Pensl, Physical properties of SiC, MRS Bull. (1997) 25–29. doi:10.1111/j.2041-6962.1997.tb00844.x.
[31] C.-H. Chen, Ion Irradiation-induced Microstructural Change in SiC, University of Tennessee, 2015. https://trace.tennessee.edu/utk_graddiss/3566.
[32] P. Liu, Atomic Structure of the Vicinal Interface between Silicon Carbide and Silicon Dioxide, 2014. http://trace.tennessee.edu/utk_graddiss/2708/.
[33] R.H. Jones, L. Giancarli, A. Hasegawa, Y. Katoh, A. Kohyama, B. Riccardi, L.L. Snead, W.J. Weber, Promise and challenges of SiCf/SiC composites for fusion energy applications, J. Nucl. Mater. 307–311 (2002) 1057–1072. doi:10.1016/S0022-3115(02)00976-5.
[34] Y. Zhang, H. Xue, E. Zarkadoula, R. Sachan, C. Ostrouchov, P. Liu, X. lin Wang, S. Zhang, T.S. Wang, W.J. Weber, Coupled electronic and atomic effects on defect evolution in silicon carbide under ion irradiation, Curr. Opin. Solid State Mater. Sci. 21 (2017) 285–298. doi:10.1016/j.cossms.2017.09.003.
[35] L.L. Snead, T. Nozawa, M. Ferraris, Y. Katoh, R. Shinavski, M. Sawan, Silicon carbide composites as fusion power reactor structural materials, J. Nucl. Mater. 417 (2011) 330–339. doi:10.1016/j.jnucmat.2011.03.005.
[36] H. Bolt, V. Barabash, W. Krauss, J. Linke, R. Neu, S. Suzuki, N. Yoshida, Materials for the plasma-facing components of fusion reactors, J. Nucl. Mater. 329–333 (2004) 66–73. doi:10.1016/j.jnucmat.2004.04.005.

[37] M.R. Gilbert, J.C. Sublet, Neutron-induced transmutation effects in W and W-alloys in a fusion environment, Nucl. Fusion. 51 (2011). doi:10.1088/0029-5515/51/4/043005.
[38] C.H. Chen, Y. Zhang, E. Fu, Y. Wang, M.L. Crespillo, C. Liu, S. Shannon, W.J. Weber, Irradiation-induced microstructural change in helium-implanted single crystal and nano-engineered SiC, J. Nucl. Mater. 453 (2014) 280–286. doi:10.1016/j.jnucmat.2014.07.020.
[39] M. Rebai, D. Rigamonti, S. Cancelli, G. Croci, G. Gorini, E. Perelli Cippo, O. Putignano, M. Tardocchi, C. Altana, M. Angelone, G. Borghi, M. Boscardin, C. Ciampi, G.A.P. Cirrone, A. Fazzi, D. Giove, L. Labate, G. Lanzalone, F. La Via, S. Loreti, A. Muoio, P. Ottanelli, G. Pasquali, M. Pillon, S.M.R. Puglia, A. Santangelo, A. Trifiro, S. Tudisco, New thick silicon carbide detectors: Response to 14 MeV neutrons and comparison with single-crystal diamonds, Nucl. Instruments Methods Phys. Res. Sect. A Accel. Spectrometers, Detect. Assoc. Equip. 946 (2019) 162637. doi:10.1016/j.nima.2019.162637.
[40] L. Wang, J. Jarrell, S. Xue, C. Tan, T. Blue, L.R. Cao, Fast neutron detection at near-core location of a research reactor with a SiC detector, Nucl. Instruments Methods Phys. Res. Sect. A Accel. Spectrometers, Detect. Assoc. Equip. 888 (2018) 126–131. doi:10.1016/j.nima.2018.01.070.
[41] B. Riccardi, L. Giancarli, A. Hasegawa, Y. Katoh, A. Kohyama, R.H. Jones, L.L. Snead, Issues and advances in SiC_f/SiC composites development for fusion reactors, J. Nucl. Mater. 329–333 (2004) 56–65. doi:10.1016/j.jnucmat.2004.04.002.
[42] M.E. Sawan, Y. Katoh, L.L. Snead, Transmutation of silicon carbide in fusion nuclear environment, J. Nucl. Mater. 442 (2013) 370–375. doi:10.1016/j.jnucmat.2012.11.018.
[43] L.L. Snead, R.H. Jones, A. Kohyama, P. Fenici, Status of silicon carbide composites for fusion, J. Nucl. Mater. (1996).
[44] M.E. Sawan, L. Snead, S. Zinkle, Radiation damage parameters for SiC/SiC composite structure in fusion nuclear environment, Fusion Sci. Technol. 44 (2003) 150–154. doi:10.13182/FST03-A325.
[45] Y. Negoro, T. Kimoto, H. Matsunami, F. Schmid, G. Pensl, Electrical activation of high-concentration aluminum implanted in 4H-SiC, J. Appl. Phys. 96 (2004) 4916–4922. doi:10.1063/1.1796518.
[46] J.S. Williams, J.M. Poate, Ion Implantation and Beam Processing,

Academic Press, 1984. doi:10.1016/C2013-0-07644-X.
[47] A. Hallén, M. Linnarsson, Ion implantation technology for silicon carbide, Surf. Coatings Technol. 306 (2016) 190–193. doi:10.1016/j.surfcoat.2016.05.075.
[48] S. Ahmed, C.J. Barbero, T.W. Sigmon, Activation of ion implanted dopants in α-SiC, Appl. Phys. Lett. 712 (1995) 712. doi:10.1063/1.114108.
[49] G.S. Was, Z. Jiao, E. Getto, K. Sun, A.M. Monterrosa, S.A. Maloy, O. Anderoglu, B.H. Sencer, M. Hackett, Emulation of reactor irradiation damage using ion beams, Scr. Mater. 88 (2014) 33–36. doi:10.1016/j.scriptamat.2014.06.003.
[50] S.J. Zinkle, N.M. Ghoniem, Operating temperature windows for fusion reactor structural materials, Fusion Eng. Des. 51–52 (2000) 55–71. doi:10.1016/S0920-3796(00)00320-3.
[51] G. Ilas, D. Chandler, B.J. Ade, E.E. Sunny, B.R. Betzler, D. Pinkston, Modeling and Simulations of the High Flux Isotope Reactor Cycle 400, 2015. doi:10.2172/1185903.
[52] G.S. Was, Fundamentals of radiation materials science: Metals and alloys, 2007. doi:10.1007/978-3-540-49472-0.
[53] L. Mansur, Theory of transitions in dose dependence of radiation effects in structural alloys, J. Nucl. Mater. 206 (1993) 306–323. doi:10.1016/0022-3115(93)90130-Q.
[54] L.L. Snead, S.J. Zinkle, J.C. Hay, M.C. Osborne, Amorphization of SiC under ion and neutron irradiation, Nucl. Instruments Methods Phys. Res. Sect. B Beam Interact. with Mater. Atoms. 141 (1998) 123–132. doi:10.1016/S0168-583X(98)00085-8.
[55] Y. Katoh, N. Hashimoto, S. Kondo, L.L. Snead, A. Kohyama, Microstructural development in cubic silicon carbide during irradiation at elevated temperatures, J. Nucl. Mater. 351 (2006) 228–240. doi:10.1016/j.jnucmat.2006.02.007.
[56] G. Was, Fundamentals of Radiation Materials Science, second, Springer Science, New York, 2017.
[57] J.F. (James F.. Ziegler, J.P. Biersack, M.D. Ziegler, SRIM, the stopping and range of ions in matter, (2008). doi:10.1016/j.nimb.2004.01.208.4.
[58] J.F. Ziegler, the Stopping and Range of Ions in Solids, ACADEMIC PRESS, INC., 1984. doi:10.1016/b978-0-12-780620-4.50007-0.

[59] W.J. Weber, Y. Zhang, Predicting damage production in monoatomic and multi-elemental targets using stopping and range of ions in matter code: Challenges and recommendations, Curr. Opin. Solid State Mater. Sci. 23 (2019) 100757. doi:10.1016/j.cossms.2019.06.001.
[60] M. Toulemonde, C. Dufour, A. Meftah, E. Paumier, Transient thermal processes in heavy ion irradiation of crystalline inorganic insulators, Beam Interact. with Mater. Atoms. 166–167 (2000) 903–912. doi:10.1016/S0168-583X(99)00799-5.
[61] W.J. Weber, D.M. Duffy, L. Thomé, Y. Zhang, The role of electronic energy loss in ion beam modification of materials, Curr. Opin. Solid State Mater. Sci. 19 (2015) 1–11. doi:10.1016/j.cossms.2014.09.003.
[62] A. Benyagoub, Irradiation effects induced in silicon carbide by low and high energy ions, Nucl. Instruments Methods Phys. Res. Sect. B Beam Interact. with Mater. Atoms. 266 (2008) 2766–2771. doi:10.1016/j.nimb.2008.03.113.
[63] H. Xue, Y. Zhang, W.J. Weber, In-cascade ionization effects on defect production in 3C silicon carbide*, Mater. Res. Lett. 5 (2017) 494–500. doi:10.1080/21663831.2017.1334241.
[64] Y. Zhang, W.J. Weber, Ion irradiation and modification: The role of coupled electronic and nuclear energy dissipation and subsequent nonequilibrium processes in materials, Appl. Phys. Rev. 7 (2020) 041307. doi:10.1063/5.0027462.
[65] L. Nuckols, M.L. Crespillo, Y. Yang, J. Li, E. Zarkadoula, Y. Zhang, W.J. Weber, Effects of recoil spectra and electronic energy dissipation on defect survival in 3C-SiC, Materialia. 15 (2021) 101023. doi:10.1016/j.mtla.2021.101023.
[66] R.E. Stoller, M.B. Toloczko, G.S. Was, A.G. Certain, S. Dwaraknath, F.A. Garner, On the use of SRIM for computing radiation damage exposure, Nucl. Instruments Methods Phys. Res. Sect. B Beam Interact. with Mater. Atoms. 310 (2013) 75–80. doi:10.1016/j.nimb.2013.05.008.
[67] S.J. Zinkle, J.W. Jones, V.A. Skuratov, Microstructure of Swift Heavy Ion Irradiated SiC, Si_3N_4, and AlN, in: MRS Bull., 2000: pp. 136–142.
[68] M. Levalois, P. Marie, Damage induced in semiconductors by swift heavy ion irradiation, Nucl. Instruments Methods Phys. Res. Sect. B Beam Interact. with Mater. Atoms. 156 (1999) 64–71. doi:10.1016/S0168-583X(99)00243-8.

[69] S.J. Zinkle, V.A. Skuratov, D.T. Hoelzer, On the conflicting roles of ionizing radiation in ceramics, Nucl. Instruments Methods Phys. Res. Sect. B Beam Interact. with Mater. Atoms. 191 (2002) 758–766. doi:10.1016/S0168-583X(02)00648-1.
[70] W. Jiang, W.J. Weber, Y. Zhang, S. Thevuthasan, V. Shutthanandan, Ion beam analysis of irradiation effects in 6H-SiC, Nucl. Instruments Methods Phys. Res. Sect. B Beam Interact. with Mater. Atoms. 207 (2003) 92–99. doi:10.1016/S0168-583X(03)00527-5.
[71] A. Benyagoub, A. Audren, L. Thomé, F. Garrido, Athermal crystallization induced by electronic excitations in ion-irradiated silicon carbide, Appl. Phys. Lett. 89 (2006) 5–8. doi:10.1063/1.2405410.
[72] T.T. Hlatshwayo, J.H. O'Connell, V.A. Skuratov, E. Wendler, E.G. Njoroge, M. Mlambo, J.B. Malherbe, Comparative study of the effect of swift heavy ion irradiation at 500 °C and annealing at 500 °C on implanted silicon carbide, RSC Adv. 6 (2016) 68593–68598. doi:10.1039/c6ra13592g.
[73] V.A. Skuratov, J. O'Connell, A.S. Sohatsky, J. Neethling, TEM study of damage recovery in SiC by swift Xe ion irradiation, Nucl. Instruments Methods Phys. Res. Sect. B Beam Interact. with Mater. Atoms. 327 (2014) 89–92. doi:10.1016/j.nimb.2013.10.082.
[74] A. Debelle, M. Backman, L. Thomé, W.J. Weber, M. Toulemonde, S. Mylonas, A. Boulle, O.H. Pakarinen, N. Juslin, F. Djurabekova, K. Nordlund, F. Garrido, D. Chaussende, Combined experimental and computational study of the recrystallization process induced by electronic interactions of swift heavy ions with silicon carbide crystals, Phys. Rev. B - Condens. Matter Mater. Phys. 86 (2012) 2–5. doi:10.1103/PhysRevB.86.100102.
[75] A. Debelle, M. Backman, L. Thomé, K. Nordlund, F. Djurabekova, W.J. Weber, I. Monnet, O.H. Pakarinen, F. Garrido, F. Paumier, Swift heavy ion induced recrystallization in cubic silicon carbide: New insights from designed experiments and MD simulations, Nucl. Instruments Methods Phys. Res. Sect. B Beam Interact. with Mater. Atoms. 326 (2014) 326–331. doi:10.1016/j.nimb.2013.10.080.
[76] A. Audren, I. Monnet, D. Gosset, Y. Leconte, X. Portier, L. Thomé, F. Garrido, A. Benyagoub, M. Levalois, N. Herlin-Boime, C. Reynaud, Effects of electronic and nuclear interactions in SiC, Nucl. Instruments

Methods Phys. Res. Sect. B Beam Interact. with Mater. Atoms. 267 (2009) 976–979. doi:10.1016/j.nimb.2009.02.033.

[77] S. Sorieul, X. Kerbiriou, J.M. Costantini, L. Gosmain, G. Calas, C. Trautmann, Optical spectroscopy study of damage induced in 4H-SiC by swift heavy ion irradiation, J. Phys. Condens. Matter. 24 (2012). doi:10.1088/0953-8984/24/12/125801.

[78] Y. Zhang, R. Sachan, O.H. Pakarinen, M.F. Chisholm, P. Liu, H. Xue, W.J. Weber, Ionization-induced annealing of pre-existing defects in silicon carbide, Nat. Commun. 6 (2015) 8049. doi:10.1038/ncomms9049.

[79] W.J. Weber, Models and mechanisms of irradiation-induced amorphization in ceramics, Nucl. Instruments Methods Phys. Res. Sect. B Beam Interact. with Mater. Atoms. 166 (2000) 98–106. doi:10.1016/S0168-583X(99)00643-6.

[80] W.J. Weber, W. Jiang, S. Thevuthasan, Accumulation, dynamic annealing and thermal recovery of ion-beam-induced disorder in silicon carbide, Nucl. Instruments Methods Phys. Res. Sect. B Beam Interact. with Mater. Atoms. 175–177 (2001) 26–30. doi:10.1016/S0168-583X(00)00542-5.

[81] W. Jiang, W.J. Weber, S. Thevuthasan, V. Shutthanandan, Accumulation and recovery of disorder on silicon and carbon sublattices in ion-irradiated 6H-SiC, J. Nucl. Mater. 289 (2001) 96–101. doi:10.1016/S0022-3115(00)00687-5.

[82] W.J. Weber, L.M. Wang, N. Yu, N.J. Hess, Structure and properties of ion-beam-modified (6H) silicon carbide, Mater. Sci. Eng. A. 253 (1998) 62–70. doi:10.1016/s0921-5093(98)00710-2.

[83] W. Jiang, W.J. Weber, S. Thevuthasan, D.E. McCready, Damage formation and recovery in C^+-irradiated 6H-SiC, Nucl. Instruments Methods Phys. Res. Sect. B Beam Interact. with Mater. Atoms. 148 (1999) 562–566. doi:10.1016/S0168-583X(98)00716-2.

[84] W.J. Weber, N. Yu, L.M. Wang, N.J. Hess, Temperature and dose dependence of ion-beam-induced amorphization in α-SiC, J. Nucl. Mater. 244 (1997) 258–265. doi:10.1016/S0022-3115(96)00742-8.

[85] A. Heft, E. Wendler, T. Bachmann, E. Glaser, W. Wesch, Defect production and annealing in ion implanted silicon carbide, Mater. Sci. Eng. B29 (1995) 142–146. doi:10.1557/JMR.1997.0238.

[86] S.J. Zinkle, L.L. Snead, Influence of irradiation spectrum and

implanted ions on the amorphization of ceramics, Nucl. Instruments Methods Phys. Res. Sect. B Beam Interact. with Mater. Atoms. 116 (1996) 92–101. doi:10.1016/0168-583X(96)00016-X.
[87] W.J. Weber, L.M. Wang, N. Yu, The irradiation-induced crystalline-to-amorphous phase transition in a-SiC, Nucl. Instruments Methods Phys. Res. 116 (1996) 322–326.
[88] P. Schuh, J. Steiner, F. La Via, M. Mauceri, M. Zielinski, P.J. Wellmann, Limitations during vapor phase growth of bulk (100) 3C-SiC using 3C-SiC-on-SiC seeding stacks, Materials (Basel). 12 (2019) 1–8. doi:10.3390/ma12152353.
[89] F. La Via, A. Severino, R. Anzalone, C. Bongiorno, G. Litrico, M. Mauceri, M. Schoeler, P. Schuh, P. Wellmann, From thin film to bulk 3C-SiC growth: Understanding the mechanism of defects reduction, Mater. Sci. Semicond. Process. 78 (2018) 57–68. doi:10.1016/j.mssp.2017.12.012.
[90] R. Devanathan, W.J. Weber, F. Gao, Atomic scale simulation of defect production in irradiated 3C-SiC, J. Appl. Phys. 90 (2001) 2303–2309. doi:10.1063/1.1389523.
[91] C. Ostrouchov, Y. Zhang, W.J. Weber, pysrim: Automation, Analysis, and Plotting of SRIM Calculations, J. Open Source Softw. 3 (2018). doi:10.21105/joss.00829.
[92] Y. Zhang, M.L. Crespillo, H. Xue, K. Jin, C.H. Chen, C.L. Fontana, J.T. Graham, W.J. Weber, New ion beam materials laboratory for materials modification and irradiation effects research, Nucl. Instruments Methods Phys. Res. Sect. B Beam Interact. with Mater. Atoms. 338 (2014) 19–30. doi:10.1016/j.nimb.2014.07.028.
[93] W.-K. Chu, J.W. Mayer, M.-A. Nicolet, Backscattering Spectrometry, First, Academic Press, New York, 1978.
[94] Y. Wang, M. Nastasi, Handbook of Modern Ion Beam Materials Analysis, second, Cambridge University Press, 2010.
[95] Y. Zhang, J. Lian, Z. Zhu, W.D. Bennett, L. V. Saraf, J.L. Rausch, C.A. Hendricks, R.C. Ewing, W.J. Weber, Response of strontium titanate to ion and electron irradiation, J. Nucl. Mater. 389 (2009) 303–310. doi:10.1016/j.jnucmat.2009.02.014.
[96] K. Jin, Y. Zhang, Z. Zhu, D.A. Grove, H. Xue, J. Xue, W.J. Weber, K. Jin, Y. Zhang, Z. Zhu, D.A. Grove, H. Xue, J. Xue, W.J. Weber, Electronic stopping powers for heavy ions in SiC and SiO_2, 044903

(2015). doi:10.1063/1.4861642.
[97] Y.G. Li, Y. Yang, M.P. Short, Z.J. Ding, Z. Zeng, J. Li, IM3D: A parallel Monte Carlo code for efficient simulations of primary radiation displacements and damage in 3D geometry, Sci. Rep. 5 (2015) 1–13. doi:10.1038/srep18130.
[98] D. Guo, H. Zang, P. Zhang, J. Xi, T. Li, L. Ma, C. He, Analysis of primary damage in silicon carbide under fusion and fission neutron spectra, J. Nucl. Mater. 455 (2014) 229–233. doi:10.1016/j.jnucmat.2014.06.001.
[99] W.. J. Weber, W. Jiang, F. Gao, R. Devanathan, Ion – solid interactions and defects in silicon carbide, Nucl. Inst. Methods Phys. Res. B. 190 (2002) 261–265.
[100] W.J. Weber, F. Gao, R. Devanathan, W. Jiang, The efficiency of damage production in silicon carbide, Nucl. Instruments Methods Phys. Res. Sect. B Beam Interact. with Mater. Atoms. 218 (2004) 68–73. doi:10.1016/j.nimb.2003.12.006.
[101] L. Nuckols, M.L. Crespillo, C. Xu, E. Zarkadoula, Y. Zhang, W.J. Weber, Coupled effects of electronic and nuclear energy deposition on damage accumulation in ion-irradiated SiC, Acta Mater. 199 (2020) 96–106. doi:10.1016/j.actamat.2020.08.014.
[102] E. Wendler, A. Heft, W. Wesch, Ion-beam induced damage and annealing behaviour in SiC, Nucl. Instruments Methods Phys. Res. Sect. B Beam Interact. with Mater. Atoms. 141 (1998) 105–117. doi:10.1016/S0168-583X(98)00083-4.
[103] F.N. Cue, D.E.C. Faria, M.J. Gaillard, J.C. Poizat, J. Remillieux, Electron Loss and Capture Cross Sections of 800keV/amu H and He Species in Carbon Foils, in: 8th Int. Conf. At. Collisions Soilds, Hamilton, Canada, 1979.
[104] Y. Zhang, W.J. Weber, W. Jiang, C.M. Wang, V. Shutthanandan, A. Hallén, Effects of implantation temperature on damage accumulation in Al-implanted 4H-SiC, J. Appl. Phys. 95 (2004) 4012–4018. doi:10.1063/1.1666974.
[105] W. Jiang, Y. Zhang, W.J. Weber, Temperature dependence of disorder accumulation and amorphization in Au-ion-irradiated 6H-SiC [48], Phys. Rev. B - Condens. Matter Mater. Phys. 70 (2004) 1–8. doi:10.1103/PhysRevB.70.165208.
[106] J. Senzaki, K. Fukuda, S. Imai, Y. Tanaka, N. Kobayashi, H. Tanoue,

H. Okushi, K. Arai, Electrical characteristics and surface morphology for arsenic ion-implanted 4H-SiC at high temperature, Mater. Sci. Forum. 338 (2000) 865–868. doi:10.4028/www.scientific.net/msf.338-342.865.
[107] E.N. Mokhov, Doping of SiC Crystals during Sublimation Growth and Diffusion, in: Cryst. Growth, 2018. doi:http://dx.doi.org/10.5772/57353.
[108] A. Hallén, M.S. Janson, A.Y. Kuznetsov, D. Åberg, M.K. Linnarsson, B.G. Svensson, P.O. Persson, F.H.C. Carlsson, L. Storasta, J.P. Bergman, S.G. Sridhara, Y. Zhang, Ion implantation of silicon carbide, Nucl. Instruments Methods Phys. Res. Sect. B Beam Interact. with Mater. Atoms. 186 (2002) 186–194. doi:10.1016/S0168-583X(01)00880-1.
[109] T. Kimoto, J.A. Cooper, Fundamentals of Silicon Carbide Technology, Wiley, 2014. doi:10.1002/9781118313534.
[110] L.L. Snead, S.J. Zinkle, Structural relaxation in amorphous silicon carbide, Nucl. Instruments Methods Phys. Res. Sect. B Beam Interact. with Mater. Atoms. 191 (2002) 497–503. doi:10.1016/S0168-583X(02)00599-2.
[111] M.J. Zheng, N. Swaminathan, D. Morgan, I. Szlufarska, Energy barriers for point-defect reactions in 3C-SiC, Phys. Rev. B - Condens. Matter Mater. Phys. 88 (2013) 1–15. doi:10.1103/PhysRevB.88.054105.
[112] A. Debelle, L. Thomé, I. Monnet, F. Garrido, O.H. Pakarinen, W.J. Weber, Ionization-induced thermally activated defect-annealing process in SiC, Phys. Rev. Mater. 3 (2019) 1–11. doi:10.1103/physrevmaterials.3.063609.
[113] W. Jiang, W.J. Weber, V. Shutthanandan, L. Li, S. Thevuthasan, Thermal and dynamic responses of Ag implants in silicon carbide, Nucl. Instruments Methods Phys. Res. Sect. B Beam Interact. with Mater. Atoms. 219–220 (2004) 642–646. doi:10.1016/j.nimb.2004.01.134.
[114] M.A. Capano, J.A. Cooper, M.R. Melloch, A. Saxler, W.C. Mitchel, Ionization energies and electron mobilities in phosphorus- and nitrogen-implanted 4H-silicon carbide, Mater. Sci. Forum. 338 (2000). doi:10.4028/www.scientific.net/msf.338-342.703.
[115] Y. Negoro, K. Katsumoto, T. Kimoto, H. Matsunami, Electronic

behaviors of high-dose phosphorus-ion implanted 4H-SiC (0001), J. Appl. Phys. 96 (2004) 224–228. doi:10.1063/1.1756213.

[116] D. Dwight, M. V. Rao, O.W. Holland, G. Kelner, P.H. Chi, J. Kretchmer, M. Ghezzo, Nitrogen and aluminum implantation in high resistivity silicon carbide, J. Appl. Phys. 82 (1997) 5327–5333. doi:10.1063/1.366299.

[117] E.G. Seebauer, K.W. Noh, Trends in semiconductor defect engineering at the nanoscale, Mater. Sci. Eng. R Reports. 70 (2010) 151–168. doi:10.1016/j.mser.2010.06.007.

[118] H.J. Queisser, E.E. Haller, Defects in semiconductors: Some fatal, some vital, Science (80-.). 281 (1998) 945–950. doi:10.1126/science.281.5379.945.

[119] S. Mahajan, Defects in semiconductors and their effects on devices, Acta Mater. 48 (2000) 137–149. doi:10.1016/S1359-6454(99)00292-X.

VITA

Lauren Nuckols is from Hillsboro, Missouri. She received her high school diploma from Hillsboro High School in 2012. Lauren then attended Missouri University of Science and Technology in Rolla, MO where she earned her B.S in Ceramics Engineering in 2016. She joined the Materials Science and Engineering department at the University of Tennessee, Knoxville in August 2017 for her Ph.D. Lauren's research was performed under the supervision of Prof. William J. Weber and focused on understanding ion irradiation effects in semiconductors.